Mechanistic study on redox reactions over heterogeneous catalysts and design of local structure of active sites

Okemoto, Atsushi

(Degree)
博士（工学）

(Date of Degree)
2017-03-25

(Date of Publication)
2018-03-01

(Resource Type)
doctoral thesis

(Report Number)
甲第6930号

(URL)
https://hdl.handle.net/20.500.14094/D1006930

Doctoral Dissertation

博 士 論 文

Mechanistic study on redox reactions over heterogeneous catalysts and design of local structure of active sites

不均一触媒による酸化還元反応の機構解明と活性点構造の設計

Graduate School of Engineering, Kobe University

神戸大学大学院工学研究科

Atsushi Okemoto

桶本篤史

January, 2017

平成 29 年 1 月

PREFACE

In this thesis, catalyst design for benzene hydroxylation and photocatalytic reactions was described, and each reaction mechanism was also investigated experimentally and theoretically. For catalyst design in the benzene hydroxylation, encapsulation of vanadium complex catalyst successfully provided the heterogeneous catalyst in the liquid-phase reaction. Furthermore, it was found out that binuclear structure of metal complex catalyst has a possibility of a better catalyst than mononuclear catalyst. For the photocatalytic reaction, visible-light responsible catalyst was successfully prepared by doping with transition metal ions. Investigation of mechanism of these reactions revealed the structure of reaction intermediates and energy diagram of the reactions. This work should be helpful for not only understanding the detailed mechanisms, but also providing valuable clue for rational design and the effective preparation of catalysts. Each abstract of these chapters is summarised as follows:

1. Liquid Phase Oxidation of Benzene with Molecular Oxygen Catalysed by Vanadium Complex

Vanadium complex catalysts encapsulated in Y-zeolite (VPA-Y), which are prepared by the “Ship in a Bottle” method, are investigated as heterogeneous catalysts for the liquid-phase oxidation of benzene to phenol with molecular oxygen. Phenol is the major product of the process, and the

catalyst can be easily separated from the product solution after the reaction. These encapsulated catalysts are characterized by thermogravimetric analysis, demonstrating that the vanadium complexes are formed in the Y-zeolite cages.

2. Benzene Hydroxylation in Liquid Phase Using Binuclear Copper Complex Catalyst

Mono- or binuclear copper homogeneous catalysts with similar coordination environment were used for the benzene hydroxylation. The effect of multiple active sites on phenol formation was investigated. The structures of the synthesized mono- and binuclear copper catalysts were confirmed by FT-IR and EXAFS. Molecular oxygen was used as the oxidant and it was found that the binuclear copper catalyst showed better phenols formation than the mononuclear catalyst.

3. Reaction Mechanism of Liquid-Phase Oxidation of Benzene

Vanadium complex catalysts were successfully encapsulated within the supercage of Y-zeolite by Ship in a bottle method. The synthesised materials exhibited to be active catalysts for the hydroxylation of benzene to phenol with molecular oxygen and reusable along at least two catalytic cycles. Effect of ligands on the catalytic performance was also investigated experimentally and theoretically using DFT calculations at B3LYP/6-31G* computational levels. These results revealed the catalytic property depends on the formation rate of hydrogen peroxide as a reaction intermediate

through redox cycle between V(III)/V(IV). Furthermore, the activation mechanism of molecular oxygen catalysed by the vanadium complex in this reaction was investigated theoretically using the B3LYP/6-31G* calculations. The different reaction pathways were mapped out, and the computational results revealed that the reaction subsequences including five steps to form hydrogen peroxide with the energy barrier of 106 kJ/mol at the most.

4. Gas-Phase Benzene Hydroxylation with Molecular Oxygen Catalysed by Cu/HZSM-5

The direct hydroxylation of benzene to phenol over a Cu impregnated zeolite catalyst (Cu/HZSM-5) is performed in airflow. Phenol is obtained as a main product in a yield of 2.5%; however, the selectivity of phenol is low (44.0%) due to the formation of by-products such as hydroquinone, *p*-benzoquinone, CO, and CO_2. The use of Cu/HZSM-5 leads to a significantly higher selectivity of phenol (94.0%) under an O_2 partial pressure that is lower than the atmospheric O_2 partial pressure. It is found that excess O_2 in the gas-phase causes the formation of by-products, whereas a decrease of O_2 partial pressure prevents the by-products from forming. Moreover, the addition of Ti to Cu/HZSM-5 leads to improved phenol formation activity. High yield (4.3%) and selectivity (88.0%) of phenol are achieved over Cu/Ti/HZSM-5 under a low O_2 partial pressure. The addition of Ti is found to accelerate the formation of Cu^+ as an active site. It is therefore speculated that phenol can be formed selectively over Cu/Ti/HZSM-5 under lower O_2 partial pressure owing to the increase of Cu^+

sites by Ti addition and the prevention of by-product formation by the decreased O_2 partial pressure.

5. Visible-Light-Responsible Tungsten Oxide for Photo-oxidation of Cyclohexane

The cyclohexane photo-oxidation is performed under visible light irradiation over WO_3 photocatalysts with molecular oxygen. Cyclohexanone and cyclohexanol are obtained with high selectivity. On the basis of isotope labeled experiments and ESR measurement, cyclohexyl radical is formed as a reaction intermediate. The lattice oxygen of WO_3 is involved in products formation, thus it is indicated that products are produced by the reaction of cyclohexyl radical with the lattice oxygen of WO_3. The physical mixing of TiO_2 with Pt/WO_3 leads to higher photocatalytic activity than that of Pt/WO_3. The photocatalytic activity increases with increasing BET surface area of TiO_2 which is mixed with Pt/WO_3. The physical mixing of TiO_2 is found to accelerate the formation of cyclohexyl radical. It is therefore speculated that the surface of TiO_2 contributes to the formation of cyclohexyl radical or stabilization of cyclohexyl radical.

6. Visible-Light-Responsible Titanium Oxide by Doping with Ferrous Ions for Photodecomposition of Ammonia

The photodecomposition of NH_3 to H_2 and N_2 was carried out by using Pt-supported metal-doped TiO_2 ($Pt/M\text{-}TiO_2$, M: dopant element)

photocatalyst in an aqueous NH_3 solution under UV irradiation at room temperature. Fe-doped TiO_2 photocatalysts ($Pt/FeTiO_2$) promoted the highest yield of H_2 formation in the NH_3 photodecomposition. UV-visible diffuse reflectance spectra of Fe-doped TiO_2 showed that the absorption edge of TiO_2 was shifted from the ultraviolet to the visible light region by substitution with Fe. In addition, X-ray diffraction and electron spin resonance spectra showed that the dopant metals substituted a portion of the Ti^{4+} sites in the TiO_2 crystal without changing TiO_2 structure. Hence, it is indicated that TiO_2 doped with Fe can utilize visible light wavelengths and effectively produce hydrogen from the decomposition of aqueous NH_3.

7. Reaction Mechanism of Ammonia Photodecomposition Catalysed by Titanium Oxide

The photodecomposition of NH_3 to H_2 and N_2 was carried out by using metal-supported TiO_2 (M/TiO_2) photocatalysts in an aqueous NH_3 solution under UV irradiation at room temperature. Ni/TiO_2 photocatalysts were prepared and promoted the highest yield of H_2 formation in the NH_3 photodecomposition. It was found that a NH_2 radical formed as a dominant intermediate through the NH_3 decomposition by ESR measurements. Reaction pathways via the NH_2 radical formation have been investigated in detail by density functional theory (DFT). It is concluded that H_2 and N_2 form via $H_2N\text{-}NH_2$ by the coupling of adjacent NH_2 radicals or one NH_2 radical and ammonia in gas phase from the NH_3 photodecomposition. Our

findings should be useful for further developments of efficient catalytic systems.

8. Visible-Light-Responsible Titanium Oxide by Co-Doping with Tantalum and Chromium Ions for Photocatalytic Decomposition of Water with Urea as a Reducing Agent

Urea is expected to be used for a sacrificial material in the photocatalytic formation of hydrogen from water decomposition because it is a non-petroleum material and abundant in domestic wastewater. In this study, a TiO_2 catalyst co-doped with tantalum(V) and a trivalent metal cation, serving as promoters, was applied for the photocatalytic decomposition of water for hydrogen production using urea as the sacrificial agent. Co-doping of TiO_2 with tantalum(V) and a trivalent metal cation resulted in a considerable redshift of the absorption edge of TiO_2 via the formation of impurity levels. In particular, the incorporation of tantalum(V) and chromium(III) into TiO_2 resulted in significant performance enhancement for the photocatalytic photodecomposition of water for hydrogen production. The products obtained from the photodecomposition of water with urea were also identified, and urea was transformed into N_2 and CO_2 during the reaction. Moreover, the reaction was performed using thin-film photocatalysts based on organic semiconductors, such as picene, representing a class of novel, unconventional photocatalytic materials. Picene thin-films exhibited activity similar to that exhibited by traditional inorganic semiconductors. Effective utilisation of urea has potential application in a green and

sustainable production of hydrogen from wastewater via photocatalysis using various semiconductors.

9. Application of Picene Thin-Film Organic Semiconductors for Photodecomposition of Water with Reducing Agents

Herein, interesting photocatalytic properties of a picene thin film on quartz (PTF/Q) have been demonstrated for photocatalytic hydrogen formation from water using several sacrificial agents. Hydrogen is produced in the presence of PTF/Q catalysts under light irradiation, indicating that PTF/Q works as a photocatalyst. The catalyst retains its activity under light irradiation and addition of sacrificial agents enhanced the rate of photocatalytic hydrogen formation from water, similar to the condition when a traditional inorganic photocatalyst is used. Moreover, PTF/Q catalysts comprising picene films of different thickness have been fabricated, and PTF/Q with the thinnest film (50 nm) exhibits the highest activity for hydrogen formation. X-ray diffraction patterns show that the picene crystals are vertically aligned on the surface of the quartz sheet, and that PTF/Q with the thinnest film has a nonuniform film phase. The difference of picene thin-film surface in morphology probably influences the photocatalytic activity. The absorption edge and optical gap energies of the prepared PTF/Q catalyst are determined and the optical gap of the picene film is calculated to be 3.2 eV.

TABLE OF CONTENTS

1. General Introduction

Chapter 1. General Introduction

Catalysis is responsible for nearly all chemical products manufactured in the chemical synthetic and biological fields. Heterogeneous catalytic reactions provide a majority of the commodity chemicals and fuels. To a large extent, inspiration of the design of catalyst is rooted in deep understanding of reaction mechanisms. Chemical reactions are the chemical phenomena along with bond formations and cleavages from changes of electronic states among reactants and catalysts. To explore high-performance catalysts, analytical investigation based on electronic states is necessary, and theoretical calculations are indispensable for determining the electronic states. The number of articles relating to theoretical calculation has recently increased in the fields of spectroscopy assignments, study of electronic states and structures, and elucidation of reaction mechanisms. This trend is due to improvements in CPU speeds and the development of advanced molecular theories. Among these, the use of density functional theory (DFT) has rapidly progressed after 1990, and DFT makes an important contribution to promotion of theoretical calculations. With DFT, the electronic state of the chemical compounds is expressed by electron density functional, which have been modified and proposed by many types of approaches for improving computation accuracy. This thesis takes two approach to catalyst design for thermal and photo catalytic reactions, by conducting high-throughput quantum-mechanical

computations for theoretical studies, as well as by performing laboratory-based synthesis, testing, and analysis for experimental studies. The study focus on investigation of detailed reaction mechanism in thermal and photo catalytic reactions. The investigation of the mechanisms of the catalytic reactions in this thesis provided first-insights into the action of the catalyst principles and these design for oxygen oxidation of benzene and photocatalytic reaction. These discoveries open the door to the design of new classes of catalytic materials, for energy efficient production of important chemicals and fuels.

1.1. Selective Oxidation of Hydrocarbons with Molecular Oxygen

Certain catalytic oxidation processes have long been a part of industrial chemistry. One of the most remarkable technical developments of recent times is the conversion of natural hydrocarbons of petroleum by catalytic process in the petroleum refining industry [1-5]. In variety of chemical reactions involved and in scale of application, it surpasses by far of any the other catalytic industrial operations which have been witnessed in past. Although there are many studies of catalytic oxidation, the field of catalytic oxidation is still one which should be attractive to researchers interested in catalysis. Previous papers have appeared, which describe successful attempts to apply the properties of transition metal complexes and the solid acid materials to oxidation catalysts [5-8]. There has been much

interest in understanding of catalytic phenomena so that it will bring the progress of technology in the field of catalytic oxidation. This thesis describes several catalytic oxidations of materials and the reaction mechanism in the direct oxidation of benzene to phenols with molecular oxygen in detail. It is one of the most difficult and challenging processes in the catalytic oxidations because catalytic activation of sp^2 C-H bond causes formation of the desired product with further oxidation that would give CO and CO_2. A catalyst for a partial-oxidation process should be designed to provide a limit amount of oxygen to a reactant. Yang et al. reported that benzene was oxidised with 2,2,6,6-Tetramethylpiperidinyloxy (TEMPO) in the presence of $Py_3PMo_{10}V_2O_{40}$ as a catalyst [9]. This was an example of liquid-phase direct oxidation of benzene by various oxidising reagents. Since then, many production processes of phenols by catalytic partial-oxidation of benzene have been studied in operation with mineral acid or organic acid peroxide as an oxidant [10-13]; however, they would be difficult to consider the economical and eco-friendly process because the oxidants are toxic and hazardous materials. Only recent have become available giving some insight into the reaction with molecular oxygen instead of the other oxidants [14-16]. Molecular oxygen can be easily obtained from atmosphere by fractional distillation based on the components' boiling point, and is the least expensive oxidising reagents. Partial oxidation with molecular oxygen is an economically and industrially useful process because of its productivity, general-purpose properties, and safety. Partial insertion reactions of oxygen to reactants are many and varied, and

usually involve the initiation and propagation of free-radical reactions by metal ions. The best known example of the partial insertion is Udenfriend's system, which uses a suitable two-electron reductant such as a catechol and a chelate compounds of iron(II) for the conversion of alkenes, alkanes, and aromatic compounds to epoxides, alcohols, and phenols [17,18]. Most other partial insertion reactions are metal ion-catalysed free-radical reactions in which hydrogen peroxide is the source of oxygen. The mechanism of the metal ion catalysed reactions with molecular oxygen are examined from the point of view of applying these mechanisms toward a better understanding of the corresponding oxygen oxidations in this thesis.

1.2. Catalyst Design for Benzene Hydroxylation

In chapter 2 of this thesis, catalyst design for benzene hydroxylation with molecular oxygen is studied. Previous study reported a homogeneous catalyst including vanadium or copper ions efficiently catalysed the benzene derivatives hydroxylation [19-21]. Although a homogeneous catalyst is known to enhance liquid-phase reactions with excellent yield and selectivity, homogeneous systems are often regarded with many limitations, including separation problem. Heterogenisation efforts have been made to utilise metal oxide catalysts on typical solid supports, which are chemical and thermal stable, such as silica, alumina, and the others. However, the catalytic properties of metal oxide in the benzene hydroxylation were far

inferior to that of the corresponding homogeneous complex catalysts, probably because of low frequency of immediate contact reactions to active sites in the solid-liquid interface. Homogenization of the catalyst with high activity in the reaction is necessary to incorporate homogeneous metal complexes on solid supports. In specific, encapsulation of metal complexes in the nanopores of Y-zeolite is an eco-friendly technique for heterogenisation; since no leaching is perceived when the complex is confined entirely in the nanocavity of Y-zeolite [22,23]. A vanadium complex catalyst encapsulated in Y-zeolite, which are prepared by the "Ship in a Bottle" method, are studied as heterogeneous catalysts for the liquid-phase oxidation of benzene to phenol with molecular oxygen. The vanadium complex, which catalyses the selective formation of phenol as the major product, are encapsulated in the cage of Y-zeolite and can be used as a heterogeneous catalyst in liquid-phase reactions. These encapsulated catalysts are characterized by thermogravimetric analysis, demonstrating that the vanadium complexes are formed in the Y-zeolite cages. In chapter 2.1, the method for preparation of the heterogeneous vanadium complex catalyst and its reaction stability in liquid-phase oxidation of benzene are discussed.

Chapter 2.2 deals with catalyst design of a copper complex catalyst for highly efficient synthesis of phenols. Copper is widespread in nature, being present in the active sites of many oxidation enzymes, often as di-, tri-, or polynuclear for oxidation reactions. Multi-copper catalysts have been used for alkane oxidation; however, there are only few reports on their application

limited to homogeneous catalysis with respect to oxidative coupling [24-26]. In this chapter, binuclear copper homogeneous catalyst is prepared for the benzene hydroxylation. The effect of multiple active sites, such as binuclear complex, on phenol formation is investigated in this chapter. The structures of the synthesized mono- and binuclear copper catalysts are confirmed by FT-IR and EXAFS.

In the previous chapters, heterogenisation technique and the effect of multi-nuclear structure of metal complex are discussed for design of highly effective catalyst on hydroxylation of benzene. In chapter 2.3, reaction mechanism of benzene hydroxylation is studied for a better understanding of the oxygen oxidation. Molecular oxygen is kinetically quite stable towards reaction at room temperature because of its triplet ground state and strong oxygen-oxygen bond. On the other hand, the thermodynamic tendency for the reaction of O_2 is combustion, that is to form carbon dioxide and water. Thus, hydrocarbons typically react with O_2 via a complicated free-radical pathway termed auto-oxidation. These reactions are usually not selective and often have little synthetic utility [27]. Vanadium or copper complex, which is effective for the selective synthesis of phenols form benzene oxidation with molecular oxygen, is supposed to catalyse the reaction by other pathways. Investigation of the special pathway is very important for deep understanding a pathway of selective activation of oxygen, and contributes to overcome the limitation that oxygen oxidations are not selective. In chapter 3, liquid-phase oxidation of benzene catalysed by the vanadium complex and the reaction mechanism are studied.

1.3. Gas-Phase Benzene Hydroxylation

Oxidations in the liquid-phase with molecular oxygen as a oxidising source are covered in chapter 2. Chapter 3 describes gas-phase hydroxylation of benzene to phenol. Gas-phase hydroxylation also requires selective activation process of oxygen similar to the liquid-phase. Moreover, the gas-phase process has serious problem that the products easily oxidizable to CO and CO_2 in the high temperature process. This chapter deals with effort to improve selectivity of the product over a Cu impregnated zeolite catalyst (Cu/HZSM-5). In previous study, phenol was obtained as a main product in a yield of 2.5%; however, the selectivity of phenol was low (44.0%) due to the formation of by-products such as hydroquinone, *p*-benzoquinone, CO, and CO_2 [28]. Then, low selectivity of phenol is need to be improved. It is found that excess O_2 in the gas-phase causes the formation of by-products, whereas a decrease of O_2 partial pressure prevents the by-products from forming. Moreover, the addition of Ti to Cu/HZSM-5 leads to improved phenol formation activity. In this chapter, gas-phase selective oxidation of benzene over Cu/Ti/HZSM-5 and the effect of molecular oxygen feed on the catalytic activity are studied.

1.4. Reaction Mechanism and Catalyst Design of Organic and Inorganic Semiconductors for Photocatalysis

This chapters describe reaction mechanism and catalyst design for photocatalytic processes. Photocatalysis, such as photodegradation and photodecomposition, are known for mild condition reactions by oxidising power of semiconductors, such as titanium oxide. Then, photo-oxidation as an economical and industrial process has received considerable attention in recent years, such as selective photo-oxidation of chemical substrates, photodegradation of chemical waste and photodecomposition of hydrogen carriers [29-32]. Chapter 5.1 describes the selective photo-oxidation of cyclohexane and catalyst design for a visible-light-responsible catalyst. The cyclohexane photo-oxidation is performed by tungsten oxide photocatalyst with molecular oxygen. Tungsten oxide is visible-light responsible and chemical stable material in water or organic solution. It is, therefore, expected to be a photocatalyst for photo-oxidation under mild conditions. And also, the reaction mechanism is investigated on the basis of isotope labeled experiments and ESR measurement.

The photodegradation has already put into practice, applying of the reaction using titanium oxide extends to water treatment and air cleaning systems. The latter reaction is expected to be an eco-friendly process in which hydrogen is produced as energy source without a fossil resource including a petroleum resource, though it hasn't been used for industrial field yet. Of special interest are liquid hydrogen carriers (LHCs), such as water

[33,34], ammonia [35], formic acid [36], which can be readily loaded and unloaded with considerable amounts of hydrogen. Among them, water and ammonia have advantages as a hydrogen storage carrier as follows: First, CO_2 is not exhausted in decomposition since it does not contain carbon. Second, ammonia can be easily transported and stored, as severe conditions are not necessary for its liquefaction. Finally, hydrogen content percentage in one molecule (H_2O: 11.1%, NH_3: 17.6%) is high in comparison with that in other hydrogen storage carriers such as liquefied petroleum gas (LPG). Chapter 4.2 describes the photodecomposition of NH_3 to H_2 and N_2 was carried out by using Pt-supported metal-doped titanium oxide (Pt/M-TiO_2, M: dopant element) photocatalyst in an aqueous NH_3 solution under UV irradiation at room temperature. In particular, Fe-doped TiO_2 photocatalysts (Pt/FeTiO_2) promotes the formation of H_2 and N_2 in the NH_3 photodecomposition. By UV-visible diffuse reflectance, X-ray diffraction and electron spin resonance measurements, the effect of the dopant metals substituted a portion of the Ti^{4+} sites on the titanium oxide crystal structure and the photocatalytic activity is discussed. Furthermore, chapter 4.3 deals with investigation of reaction mechanism for ammonia photodecomposition by titanium oxide. Although it is known that ammonia can be decomposed to hydrogen and nitrogen by titanium oxide, the reaction pathways on titanium oxide is still unknown. I focus on the mechanism of breaking away of hydrogen molecular from the surface of titanium oxide. The reaction profile and its energy diagram is obtained on basis of DFT calculations.

Chapter 4.4. describes photodecomposition of water with urea. Urea

is expected to be used for a sacrificial material in the photocatalytic formation of hydrogen from water decomposition because it is a non-petroleum material and abundant in domestic wastewater [37]. In this study, a TiO_2 catalyst co-doped with tantalum(V) and a trivalent metal cation, serving as promoters, was applied for the photocatalytic decomposition of water for hydrogen production using urea as the sacrificial agent. Co-doping of TiO_2 with tantalum(V) and a trivalent metal cation resulted in a considerable redshift of the absorption edge of TiO_2 via the formation of impurity levels. In particular, the incorporation of tantalum(V) and chromium(III) into TiO_2 resulted in significant performance enhancement for the photocatalytic photodecomposition of water for hydrogen production. The products obtained from the photodecomposition of water with urea are also identified. Moreover, the reaction is performed using thin-film photocatalysts based on organic semiconductors treated in chapter 5.2, representing a class of novel, unconventional photocatalytic materials.

In chapter 4.5, interesting photocatalytic properties of a picene thin film on quartz (PTF/Q) is demonstrated for photocatalytic hydrogen formation from water using several sacrificial agents. A low-molecular-weight organic semiconductor, such as picene, exhibits light absorption similar to the band gap of a typical inorganic photocatalyst [38,39]. Since the optical property is almost similar to that of typical TiO_2 photocatalysts, picene is supposed to enhance photodecomposition of water. This study is the first example of single picene photocatalyst for water photodecomposition, and effect of picene thin-film structure on catalytic

performance is discussed in detail.

Throughout this whole thesis, various oxidations of thermal and photo reactions are discussed, and there are a lot of studies and commentaries on a better understanding of their reaction mechanism. Finally, general conclusion of these studies are presented at the end of this thesis.

References

1. Y. Ishii, S. Sakaguchi, T. Iwahama, *Adv. Synth. Catal.*, 343 5 (2001) 393–427.
2. C. N. Satterfield, *Heterogeneous Catalysis in Indus-trial Practice*, McGraw-Hill, New York (1991).
3. P. Gélin, M. Primet, *Appl. Catal. B: Environ.*, 39 1 (2002) 1–37.
4. R Venkatadri, R.V Peters, *Hazard. Waste Hazard. Mater.*, 10 (1993) 107–147.
5. F.K. Nesheiwat, A.G Swanson, *Chem. Eng. Prog.*, 96 4 (2000) 47–52.
6. P.R Gogate, S Mujumdar, A.B Pandit, *Ind. Eng. Chem. Res.*, 41 14 (2002) 3370–3378.
7. A. E. Shilov, G. B. Shul'pin, *Chem. Rev.*, 97 (1997) 2912–2914.
8. G. I. Panov, A. K. Uriarte, M. A. Rodkin, V. I. Sobolev, *Catal. Today*, 41 4 (1998) 365–385.
9. H. Yang, J. Q. Chen, J. Li, Y. Lv, S. Gao, *Appl. Catal. A: Gen.*, 415–416 (2012) 22–28.
10. C. Wang, L. Hu, Yi. Hu, Y. Ren, X. Chen, B. Yue, H. He, *Catal. Commun.*, 68 (2015) 1–5.
11. R. Molinari, C. Lavorato, T. Poerio, *Appl. Catal. A: Gen.*, 417–418 (2012) 87–92.
12. T. Miyahara, H. Kanzaki, R. Hamada, S. Kuroiwa, S. Nishiyama, S. Tsuruya, *J. Mol. Catal. A: Chem.*, 176 (2001) 141–150.
13. Y. Masumoto, R. Hamada, K. Yokota, S. Nishiyama, S. Tsuruya, *J. Mol.*

Catal. A: Chem., 184 (2002) 215–222.

14. C. Guo, W. Du, G. Chen, L. Shi, Q. Sun, *Catal. Commun.*, 37 5 (2013) 19–22.
15. L. Bortolotto, R. Dittmeyer, *Sep. Purif. Technol.*, 73 1 (2010) 51–58.
16. S. P. de Visser, *Adv. Inorg. Chem.*, 64 (2012) 1–31.
17. M. M. Taqui Khan, R. S. Shukla, A. Prakash Rao, *Inorg. Chem.*, 28 3 (1989) 452–458.
18. Derek H.R. Barton, Nathalie C. Delanghe, *Tetrahedron*, 54 18 (1998) 4471–4476.
19. B. Gao, Y. Li, N. Shi, *React. Funct. Polym.*, 73 11 (2013) 1573–1579.
20. K. C. Gupta, A. K. Sutar, C.-C. Lin, *Coord. Chem. Rev.*, 253 13–14 (2009) 1926–1946.
21. D. Bianchi, M. Bertoli, R. Tassinari, M. Ricci, R. Vignola, *J. Mol. Catal. A: Chem.*, 200 1–2 (2003) 111–116.
22. S. M Drechsel, R. C.K Kaminski, S. Nakagaki, F. Wypych, *J. Colloid Interface Sci.*, 277 1 (2004) 138–145.
23. G. Li, Lijuan C., J. Bao, T. Li, F. Mei, *Appl. Catal. A: Gen.*, 346 1–2 (2008) 134–139.
24. Y. Lan, B. Liao, Y. Liu, S. Peng, Sh. Liu, *Eur. J. Org. Chem.*, (2013) 5160–5164.
25. J. Gao, S. Zhong, *J. Mol. Catal. A: Chem.*, 164 1–2 (2000) 1–7.
26. Y. Wang, J. Xiao, X. Hua, X. Yi, *Inorg. Chim. Acta*, 435 (2015) 125–130.
27. G. Henricio, S. Olive, *Angewandte Chemie. Inter. Edit. Eng.*, 13 1 (1974) 29–38.

28. Y. Shibata, R. Hamada, T. Ueda, Y. Ichihashi, S. Nishiyama, Shigeru Tsuruya, *Ind. Eng. Chem. Res.*, 44 (2005) 8765–8772.
29. S. M. Rodríguez, J. B. Gálvez, C. A. Estrada Gasca, *Solar Energy*, 77 5 (2004) 443–444.
30. F. A. Momani, *J. Photochem. Photobiol. A: Chem.*, 179 1–2 (2006) 184–192.
31. H. Lachheb, E. Puzenat, A. Houas, M. Ksibi, E. Elaloui, C. Guillard, J. Herrmann, *Appl. Catal. B: Environ.*, 39 1 (2002) 75–90.
32. M. Pera-Titus, V. García-Molina, M. A Baños, J. Giménez, S. Esplugas, *Appl. Catal. B: Environ.*, 47 4 (2004) 219–256.
33. Z. Zou, Ji. Ye, K. Sayama1, H. Arakawa, *Nature*, 414 (2001) 625–627.
34. A. Kudo, Y. Miseki, *Chem. Soc. Rev.*, 38 (2009) 253–278
35. A. Klerke, C. H. Christensen, J. K. Nørskov, T. Vegge, *J. Mater. Chem.*, 18 (2008) 2304–2310.
36. K. Tsutsumi, N. Kashimura, K. Tabata, *Silicon*, 7 1 (2015) 43–48.
37. M.R. Rahimpour, A. Azarpour, *Eng. Life Sci.*, 3 8 (2003) 335–340.
38. Y. Kubozono, X. He, S. Hamao, K. Teranishi, H. Goto, R. Eguchi, T. Kambe, S. Gohda, Y. Nishihara, *Eur. J. Inorg. Chem.*, (2014) 3806–3819.
39. T. Abe, Y. Tanno, N. Taira, K. Nagai, *RSC Adv.*, 5 (2015) 46325.

2. Mechanistic Study of Benzene Hydroxylation with Molecular Oxygen over Transition Metal Catalysts and Catalyst Design

Chapter 2.1. Liquid Phase Oxidation of Benzene with Molecular Oxygen Catalysed by Vanadium Complex

2.1.1. Introduction

Phenol, one of the most important chemical intermediates in industry, is mainly manufactured using the cumene method. However, this process consists of three steps and produces acetone as a byproduct. The one-step production of phenol by direct insertion of oxygen into the C-H bond is a desirable method, because the aromatic C-H bond is so energetically stable, it is one of the most challenging to perform. Consequently, it has been widely investigated [1-5]. Our laboratory recently reported the phenol synthesis for the liquid-phase oxidation of benzene over supported vanadium catalysts with molecular oxygen by using reducing agents [6-8]. Although vanadium species in these catalysts leached into the reaction solution during the reaction. An oxovanadium acetylacetonate which functioned as a homogeneous catalyst also catalyzed the oxidation of benzene more effective than the supported catalysts catalyst. However, it is generally difficult to recover a homogeneous catalyst from a reaction solution because of its full or partial dissolution in the reaction solution. Therefore, the utilization of a heterogeneous catalyst without the leaching of vanadium species in this reaction is desirable because of its ease of separation. In this study, I have

attempted to avoid this problem by preparing a vanadium complex catalyst encapsulated in a supercage of Y-zeolite (VPA-Y).

2.1.2. Experimental

Vanadium complexes encapsulated in Y zeolite catalysts was prepared by the “ship in a bottle” method (see Figure 1). Proton type Y zeolite and oxovanadium sulfate were added to deionized water, and the mixture was stirred at 353 K for 48 h. The mixture was then filtered, washed, and dried at 393 K overnight. The Y-zeolite on which the oxovanadium ion was anchored was named V-Y. The V-Y and picolinic acid (PA) were dispersed in methanol and the mixture refluxed with stirring at 333 K for 20 h, then filtered, washed with methanol, and dried at 393 K overnight. The obtained solid was stirred in methanol once again to remove any unreacted oxovanadium ions and picolinic acid on the surface of the Y-zeolite.

Picolinic acid supported Y-zeolite was prepared by stirring H-Y zeolite and picolinic acid in methanol, evaporating to dryness at 333 K in a hot water bath, and then drying at 393 K overnight. The obtained solid is termed PA/H-Y. Benzene (5.6 mmol, 0.5 ml) was added to an acetic acid aqueous solution (20 vol%, 5 ml) with 0.1 g of catalyst and a reducing agent. The reaction was carried out at 353 K under 0.4 MPa of O2 (gauge pressure). The oxidation products were analyzed by high-performance liquid chromatography (Jasco MD-2010 Plus) equipped with a GH-C18 column.

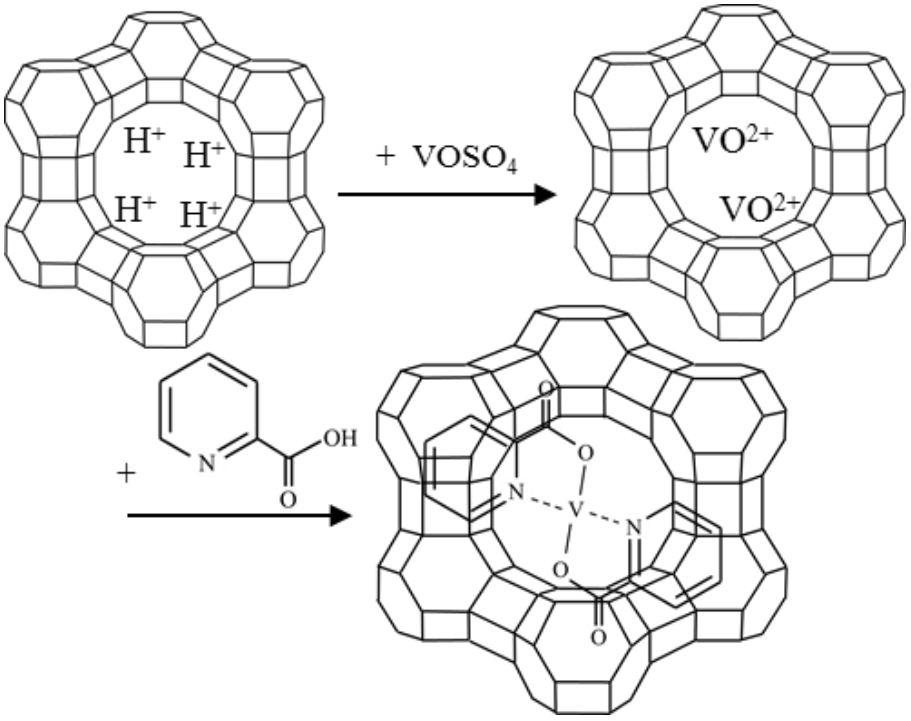

Figure 1. The preparation process of vanadium complex catalyst encapsulated in supercage of Y-zeolite by the ship in a bottle method.

Recycling of the catalyst was attempted through separation by centrifugation, washing with acetone three times, and drying at 393 K overnight.

The vanadium content of the catalysts was measured by XRF (Rigaku Primini) equipped with Pd as X-ray source. Thermogravimetric and differential thermal analysis (TG-DTA) was carried out with DTG-60 (SHIMAZU). For the TG-DTA measurements, the samples were heated to 1173 K at 10 K/min in a constant air flow.

2.1.3. Results and Discussion

The liquid-phase oxidation of benzene to phenol is carried out by using an oxovanadium acetylacetonate catalyst with molecular oxygen as the oxidant and ascorbic acid as the reducing agent. Phenol is the major product, and hydroquinone and benzoquinone are hardly observed in this reaction. I tried to determine the most effective reducing agent for the reaction by using an oxovanadium acetylacetonate as a homogeneous catalyst. The results of phenol yield by using several reducing agents are shown in Table 1. The mentioned phenol yields are the maximum which are obtained by using the optimum amount of reducing agent. The efficiency of the reducing agent is calculated as the rate of phenol formation per equivalent of reducing agent. The addition of L-ascorbic acid (1.0 mmol) as a reducing agent leads to the highest yield of phenol (6.7 mmol/g-cat). On the other hand, sucrose (0.4 mmol) as a reducing agent gives a

Table 1. Phenol yield over $VO(acac)_2$ with molecular oxygen by using several reducing agents.

Reducing agents	Amount of reducing agent [mmol]	Yields of phenol [mmol/g-cat.]	Reducing agents efficiency[a] [-]
L-ascorbic acid	1.0	6.2	0.62
Zinc powder	2.0	2.4	0.12
Sucrose	0.4	3.8	0.94
Glucose	0.4	1.3	0.32
Fructose	0.4	2.5	0.62

[a]: The efficiency of the reducing agent is calculated as the rate of phenol formation per equivalent of reducing agent.

phenol yield (3.8 mmol/g-cat) lower than that obtained with L-ascorbic acid. However, sucrose, as a reducing agent, exhibits the highest efficiency, indicating that sucrose is the preferred reducing agent for this reaction. This seemingly counterintuitive effect is explained by the fact that sucrose is a nonreducing disaccharide, being composed of fructose and glucose monomers. It does not function itself as reducing agent without hydrolysis. However, sucrose is hydrolyzed to glucose and fructose under mild acidic conditions, and each monomer works as a reducing agent [9-11]. Therefore, the phenol yield of sucrose (3.8 mmol/g-cat) is equal to the combined yields of glucose (1.3 mmol/g-cat) and fructose (2.5 mmol/g-cat).

Oxovanadium acetylacetonate shows a high phenol formation activity. However, it is hard to separate from the reaction solution after the reaction. Therefore, the vanadium complexes catalyst encapsulated in Y-zeolite (VPA-Y) is prepared as a heterogeneous catalyst. The Y type zeolite has large cavities, termed a supercage, with a diameter of around 1.4 nm. These supercages are connected to each other by tunnels or windows with a diameter of 0.74 nm [12-13]. The size of an oxovanadium acetylacetonate complex is smaller than the window of Y-zeolite. Hence, this complex may leach from the supercage of Y-zeolite to reaction solution. On the other hand, the size of the vanadium complex VPA is larger than the windows of Y-zeolite, therefore the encapsulation of the vanadium complexes prevents their leaching into the reaction solution. Hence, I use the VPA complex instead of an oxovanadium acetylacetonate. Table 2 shows the catalytic activities of VPA-Y and V-Y, and the vanadium content measured by XRF.

Table 2. Phenol formation activities and vanadium content of the vanadium ion exchanged in Y-zeolite catalyst (V-Y) and the vanadium complexes encapsulated in Y-zeolite catalyst (VPA-Y)

Catalysts	V content [mmol/g-cat.]	Yields of phenol [mmol/g-cat.]	
		Run 1	Run 2
V-Y	1.7	4.2	2.2
VPA-Y	0.48	4.9	4.4

Phenol is formed as the major product with both catalysts. The activity of the fresh V-Y and VPA-Y is much the same (4.2 % and 4.7 %, respectively). The phenol formation activity of the used V-Y catalyst (Run 2 in Table 2) shows a marked decrease in comparison with that of the fresh V-Y catalyst. On the other hand, the used VPA-Y catalyst shows a higher phenol formation activity than that of the used V-Y catalyst although the phenol formation activity of the used VPA-Y catalyst is slightly lower than that of the fresh VPA-Y catalyst. These results indicate that the encapsulation of vanadium complexes in the Y-zeolite supercage has prevented the vanadium complexes from leaching into the reaction solution, and that the VPA-Y catalyst can be effectively used as a heterogeneous catalyst.

The formation of VPA-Y was confirmed by TG-DTA. Figure 2 shows the thermogravimetric spectra (see Figure 2 (I)) and the DTA profiles (see Figure 2 (II)) of VPA-Y, V-Y, and PA/H-Y. The first weight loss steps of 5~10 % are observed at 373 – 423 K in all TG curves (A-C), and the endothermic peaks occur in DTA curves (a-c), which are attributed to the desorption of the coordinated water molecules on the catalysts [12]. The second weight loss of ca. 10 % appears at around 760 K in the TG profiles of VPA-Y (A). On the other hand, no weight loss was observed at the same temperature in the TG profiles of V-Y (B). The exothermal peak also appears at 760 K in DTA curve of VPA-Y (a). This suggests that the weight loss in VPA-Y is due to the combustion of the ligands in the vanadium complexes. Hence, the VPA-Y catalyst seems to be coordinated by the ligands. The weight loss in TG analysis of PA/H-Y (c) is not observed at

Figure 2. The thermogravimetric analysis (A-C) and differential thermal analysis (a-c) of VPA-Y (A, a), V-Y (B, b) and PA/H-Y (C,c) catalysts.

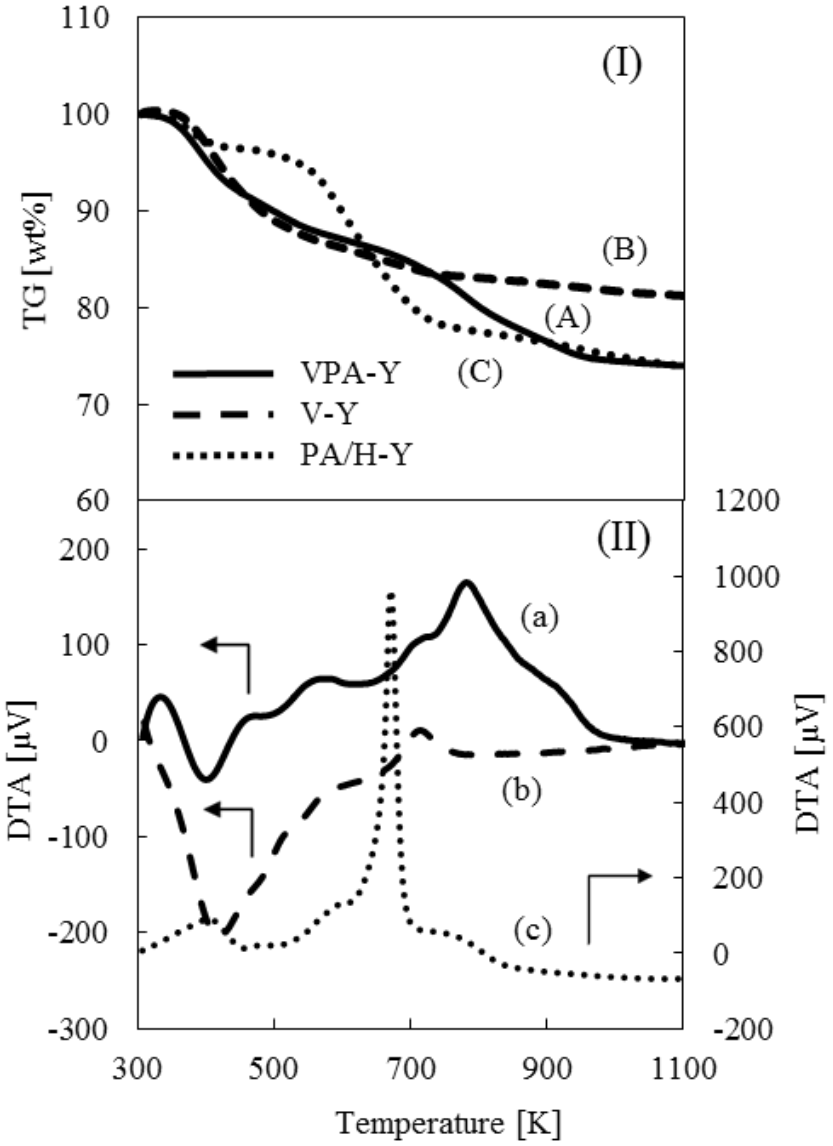

around 760 K, but at around 670 K. The exothermic peak appears at the same temperature in the DTA profile of PA/H-Y (c). This is attributed to the combustion of picolinic acid dispersed on the H-Y supports. The exothermic peak of the ligands in VPA-Y appears 50 K higher than that of PA/H-Y. It is suggested that the peak due to the combustion of ligands shifts from 670 K to 760 K because of the metal-ligand interaction in the VPA-Y samples. The amount of ligands in VPA-Y can be calculated by measuring the weight loss at around 760 K. The amount of ligands was 0.81 mmol/g-cat., and vanadium content was 0.48 mmol/g-cat in VPA-Y. The amount of ligands was 1.7 times of the vanadium ions, considering that two ligands coordinate to a vanadium ion. These results are also maintained by XAFS, FT-IR and UV-vis analysis [12-16]. Therefore, it is apparent that two ligands coordinate to a vanadium ion and that the vanadium complexes form inside the supercages of Y-zeolite.

2.1.4. Conclusion

The oxidation of benzene with molecular oxygen was carried out over VPA-Y by using sucrose as a reducing agent. It was shown that sucrose is the most effective reducing agent for this process. The catalytic stability of vanadium complexes encapsulated in Y-zeolite catalysts was confirmed by a recycling test in which the catalyst was successfully reused. The results of TG-DTA analysis show the formation of vanadium complexes in Y-zeolite.

The encapsulation of the vanadium complex catalysts in Y-zeolite prevented the leaching of vanadium species into the reaction solution, and thus is a powerful and convenient tool for the one-step oxidation of benzene to phenol.

References

1. T. Miyake, M. Hamada, Y. Sasaki, M, Oguri, *App. Catal. A*, 131 (1995) 33–42.
2. K. Nomiya, H. Yanagibayashi, C. Nozaki, K. Kondoh, E. Hiramatsu, Y. Shimizu, *J. M. Catal. A: Chem.*, 114 *(*1996) 181–190.
3. D. D. Devos, B. F. Sels, P. A. Jacobs, *Adv. Catal.*, 46 (2001) 1–87.
4. Y. Zhu, Y. Dong, L. Zhao, F. Yuan, *J. Mol. Catal. A: Chem.*, 315 (2010) 205–212.
5. J. Pan, C. Wang, S. Guo, J. Li, Z, Yang, *Catal. Commun.*, 9 (2008) 176–181.
6. K. Nomiya, S. Matsuoka, T. Hasegawa and Y. Nemoto, *J. Mol. Catal. A: Chem.*, 156 (2000) 143–152.
7. T. Miyahara, H. Kanzaki, R. Hamada, S. Kuroiwa, S. Nishiyama, S. Tsuruya, *J. Mol. Catal. A: Chem.*, 176 (2001) 141–150.
8. S. Sumimoto, C. Tanaka, S. Yamaguchi, Y. Ichihashi, S. Nishiyama, S. Turuya, *Ind. Eng. Chem. Res.*, 45 (2006) 7444–7450.
9. Y. Ichihashi, T. Taniguchi, H. Amano, T. Atsumi, S. Nishiyama, S. Tsuruya, *Top Catal*., 47 (2008) 98–100.

10. P.D. Bragg, L. Hough, *J. Chem. Soc.*, (1957) 4347–4352.
11. R. Larsson, B. Foikesson, *J. Mol. Catal.*, 229 (2005)183–190.
12. S. Yamaguchi, T. Fukura, C. Fujita, H.Yahiro, *Chem. Lett*., 41 (2012) 713–715.
13. A. kozlov, A. Kozlova, K. Asakura, Y. Iwasawa, *J. Mol. Catal. A: Chem.*, 137 (1999) 223-237
14. B. Sulikowski, J. Haber, A. Kubacka, K. Pamin, Z. Olejniczak. J. Ptaszynski, *Catal. Lett.*, 39 (1996) 27–31.
15. M. Alvaro, E. Carbonell, M. Espla, H. Garcia, *Appl. Catal. B: Environ.*, 57 (2005) 37–42.
16. C. Jin, W. Fan, Y. Jia, B. Fan, J. Ma, R. Li, *J. M. Catal. A: Chem.*, 249 (2006) 23–30.

Chapter 2.2. Benzene Hydroxylation in Liquid Phase Using Binuclear Copper Complex Catalyst

2.2.1. Introduction

Phenols are important chemical intermediates in industry and have been manufactured via multi-step oxidation of aromatic compounds. For example, almost 95% of global phenol production is based on the cumene process. However, this process has some disadvantages: high and damaging ecological impact, an explosive intermediate to manage (cumene hydroperoxide), and large amounts of acetone as a by-product. Therefore, an economical and eco-friendly one-step process for production of phenols is attractive and challenging, and has been widely investigated using oxidation of aromatics [1-7]. In a previous study, it has been reported that copper complexes catalysed the oxidation of benzene to phenol by using acetic acid solution as solvent and ascorbic acid as the reducing agent [8]. Copper is cheap and widespread in nature, being present in the active sites of many oxidation enzymes, often as di-, tri-, or polynuclear Cu centres that can selectively catalyse some oxidation reactions [9]. Some reports have shown the use of multi-copper compounds in alkane oxidation [10,11]; however, there are few reports on their application in homogeneous catalysis with respect to alkanes. In this paper, I present the application of multi-

copper homogeneous catalysts to phenol production via benzene hydroxylation using homogeneous mono- or binuclear copper catalysts with similar coordination environment. The effect of metal-metal interaction on phenols formation is investigated.

2.2.2. Experimental

The mononuclear copper catalyst (Cu1L) and the binuclear copper catalyst (Cu2L) were synthesized by stirring the methanol solution containing 2:1:1 and 1:1:1 molar ratio mixture of 4-tert-butyl-2,6-diformylphenol, trimethylenediamine, and $Cu(OAc)_2 \cdot H2O$, respectively [12]. The structures of Cu1L and Cu2L are illustrated in Figure 1. The samples were characterized by Fourier transform infrared spectroscopy (FT-IR) and extended X-ray absorption fine structure (EXAFS). FT-IR spectra were recorded on a NICOLET 380 spectrometer, with using KBr pellets (in solid form). X-ray absorption spectra at the Cu K-edge were measured at BL01B1 beamline of SPring-8. Commercially available CuO and synthesised $Cu[NH_3]_4(OH)_2$ were selected as reference materials for EXAFS investigations. The curve-fitting of EXAFS for the samples was conducted using REX2000 in r-space 1.0-3.5 Å. A typical oxidation procedure was as follows: benzene (2.8 mmol), catalyst (0.1 mmol), ascorbic acid (5.7 mmol), acetonitrile (2.0 mL), and acetic acid (0.5 mL) were charged into a glass batch reactor. The benzene hydroxylation was performed at 333 K in an

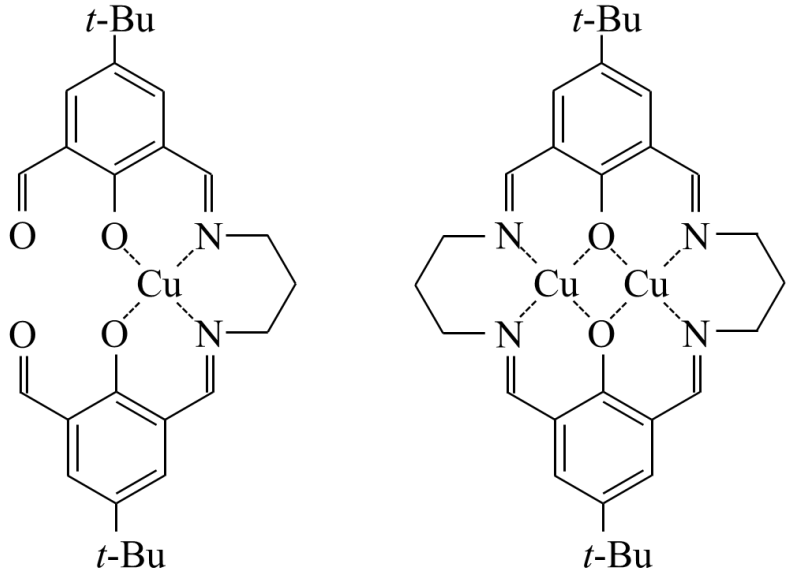

Figure 1. The structure images of Cu1L (a) and Cu2L (b).

oxygen atmosphere (0.4 MPa of gauge). The products were analysed using HPLC (Jasco MD-2010 Plus) equipped with a GH-C18 column.

2.2.3. Results and Discussion

The structures of the ligands in synthesised Cu1L and Cu2L were confirmed by FT-IR and EXAFS. FT-IR spectra of Cu1L and Cu2L show bands in the region 1,600–1,700 cm^{-1} (see Figure 2). Both Cu1L and Cu2L have an aromatic group due to 4-tert-butyl-2,6-diformylphenol being a precursor for the synthesis of the ligands. The spectrum of Cu1L also show two sharp peaks at 1,690 cm-1 and 1,640 cm-1, which were assigned to ν(C=O) and ν(C=N), respectively [12]. These peaks represent C=O bond derived from 4-tert-butyl-2,6-diformylphenol and C=N bond formed by a simple condensation of the other carbonyl group with one amino group of trimethylenediamine to give an iminophenol ligand. On the other hand, the spectrum of Cu2L exhibits the peak at 1,640 cm-1 assigned to C=N bond and quite a small peak at 1,690 cm-1 assigned to C=O bond. Therefore, Cu1L and Cu2L are similar with regards to the structures of ligands as illustrated in Figure 1. The Cu K-edge EXAFS was performed on Cu1L and Cu2L catalysts to investigate the coordination state of the Cu^{2+} centres. The Fourier transforms of the k^3-weighted EXAFS data for the synthesised Cu1L and Cu2L are shown in Figure 3. The parameters of the local structure of copper atoms retrieved from the EXAFS fitting are listed in Table 1. The

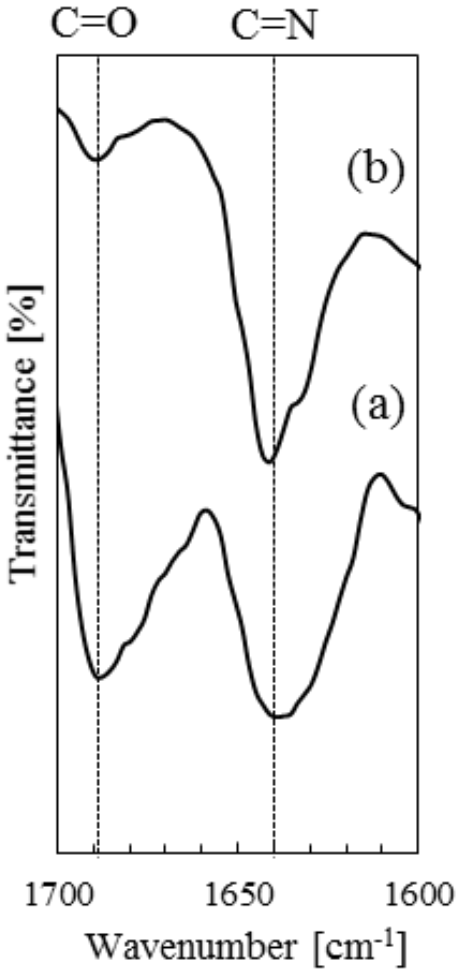

Figure 2. FT-IR spectra of Cu1L (a) and Cu2L (b).

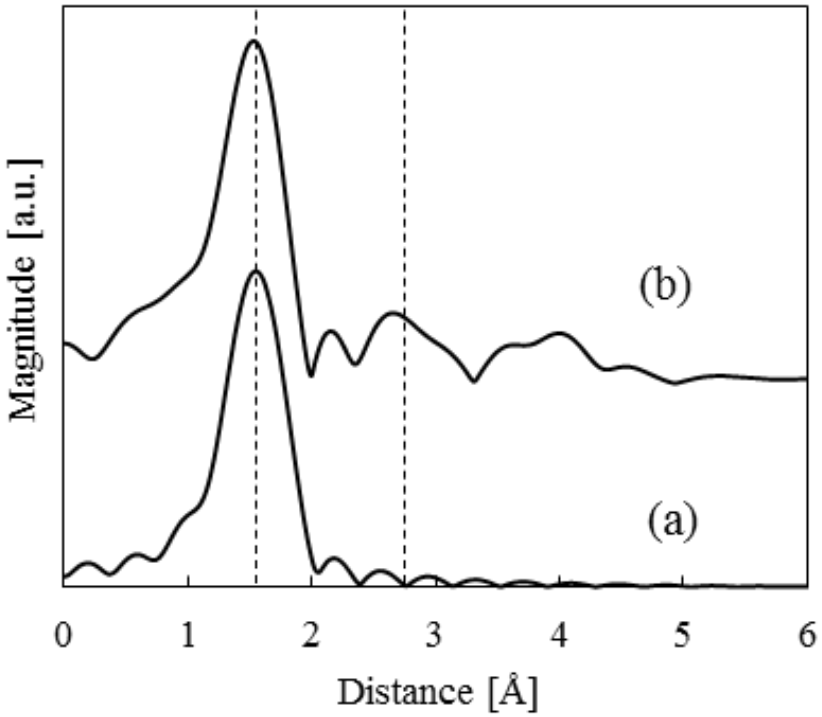

Figure 3. Radial distribution functions of the k^3-weighted Cu K-edge EXAFS data for Cu1L (a) and Cu2L (b).

Fourier transformed EXAFS data for Cu1L shows one major peak at ca. 1.5 Å (see Figure 3a), which is assigned to the first coordination shell consisting of oxygen (Cu-O) and nitrogen (Cu-N) atoms [13-16]. The atomic distances of Cu-O and Cu-N were 1.86 Å and 2.00 Å, respectively. The fitting data represents a coordination number of the Cu-N and Cu-O bonds (2.06 and 1.89, respectively), indicating two neighbouring nitrogen and two neighbouring oxygen atoms around the copper. Additionally, the peak assigned to the copper-copper bond (Cu-Cu) [12, 15] is not observed in the fitting data for Cu1L, indicating that copper atoms are mononuclear and is further confirmed by the ESR measured result. The Fourier transformed EXAFS data for Cu2L showed two major peaks at around 1.5 Å and 2.7 Å, respectively (Figure 3b). The fitting data represents a coordination distance and number for Cu-N, Cu-O, and Cu-Cu (see Table 1). The coordination number of Cu-Cu in Cu2L is calculated to be N = 0.83, indicating that a copper atom coordinates to another and it is therefore binuclear complex. Additionally, it can be suggested that Cu1L and Cu2L have the similar coordination structure except for the formation of a binuclear structure, because no significant difference in the parameters is obtained between Cu1L and Cu2L, except for Cu-Cu coordination.

The Cu1L and Cu2L catalysts with molecular oxygen were used for benzene hydroxylation. Phenol and hydroquinone were produced, whereas no formation of catechol and benzoquinone was observed. The yields of phenol and hydroquinone using Cu1L and Cu2L are shown in Table 2. Phenol is obtained in a yield of 33.4 μmol by using Cu2L, which is four times

Table 1. EXAFS fit parameters of local environment of copper atom for Cu1L and Cu2L.

Catalyst	Shells	Distance [Å]	Coordination number	σ^2 [Å^2]
Cu1L	Cu-O	1.86	1.89	0.0014
	Cu-N	2.00	2.06	0.018
	Cu-Cu	-	-	-
Cu2L	Cu-O	1.86	1.99	0.0025
	Cu-N	1.99	1.94	0.0045
	Cu-Cu	3.04	0.83	0.0030

σ: Debye-Waller factor.

Table 2. Yields of Phenol and Hydroquinone by using the Cu1L and Cu2L copper complex catalysts.

Catalyst	Yield [μmol]		Ph/Cu [-]	Hq/Cu [-]
	Phenol (Ph)	Hydroquinone (Hq)		
Cu1L	7.3	82.0	0.073	0.82
Cu2L	33.4	236.0	0.170	1.20

Reaction condition is as follows; benzene (2.8 mmol), copper catalyst (0.1 mmol), L-ascorbic acid (5.7 mmol), reaction time (5 h), reaction temperature (333 K).

higher than Cu1L (7.3 μmol). Hydroquinone is also obtained in a yield of 236.0 μmol by using Cu2L, which is three time higher than Cu1L (82.0 μmol). Ph/Cu and Hq/Cu were calculated as the ratio of product yields to copper content. It was confirmed that the Ph/Cu and Hq/Cu value were higher than 1 at the reaction time of 20 h in this reaction. Cu2L has the higher Ph/Cu and Hq/Cu than Cu1L. This indicates that active sites in Cu2L are more effectively activated for phenols production, especially for hydroquinone in comparison with Cu1L. It is speculated that metal-metal interactions between near copper atoms lead to improvement of the catalyst performance. A binuclear copper species may also easily activate the dissociation of molecular oxygen to two oxygen atoms in comparison with a mononuclear copper [17, 18].

2.2.4. Conclusion

Mono- and binuclear copper complexes were synthesised as catalysts for the hydroxylation of benzene. The FT-IR and EXAFS measurements indicated that mono- and binuclear complexes were successfully prepared. Hydroxylation of benzene to phenol and hydroquinone was carried out by using the synthesised mono- and binuclear copper complex catalysts with molecular oxygen, and it was obvious that the binuclear catalyst effectively produced phenol and hydroquinone due to metal-metal interactions.

References

1. T. Miyake, M. Hamada, Y. Sasaki, M, Oguri, *App. Catal. A*, 131 (1995) 33–42.
2. K. Nomiya, H. Yanagibayashi, C. Nozaki, K. Kondoh, E. Hiramatsu, Y. Shimizu, *J. M. Catal. A: Chem.*, 114 (1996) 181–190.
3. D. D. Devos, B. F. Sels, P. A. Jacobs, *Adv. Catal.*, 46 (2001) 1–87.
4. Y. Zhu, Y. Dong, L. Zhao, F. Yuan, *J. Mol. Catal. A: Chem.*, 315 (2010) 205–212.
5. J. Pan, C. Wang, S. Guo, J. Li, Z, Yang, *Catal. Commun.*, 9 (2008) 176–181.
6. F. Gao, R. Hua, *App. Catal. A*, 270 (2004) 223–226.
7. Y. Ichihashi, Y. Kamizaki, N. Terai, K. Taniya, S. Tsuruya, S. Nishiyama, *Catal. Lett.*, 134 (2010) 324–329.

A. Okemoto, Y. Inoue, K. Ikeda, C. Tanaka, K. Taniya, Y. Ichihashi, S. Nishiyama, *Chem. Lett.*, 43 (2014) 1734–1736.

8. M. Kirillov, M. V. Kirillov, A. J.L. Pombeiro, *Coordin. Chem. Rev.*, 256 (2012) 2741–2759.
9. S. Murahashi, N. Komiya, Y. Hayashi, T. Kumano, *Pure Appl. Chem.*, 73 (2001) 311–314.
10. T. Ohta, T. Tachiyama, K. Yoshizawa, T. Yamabe, T. Uchida, T. Kitagawa, *Inorg. Chem.*, 39 (2000) 4358–4369.
11. R. R. Gagné, C. L. Spiro, T. J. Smith, C. A. Hamann, W. R. Thies, A. K. Shiemke, *J. Am. Chem. Soc.*, 103 (1981) 4073–4081.
12. S. Mahapatra, J. A. Halfen, E. C. Wilkinson, G. Pan, X. Wang, V. G. Young, Jr., C. J. Cramer, L. Que, Jr., W. B. Tolman, *J. Am. Chem. Soc.*, 118 (1996) 11555–11574.
13. Y.-J. Huang, H. P. Wang, J. Lee, *Chemosphere*, 50 (2003) 1035–1041.
14. M. H. Groothaert, J. A. van Boknoven, A. A. Battiston, B. M. Weckhuysen, P. A. Schoonheydt, *J. Am. Chem. Soc.*, 125 (2003) 7629–7640.

15. I. Sanyal, K. D. Karlin, R. W. Strange, N. J. Blachburn, *J. Am. Chem. Soc.*, 115 (1993) 11259–11270.
16. S. Mahapatra, J. A. Halfen, E. C. Wilkinson, G. Pan, X. Wang, V. G. Young, Jr., C. J. Cramer, L. Que, Jr., W. B. Tolman, *J. Am. Chem. Soc.*, 118 (1996) 11555–11574.
17. T. Matsumoto, H. Furutachi, M. Kobino, M. Tomii, S. Nagatomo, T. Tosha, T. Osako, S. Fujinami, S. Itoh, T. Kitagawa, M. Suzuki, *J. Am. Chem. Soc.*, 128 (2006) 3874–3875.

Chapter 2.3. Reaction Mechanism of Liquid-Phase Oxidation of Benzene

2.3.1. Introduction

Phenol is known as one of the important chemical compounds in the fields of synthetic chemistry of petrochemicals and plastics, and is employed as an intermediate for production of phenolic resins and other phenol derivatives. Almost 90% of phenol production throughout the world is based on the cumene process which is an industrial process for developing phenol and acetone from benzene and propylene [1,2]. It consists of three production processes and has some disadvantages of environmental burden, consumption of high energy, and explosive intermediate product, that is, cumene hydroperoxide. The attractive effort of producing phenol from benzene by direct oxidation has received much attention.

The direct production of phenol through direct insertion of oxygen into the C-H bond is challenging method and has been studied by many researchers [3-6]. Previous works often described the direct production of phenol using hydrogen peroxide and other oxidising reagents [7-9]. Today, one challenge is employment of molecular oxygen for direct oxidations as an easily handled oxidising reagent with the lowest cost and danger. Molecular oxygen normally exists in a triplet state, which can only proceed

chemical reactions with general substrate molecules in a singlet state by the spin-forbidden transition in molecular. I have reported that the reaction system of vanadium complexes with molecular oxygen can catalyse the direct oxidation of benzene to phenol [10]. It describes the liquid-phase oxidation of benzene over supported vanadium catalysts with molecular oxygen as an oxidant and acetic acid solution as a solvent by using several reducing agents. Our interest driven from the previous studies is to understand the mechanism of activation of ground-state oxygen on vanadium-complex catalyst system that is needed to develop the practical and sustainable oxidation system. Density functional theory (DFT) methods are helpful tools for investigation on the mechanism of catalytic reactions [11-13]. Computational chemistry is becoming much more easily available for investigating reaction pathways by a dramatic development of DFT study and computer science. Successful efforts based on DFT study have been performed for mechanism investigation of organic reactions, such as Fisher esterification [14], CO oxidation [15], and methane oxidation [16]. Although its application has widely spread in the field of catalytic chemistry, no study on mechanism has been reported for the vanadium ion-catalysed oxidation of benzene using molecular oxygen. Based on our previous experimental work, DFT calculations are used to discuss both the feasibility of the experimentally proposed intermediates and their possible participation in the vanadium ion-catalysed oxidation using molecular oxygen. In this work, DFT calculation study reviews the pathway of oxygen activation via the vanadium ion-catalysed reaction, and attempts to provide conceptual

mechanism interpretation. The mechanism of vanadium ion and chelate catalysis of the oxidation is examined from the point of view of applying it toward a better understanding of the reaction in the oxygen oxidation system.

2.3.2. Experimental

2.3.2.1. Reagents

Oxovanadium sulfate ($VOSO_4$), benzene, sucrose, acetic acid, methanol and several ligands (benzoic acid, *p*-aminobenzoic acid, *p*-hydroxybenzoic acid, *p*-methylbenzoic acid, *p*-chrolobenzoic acid and *p*-nitrobenzoic acid) were purchased from Nacalai Tesque. Faujasite-type zeolite was obtained from ZEOLYST. All reagents and solvents were used as received without further purification.

2.2.2.2. Catalysts preparation

Faujasite-type zeolite H-Y (Si/Al = 4.8, ZEOLYST) was added to aqueous $VOSO_4$ solution in a 500 ml flat-bottom flask equipped with reflux condenser and stirred at 353 K for 48 h. The obtained solid was filtered, washed with 2 liters of hot water and dried at 393 K overnight. The obtained solid, which is oxovanadium ions anchored Y-type zeolite, were named V-Y.

Vanadium complexes encapsulated in Y zeolite catalysts was prepared by Ship in a bottle method [10,17]. The oxovanadium ion Y zeolite anchored (V-Y) and each ligand (benzoic acid, *p*-aminobenzoic acid, *p*-hydroxybenzoic acid, *p*-methylbenzoic acid, *p*-chrolobenzoic acid and *p*-nitrobenzoic acid) were added in methanol. The mixture was refluxed with stirring at 333 K for 20 h, then filtered, washed with methanol and dried at 393 K overnight. The obtained solid was stirred in methanol solution once again to remove an unreacted oxovanadium ion and ligands on the surface of Y-zeolite. The resulting materials were designated as vanadium complex catalysts encapsulated in Y-zeolite; VBA-Y, VABA-Y, VHBA-Y, VMBA-Y, VCBA-Y, and VNBA-Y which were prepared by using benzoic acid, *p*-aminobenzoic acid, *p*-hydroxybenzoic acid, *p*-methylbenzoic acid, *p*-chrolobenzoic acid, and *p*-nitrobenzoic acid, respectively. The ligand impregnated Y-zeolite was prepared as follows; H-Y zeolite and picolinic acid were stirred with methanol, evaporated to dry at 333 K in a hot water bath and then dried at 393 K. The obtained solid was designated as Ligand/H-Y.

2.3.2.3. Catalyst test

Selective oxidation of benzene to phenol in the liquid phase was performed using a glass pressure-proof reactor. Benzene (5.6 mmol), the catalyst (100 mg), and sucrose (0.4 mmol) were added to an acetic acid aqueous solution (5 ml, 20 vol%) in the reactor and magnetically stirred.

The reactor was purged with 0.4 MPa of O_2 (gauge pressure) and then heated at 353 K with stirring for 20 h. A mixed solution of toluene (0.2 ml) and 2-propanol (5 ml) was added to the reaction solution as an internal standard. The mixture was centrifuged to recovery the catalyst from the solution, and the used catalyst was sufficiently washed with acetone and dried at 393 K overnight. The liquid phase products were analyzed by high-performance liquid chromatograph (Jasco MD-2010 Plus) equipped with GH-C18 column. The recycling test was carried out using the used catalyst from the mixture, which was centrifugally separated from the reaction solution, washed with acetone thrice and dried at 393 K overnight.

Quantitative determination of hydrogen peroxide during the reaction was performed under the standard condition of catalyst test in the absence of benzene as a substance. After the reaction for arbitrary time, an amount of the formed hydrogen peroxide was quantitatively measured by titrimetric analysis using potassium permanganate.

2.3.2.4. Characterisation

Vanadium content in the catalyst was measured by XRF (Rigaku Primini) equipped with Pd as X-ray source. Thermogravimetric and differential thermal analysis (TG-DTA) was carried out with DTG-60 (SHIMAZU). The samples were heated up to 1173 K at 10 K/min in air flow for the TG-DTA measurement.

2.3.2.5. Computational methods

All theoretical calculations described here were performed using the Gaussian 09 program [18]. The structures of catalysts and intermediates were optimised using the density function theory (DFT) method at the B3LYP/6-31G* computational level [19-21]. The corresponding vibrational frequencies of the reactants, products, and transition states structure were also calculated at the same level. Moreover, the intrinsic reaction coordinate (IRC) calculations were performed at the level to confirm each transition state correctly connects to the desired reactants and products. It was confirmed that the reactants, intermediates, and products had no imaginary frequencies, whereas transition states had just one imaginary frequency [22].

2.3.3. Results and Discussion

2.3.3.1. Catalysts Characterization

Chemical composition of several zeolite samples measured by XRF and physical surface area by the BET method are presented in Table 1.

The diffuse reflectance UV-Vis spectra of benzoic acid derivative vanadium complex catalysts in Y-zeolite and V-Y were recorded at room temperature in the region 200-600 nm and shown in Figure 2. Within the

Table 1. Chemical composition and specific surface area of the encapsulated vanadium complex catalysts.

Catalyst	V content (mmol/g)	BET surface area (m^2/g)
H-Y	-	702
V-Y	0.89	343
V(BA)-Y	0.70	405
V(ABA)-Y	0.59	455
V(HBA)-Y	0.57	463
V(MBA)-Y	0.62	437
V(CBA)-Y	0.70	389
V(NBA)-Y	0.68	420

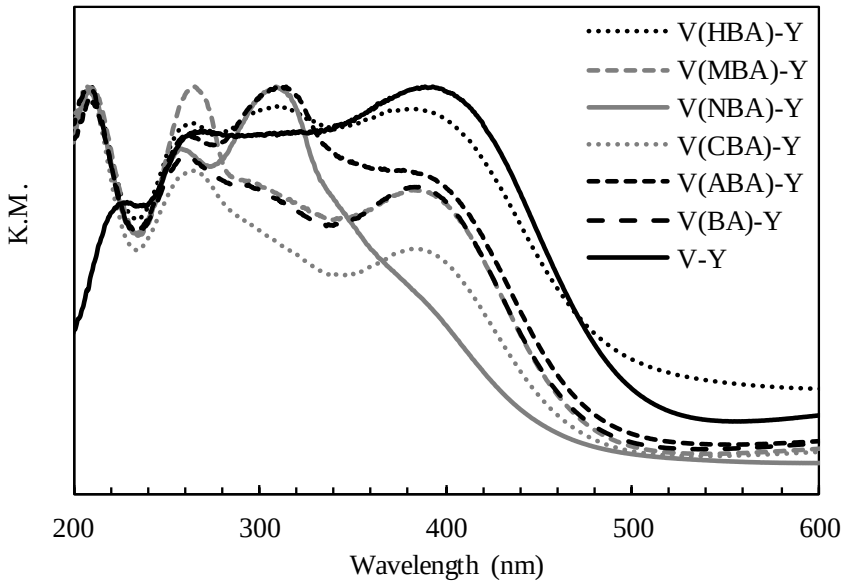

Figure 2. UV-Vis DR spectra of various vanadium catalysts.

spectrum of V-Y, the high absorption is observed at the range 400 nm which assigned to distorted tetrahedral vanadium species of crystalline vanadium oxide [23,24], and no peak appears at 200 nm. All UV-Vis spectra of benzoic acid derivative vanadium complex catalysts in Y-zeolite exhibit an absorption at 200 nm due to π-π* transition of benzoic acid derivatives. Moreover, these spectra, in particular V(NBA)-Y, shows two strong absorption bands at the range 250-300 nm which are assigned to isolated monomeric tetrahedral vanadium species [25,26], and the weak absorption at 400 nm. It indicates coordination of ligands to vanadium species causes isolation of vanadium species associated with the formation of vanadium complexes.

Thermal gravimetric analyses of the encapsulated vanadium complexes were studied using DTA-TG (Figure 3). The spectrum of V-Y shows slight weight loss in the wide temperature range 500–1000 K due to the loss of chemisorbed water in the form of OH groups in Y-zeolite [27]. The two encapsulated complexes V(BA)-Y and V(NBA)-Y show almost similar decomposition patterns in the temperature range 600–800 K, which is assigned to the to the loss of the ligands. The small percent weight loss (4–6%) almost corresponds to the coordinating ligands in vanadium complexes.

2.3.3.2. Catalyst test

The selective benzene oxidation to phenol was carried out in an aqueous solution of acetic acid using a glass batch reactor. The result of

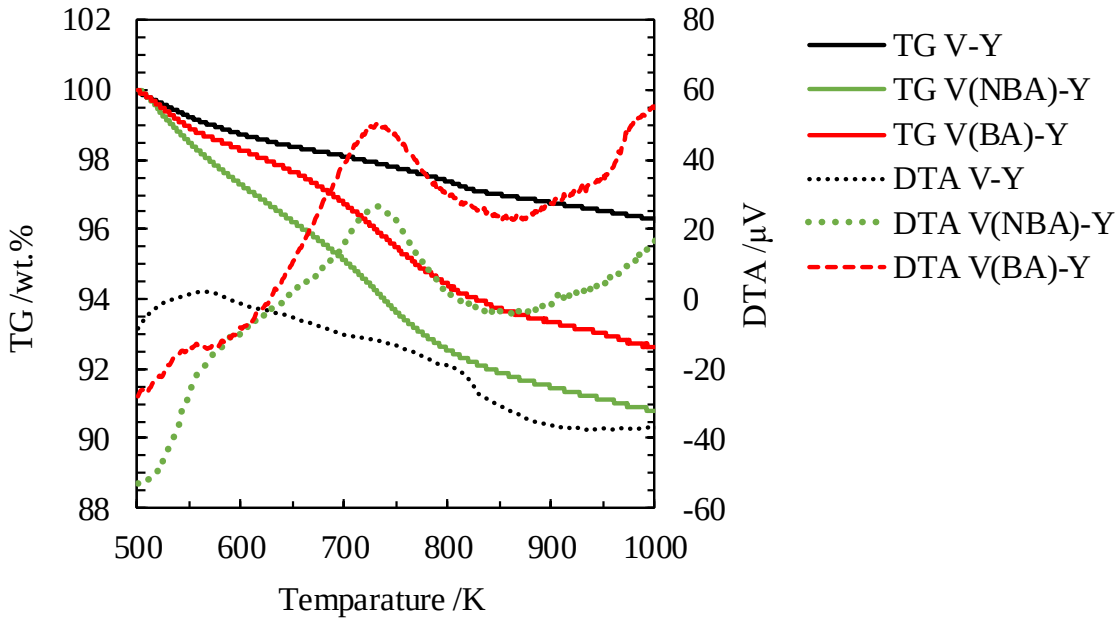

Figure 3. DTA-TG spectra of V-Y, V(BA)-Y, and V(NBA)-Y by heating from 500 K to 1000 K and holding at 1000 K for 5 min. Flow rate: N_2/O_2 = 100/25 (ml/min); ramping rate of temperature:10 K/min.

phenol formation catalysed by several vanadium complex encapsulated in Y-zeolite and the vanadium content of the catalysts measured by XRF are shown in Table 2. Phenol was the major product over all catalysts. In a blank experiment, which is performed without any catalyst, less than 0.1 mmol of phenol were observed. H-Y showed a minuscule amount of phenol (Entry 1), whereas all the catalysts containing vanadium species gave good yield of phenol in the region of 1.78–3.45 mmol/g-cat (Entry 2–8). V(NBA)-Y, which had nitric acid as a ligand, showed the highest activity in all the catalysts. On the other hand, the activity of V(ABA)-Y and V(BA)-Y were as low as 1.44 mmol/g-cat. After each reaction cycle, the catalyst was recovered by centrifugation, washed properly with acetone, dried overnight, and then used for the reaction again under identical reaction condition. The reused V-Y showed significant decrease of phenol yield and only 13% of the reusability. The reused vanadium complex catalysts encapsulated in Y-zeolite showed good yield in Run 2, especially V(NBA)-Y had 80% of the reusability. These results revealed encapsulation of vanadium complexes in Y-zeolite allowed us to prevent the active species from leaching into the reaction solvent. And also, these electron-withdrawing and electron-donating substituted ligands allow us to improve the catalytic activity and reusability of vanadium complex catalysts encapsulated in Y-zeolite. A ligand has a great influence on the yield of phenol, which is due to the electronic effect. The phenol formation activity of the used V-Y catalyst (Run 2 in Table 2) shows a marked decrease in comparison with that of the fresh V-Y catalyst. On the other hand, the used

Table 1. Phenol production activity catalyzed various vanadium catalysts.

Entry	Catalyst	V content (mmol/g-cat)	Yield of Phenol (mmol/g-cat)		TON[b]	Reusability[c] [%]
			Run 1	Run 2[a]		
1	H-Y	0.00	0.40	0.36	-	90
2	V-Y	0.89	2.25	0.29	2.5	13
3	V(ABA)-Y	0.68	1.44	0.89	2.1	62
4	V(HBA)-Y	0.70	1.78	1.12	2.5	63
5	V(MBA)-Y	0.57	3.04	2.35	5.3	77
6	V(BA)-Y	0.68	1.44	0.89	2.1	62
7	V(CBA)-Y	0.62	2.15	1.65	3.5	77
8	V(NBA)-Y	0.59	3.45	2.76	5.8	80

Reaction condition: Benzene; 0.56 mmol, Catalyst; 100 mg,

[a]Phenol production activity of the reused catalysts

[b]Turn over number = phenol yield (mol) / vanadium content (mol)

catalyst shows a higher phenol formation activity than that of the used catalyst although the phenol formation activity of the used catalyst is slightly lower than that of the fresh catalyst. These results indicate that the encapsulation of vanadium complexes in the Y-zeolite supercage has prevented the vanadium complexes from leaching into the reaction solution, and that the catalyst can be effectively used as a heterogeneous catalyst.

In previous study, it was reported that hydrogen peroxide was generated during the reaction by transition metal catalysts in the presence of oxygen and a reducing agent [28]. It was suggested that hydrogen peroxide formed as the reaction intermediate through catalytic activation of oxygen and worked for the benzene oxidation. The formation of hydrogen peroxide was quantitatively examined in the reaction of oxygen activation by various vanadium complex catalysts. Figure 3 shows the relationship between the formation of phenol and hydrogen peroxide. The catalytic performance of phenol formation is related to positive correlation with hydrogen formation. This result supports the hypothesis that hydrogen peroxide was formed as the intermediate through oxygen activation. Also, it reveals that each catalyst has a different amount of hydrogen peroxide, and ligand of vanadium complex influences strongly on the catalytic performance of oxygen activation.

2.3.3.3. Computational Studies

Hybrid density functional calculations (B3LYP/LANL2DZ) were

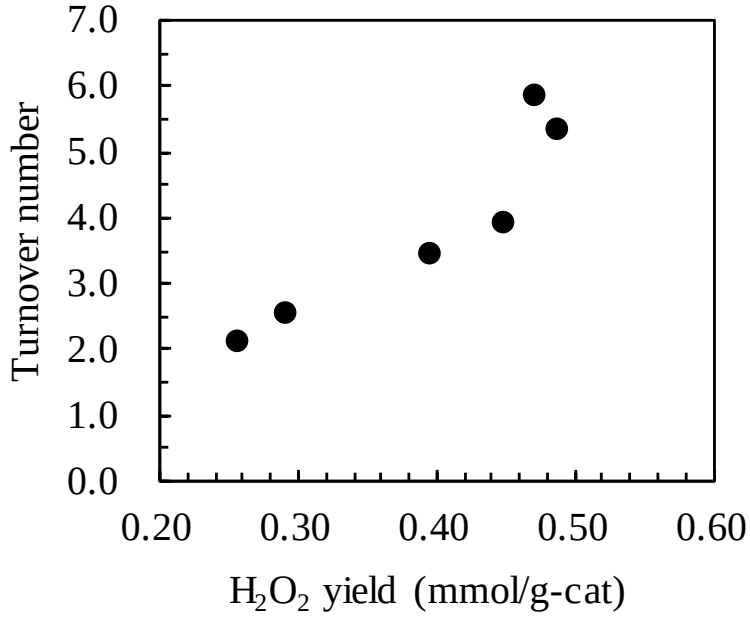

Figure 3. Relationship between H_2O_2 formation yield and turnover number of phenol formation by various vanadium complex catalysts.

performed using Gaussian 09. The interaction of vanadium complexes with molecular oxygen was studied. Figure 4 exhibits the coordination arrangement of the vanadium complex V(BA). Each bidentate ligand contributes with two coordination sites $[V=O]^{2+}$. Thus, vanadium centre has a coordination number five, giving a distorted pyramidal geometry. It was confirmed that the coordination distance between the atoms V-O around the atoms of vanadium range from 1.60(22) (corresponding to the double bond of the vanadyl oxygen) to 2.05(25) Å (the single bond character). The value was found to be within the range of bond lengths of V–O expected, according to data of the literature [29].

It is known that the oxidation-reduction of vanadium is very important to the understanding of the vanadium catalysis. The benzene hydroxylation by a vanadium complex catalyst requires a reducing reagent, and reduction of the catalyst during the reaction is confirmed by UV-vis spectroscopy. The reduction is slow, and therefore, the step is supposed to be one of the major elementary processes that determine the reaction rate of progress. The V(IV)/V(III) reduction was simulated using DFT calculations. Figure 5 shows the energy gap between V(IV)/V(III) reduction of several vanadium complexes and their catalytic performance in the benzene hydroxylation. Among them, vanadium nitrobenzoate V(NBA), which has the highest activity, exhibits the lowest energy gap of 1.13 eV, and the result is a negative correlation tracing a downward line. It reinforces a significant effect of the reduction process on the catalytic performance, DFT calculations to describe ligand effects can provide very good result if the ligand is adequately chosen.

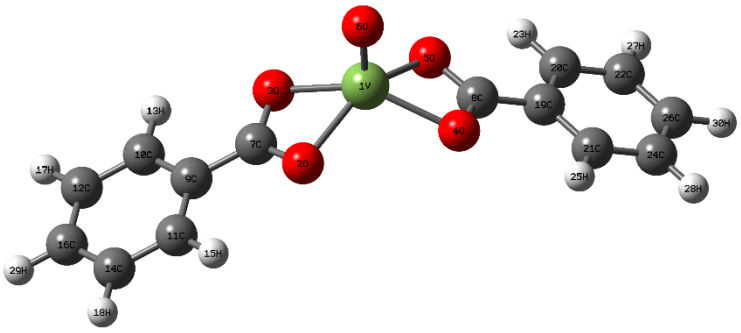

Figure 4. the coordination arrangement of the vanadium complex V(BA) that is coordinated with two molecules of benzoic acid as ligands.

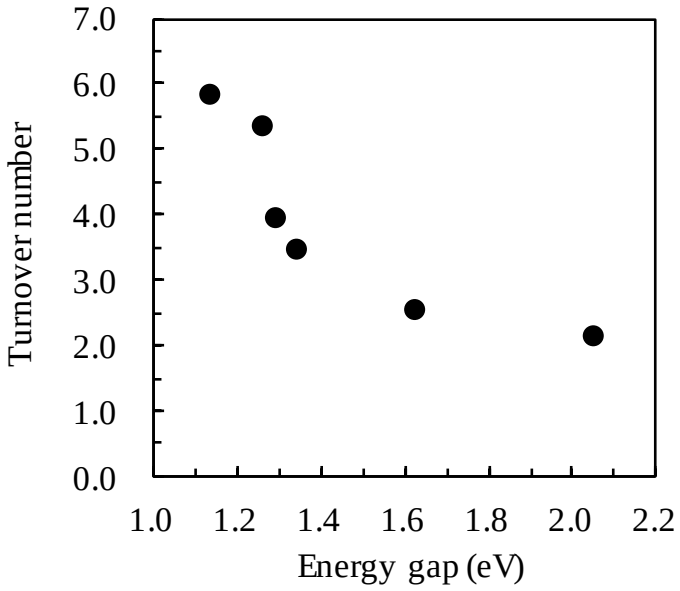

Figure 5. Relationship between H_2O_2 formation and energy gaps between V(III) and V(IV) vanadium complexes by DFT calculation.

Similar efforts have been made to estimate the free energy difference in the oxidation process form theoretical calculations [30]

A detailed simulation of reaction pathways is required to clarify the complicated reaction mechanism for reaction controlling of selective oxidations with molecular oxygen. The microscopic mechanism for the benzene hydroxylation with molecular oxygen has remained unclear yet. A theoretical procedure might be used to predict their mechanism and understand the reactivity. Possible pathways for the activation of oxygen oxidation over vanadium dibenzoate V(BA) are shown in Scheme 1. Path 1 involves a process of the O_2 side-on adsorption on vanadium complex. First, molecular oxygen interacts with the vanadium centre, which is activated by +4.0 kJ/mol to form (**1-2TS**). Subsequently, (**1-3**) is stabilized by cleavage and rearrangement of the oxygen double bond. In path 2, molecular oxygen is adsorbed on vanadium centre with the side-on mode. Interestingly, molecular oxygen absorbed with the side-on mode (**2-2**) is more stable than (**1-2**) of the end-on mode. The structure of (**2-2TS**) is optimised in the singlet states, the energy is calculated to be +0.003 kJ/mol. Therefore, the catalytic cleavage of the oxygen double bond immediately proceeds through (**2-2TS**), followed by the formation of the vanadium peroxydibenzoate intermediate. Then, hydrogen peroxide is released from it via transition state with activation energy of 106 kJ/mol. It should be noted that the formation of hydrogen peroxide is supported by experimental studies. From these results, the energies for the activation of molecular oxygen on the V(BA) catalyst are required with 4.0 kJ/mol at **1-2TS** in path

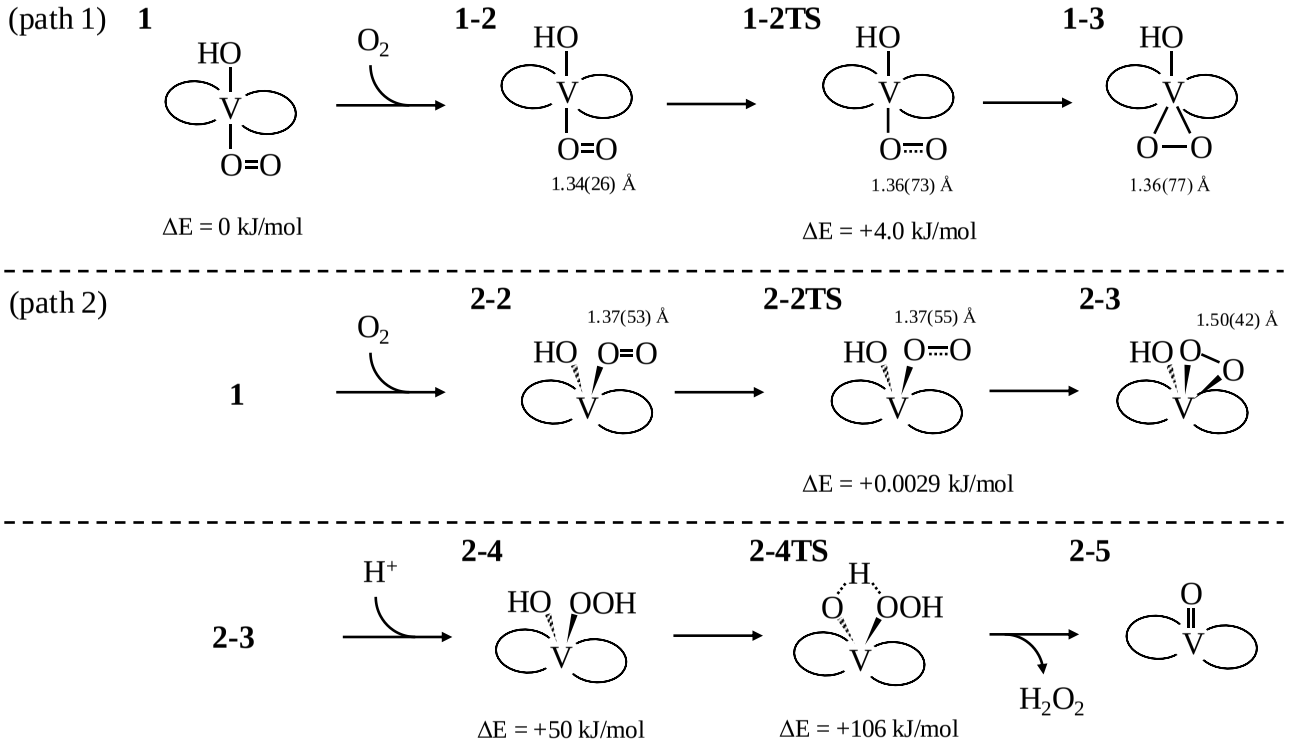

Scheme 1. Possible reaction coordinates for the O_2 activation by a vanadium complex with end-on (path 1) and side-on (path 2) adsorption modes.

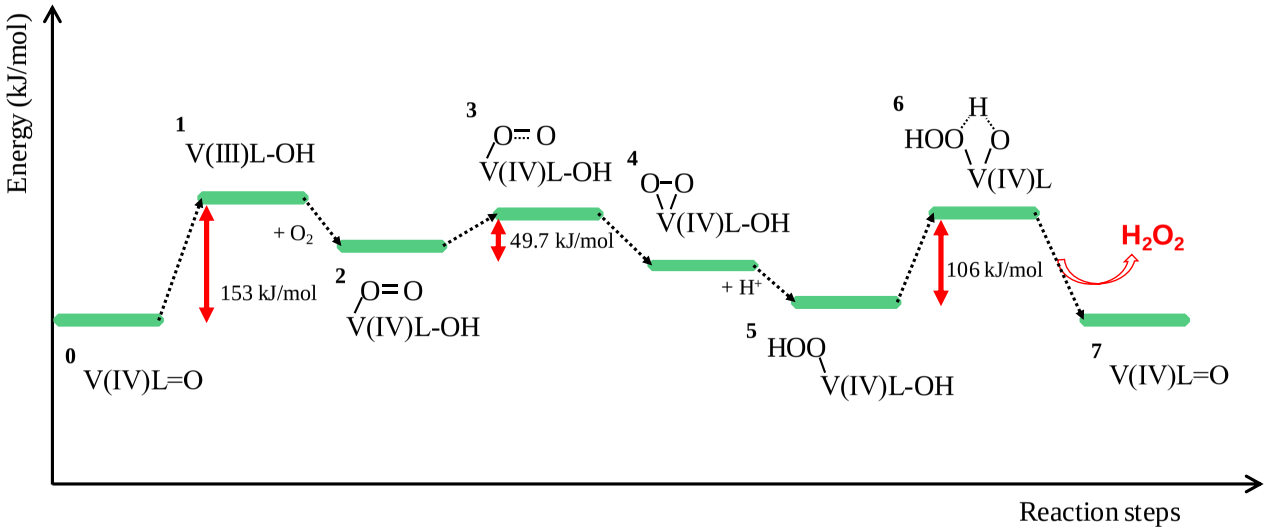

Figure 6. Energy diagram in the activation process of molecular oxygen over the vanadium complex catalyst.

1, and 4.0 kJ/mol at **2-2TS** in path 2. Then, the energy for the formation of hydrogen peroxide is required with 106 kJ/mol. Overall reaction coordinates in oxygen activation on V(BA) are shown in Figure 6. As shown in Figure 6, the relative high activation energy is required with 153 kJ/mol at **1**. The result supports data indicating the energy gap between V(III)/V(IV) are related with the catalytic performance. The activation energy of oxygen by the reduced vanadium complex is 140 kJ/mol, and the value is close to the actual enthalpy of the hydrogen peroxide formation, suggesting that the process can be simulated by theoretical procedures [31]. According to the collected data, a few reaction sequences can be assigned to be the pathway in the vanadium ion-catalysed oxidation using molecular oxygen. The most feasible mechanism is shown in Scheme 2 with their energy profiles. Starting from reduction step of the vanadium(IV) complex, pathway s) has a higher overall barrier, but a) does the lower individual energy barrier. With the formation of hydrogen peroxide, pathway c) has relatively higher of all individual barriers, suggesting the pathway a) seems to be a rate determining step in series of pathways of the V(BA) catalyst.

Finally, the oxidation process of benzene was investigated by DFT calculations. Proposed reaction coordinates for benzene oxidation by a vanadium complex are illustrated in scheme 3. In path 3, hydrogen peroxide oxidises the V(IV) complex **5-1** to the V(V) complex **5-2**, and the formed V(V) complex works for benzene oxidation to phenol. On the other hand, in path 4, the reaction intermediate **5** immediately reacts with benzene. Energy diagram of each pathways estimated by DFT calculations is shown

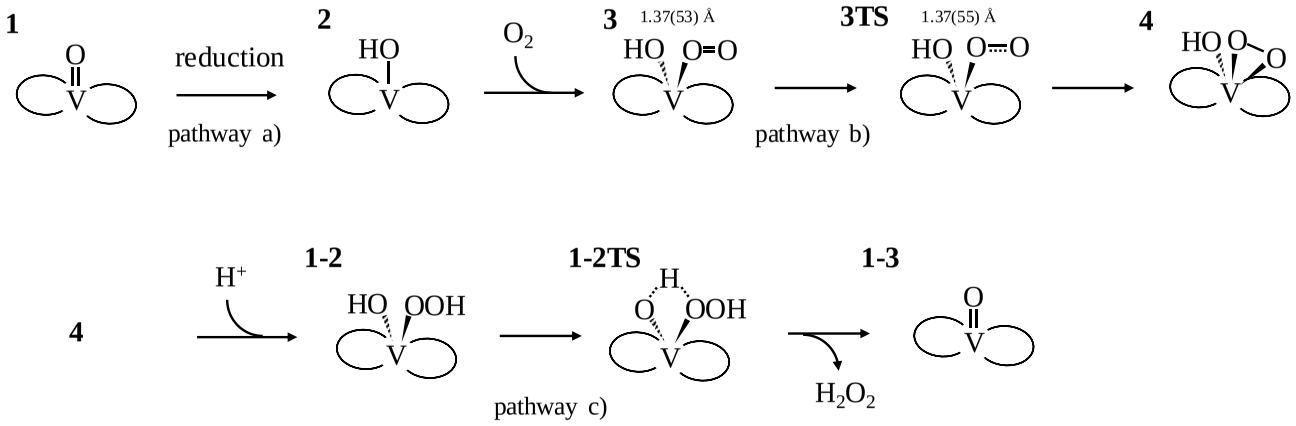

Scheme 2. The most feasible mechanism for the O_2 activation by a vanadium complex.

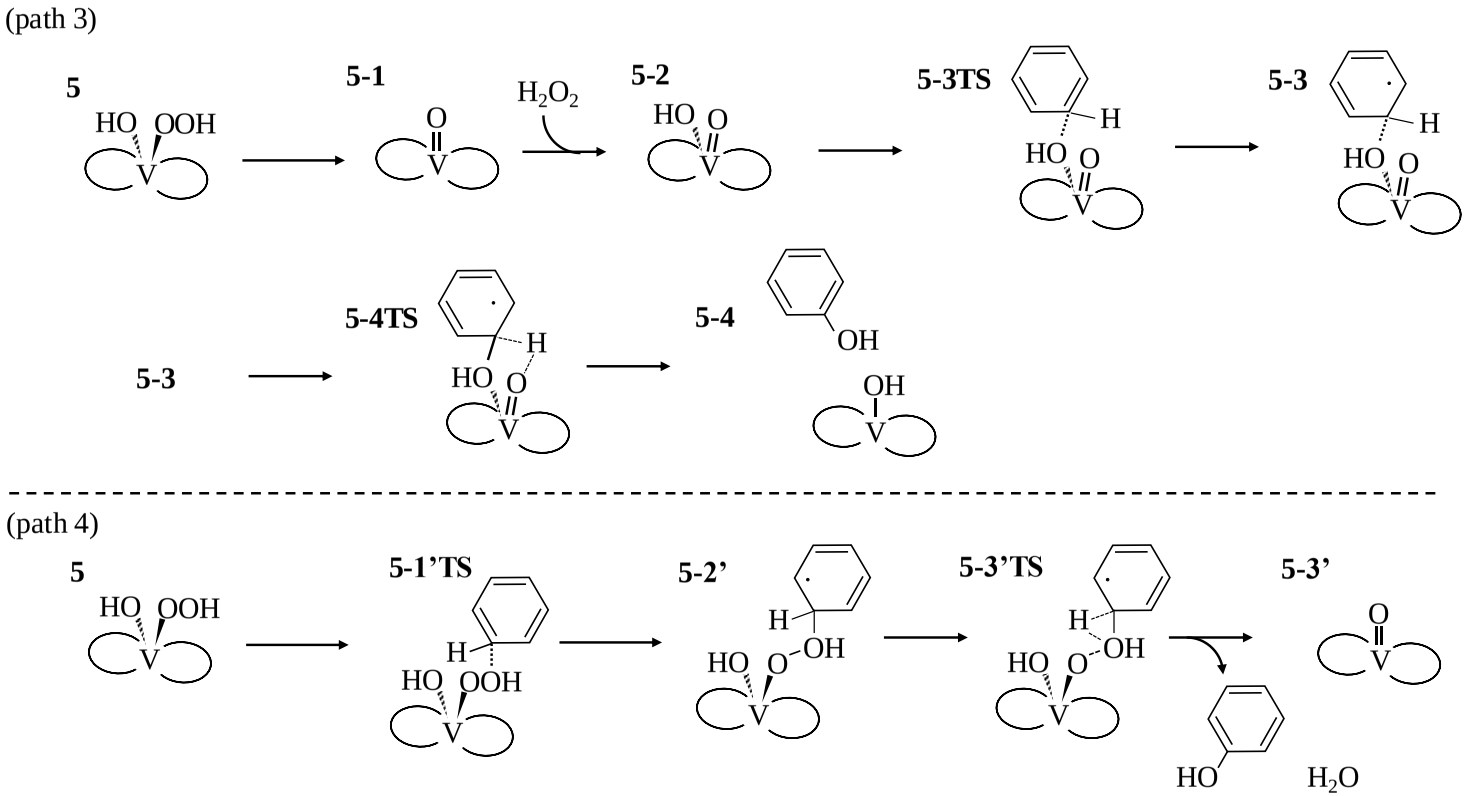

Scheme 3. Possible reaction coordinates for benzene oxidation by a vanadium complex.

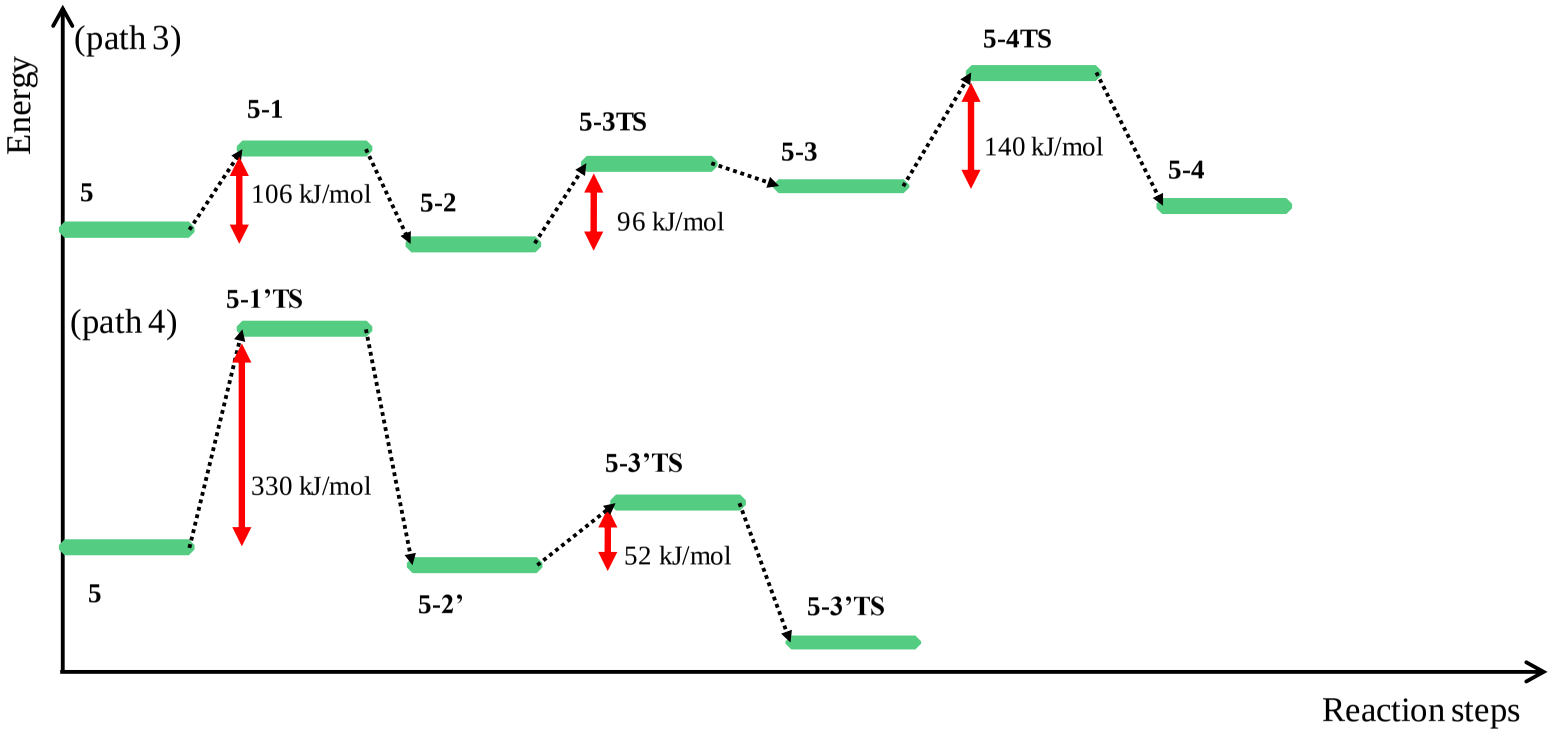

Figure 7. Energy diagram in the oxidation process of benzene over the vanadium complex catalyst.

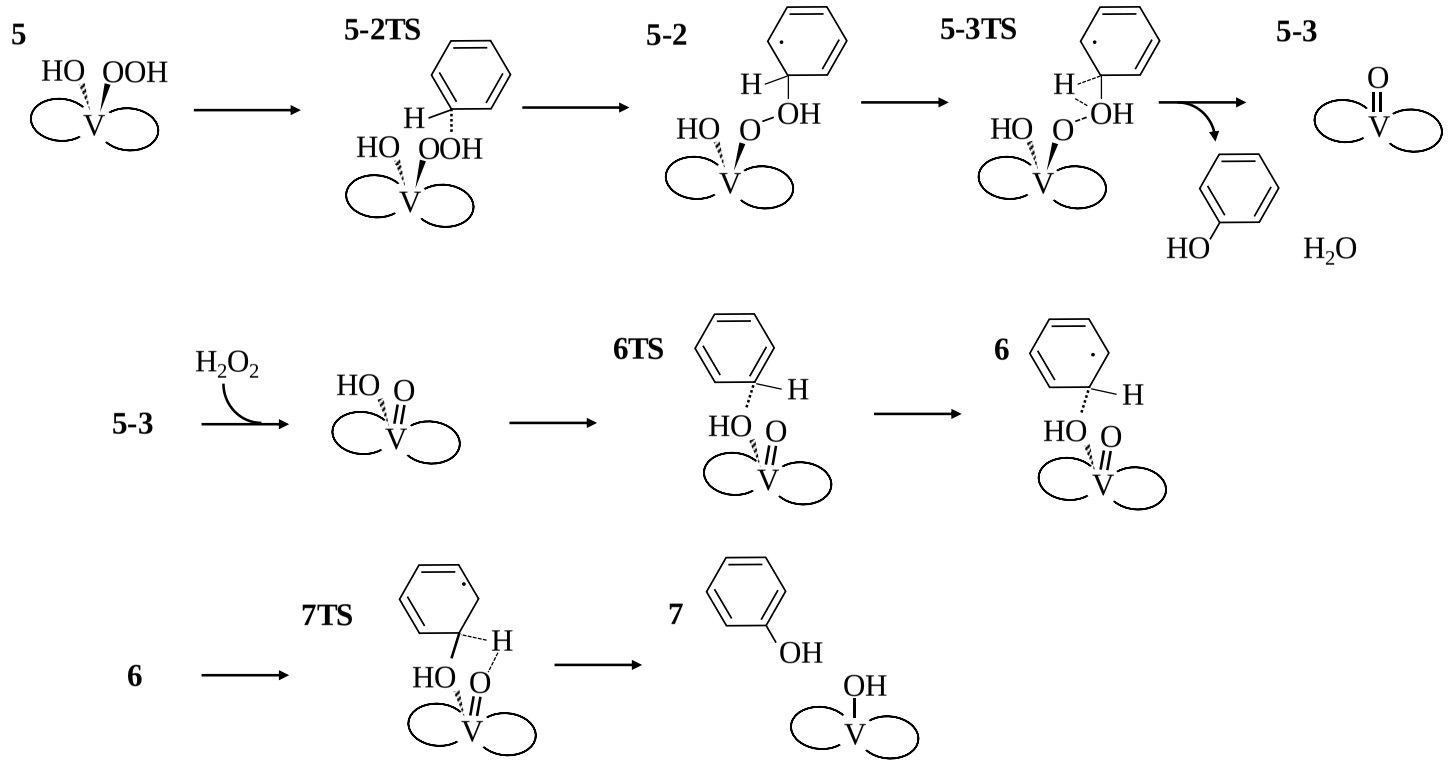

Scheme 4. The most feasible mechanism for the stage of benzene oxidation by a vanadium complex.

in Figure 7. It is obvious that path 4 has extremely high activation energy of 330 kJ/mol in formation of the reaction intermediate **5-1'TS**. Path 3 has activation energy of 160 kJ/mol at most. Path 3 is the process in which V(V) complex is formed, and formation of V(V) was indeed observed during the reaction by UV-vis spectroscopy. Therefore, path 3 is the better feasible mechanism for the stage of benzene oxidation by a vanadium complex.

2.3.4. Conclusion

The selective oxidation of benzene to form phenol was performed by vanadium ion-catalysed system using sucrose as a reducing reagent and molecular oxygen as an oxidising reagent. Encapsulation of vanadium complex in supercage of Y-zeolite by Ship in a bottle method allowed to heterogeneous vanadium complex catalysts that showed effective formation of phenol with excellent reusability of the used catalyst. Also, effect of ligands on the catalytic performance was studied experimentally and theoretically, and the catalytic property depends on the formation rate of hydrogen peroxide as a reaction intermediate through redox cycle between V(III)/V(IV). Furthermore, the activation mechanism of molecular oxygen catalysed by the vanadium complex in this reaction was investigated theoretically using the B3LYP/6-31G* calculations. The different reaction pathways were mapped out, and the computational results revealed that the reaction subsequences including five steps to form hydrogen peroxide with

the energy barrier of 106 kJ/mol at the most. The detailed mechanisms should be helpful for a better understanding oxygen oxidations, and can provide some valuable insights to design the suitable metal complex catalysts for this type of reaction in future.

References

1. A. Chudinova, A. Salischeva, E. Ivashkina, O. Moizes, A. Gavrikov, *Procedia Chem.*, 15 (2015) 326–334.
2. Y. Zhuo, Y. Zhong, Y. Xu, Y. Sha, *Ind. Eng. Chem. Res.*, 55 1 (2016) 257–266.
3. T. Miyake, M. Hamada, Y. Sasaki, M. Oguri, *Appl. Catal. A: Gen.*, 131 (1995) 33–42.
4. T. Dong, J. Li, F. Huang, L. Wang, J. Tu, Y. Torimoto, M. Sadakata, Q. Li, *Chem. Commun.*, (2005) 2724–2726.
5. A. Okemoto, K. Kato, K. Taniya, Y. Ichihashi, S. Nishiyama, *Chem. Lett.*, 44 *2015* 384–386.
6. A. Okemoto, Y. Tsukano, A. Utsunomiya, K. Taniya, Y. Ichihashi, S. Nishiyama, *J. Mol. Catal. A: Chem.*, 411 (2016) 372–376.
7. T. Miyahara, H. Kanzaki, R. Hamada, S. Kuroiwa, S. Nishiyama, S. Tsuruya, *J. Mol. Catal. A: Chem.*, 176 (2001) 141–150.
8. J. Pan, C. Wang, S. Guo, J. Li, Z. Yang, *Catal. Commun.*, 9 (2008) 176–181.

9. Y. Zhua, Y. Donga, L. Zhaoa, F. Yuan, *J. Mol. Catal. A: Chem.*, 315 (2010) 205–212.
10. A. Okemoto, Y. Inoue, K. Ikeda, C. Tanaka, K. Taniya, Y. Ichihashi, S. Nishiyama, *Chem. Lett.*, 43 (2014) 1734–1736.
11. Y. Wang, D. Wei, Y. Zhu, P. Liu, M. Tang, *Comput. Theor. Chem.*, 1018 (2013) 85–90.
12. C. Q. Lv, C. Liu, G. C. Wang, *Catal. Commun.*, 45 (2014) 83–90.
13. H. Kobayashi, S. Higashimoto, *Appl. Catal. B: Environ.*, 170–171 (2015) 135–143.
14. M. Vafaeezadeh, A. Fattahi, *Comput. Theor. Chem.*, 1071 (2015) 27–32.
15. Y. L. Song, L. L. Yin, J. Zhang, P. Hu, X. Q. Gong, G. Lu, *Surf. Science*, 618 (2013) 140–147.
16. M. Drees, S. A. Hauser, M. Cokoja, F. E. Kühn, *J. Organomet. Chem.*, 748 (2013) 36–45.
17. S. Yamaguchi, T. Fukura, C. Fujita, H. Yahiro, *Chem. Lett.*, 41 (2012) 713.
18. M. J. Frisch, G. W. Trucks, H. B. Schlegel, G. E. Scuseria, M. A. Robb, J. R. Cheeseman, G. Scalmani, V. Barone, B. Mennucci, G. A. Petersson, H. Nakatsuji, M. Caricato, X. Li, H.P. Hratchian, A.F. Izmaylov, J. Bloino, G. Zheng, J. L. Sonnenberg, M. Hada, M. Ehara, K. Toyota, R. Fukuda, J. Hasegawa, M. Ishida, T. Nakajima, Y. Honda, O. Kitao, H. Nakai, T. Vreven, J.A. Montgomery Jr., J. E. Peralta, F. Ogliaro, M. Bearpark, J. J. Heyd, E. Brothers, K. N. Kudin, V. N. Staroverov, T. Keith, R. Kobayashi, J. Normand, K. Raghavachari, A. Rendell, J. C. Burant, S. S. Iyengar, J.

Tomasi, M. Cossi, N. Rega, J.M. Millam, M. Klene, J. E. Knox, J. B. Cross, V. Bakken, C. Adamo, J. Jaramillo, R. Gomperts, R. E. Stratmann, O. Yazyev, A. J. Austin, R. Cammi, C. Pomelli, J. W. Ochterski, R. L. Martin, K. Morokuma, V. G. Zakrzewski, G. A. Voth, P. Salvador, J. J. Dannenberg, S. Dapprich, A. D. Daniels, O. Farkas, J. B. Foresman, J. V. Ortiz, J. Cioslowski, D. J. Fox, Gaussian 09, Revision D.01, Gaussian, Inc., Wallingford CT, 2013.

19. A. D. Becke, *J. Chem. Phys.*, 98 (1993) 5648−5652.
20. B. Miehlich, A. Savin, H. Stoll, H. Preuss, *Chem. Phys. Lett.*, 157 (1989) 200−205.
21. C. Lee, W. Yang, R. G. Parr, *Phys. Rev. B*, 37 (1988) 785−789.
22. J. Huang, C. He, L. Wu, H. Tong, *Chem. Phys. Lett.*, 658 (2016) 114–124.
23. M. Morey, A. Davidson, H. Eckert, G. Stucky, *Chem. Mater.*, 8 (1996) 486–492.
24. I. E. Wachs, *Catal. Today*, 100 (2005) 79–94.
25. L. Čapek, J. Adama, T. Grygar, R. Bulánek, L. Vradman, G. Košová-Kučerová, P. Čičmanec, P. Knotek, *Appl. Catal. A: Gen.*, 342 (2008) 99–106.
26. G. Lischke, W. Hanke, H.G. Jerschkewitz, G. Öhlmann, *J. Catal.*, 91 (1985) 54–63.
27. K. N. Bhagya, V. Gayathri, *J. Porous Mater.*, 21 (2014) 197–206.
28. S. Sumimoto, C. Tanaka, S. Yamaguchi, Y. Ichihashi, S. Nishiyama, S. Tsuruya, *Ind. Eng. Chem. Res.*, 45 (2006) 7444–7450.

29. D. F. Back, C. R. Kopp, G. M. Oliveira, P. C. Piquini, *Polyhedron*, 36 (2012) 21–29.
30. J. M. S. Santos, S. Carvalho, E. B. Paniago, H. A. Duarte, *J. Inorg. Biochem.*, 95 (2003) 14–24.
31. C. L. Hill, *The Use of Polyoxometalates in Reactions with Hydrogen Peroxide, Catalysis by Metal Complexes*, 9 (1992) Chapter 8.

3. Gas Phase Oxidation of Benzene with Molecular Oxygen Catalysed by Cu/HZSM-5

Chapter 3. Gas Phase Oxidation of Benzene with Molecular Oxygen Catalysed by Cu/HZSM-5

3.1. Introduction

Catalytic partial oxidation reactions of hydrocarbons have important industrial applications. The oxidation of hydrocarbons has been widely studied for the manufacture of chemical derivatives such as alcohols, aldehydes, ketones, carboxylic acids, and epoxides, which are industrially significant [1-6]. Hence, their synthesis through an economical, low-energy, and green catalytic process is attractive and has been actively studied in the field of chemistry.

Phenol is one of the most important chemicals that find application in the fields of resins, fibres, and medicine. In the current industrial process, the cumene process, the yield of phenol is only 5%. The cumene process is a high-energy method that requires a three-step reaction and distillation for the separation of the products and reactant. Therefore, the direct oxidation of benzene is an economically more desirable process for phenol production without the formation of by-products. Many researchers have investigated the selective oxidation of benzene for the one-step synthesis of phenol. In particular, Panov et al. [7,8], Yoo et al. [9], and Sachtler et al. [10] have reported the catalytic gas phase oxidation of benzene to phenol

over Fe supported catalysts with N_2O; however, N_2O is expensive for use as an oxidant. Some researchers have reported the liquid phase hydroxylation of benzene with TEMPO [11] or H2O2 [12-16]. Moreover, in terms of an environmental and economical chemistry there is a growing demand for catalytic methods that employ a clean oxidant, such as O_2, with few additives [17-22]. However, the one-step synthesis of phenol from benzene without additives is more desirable for industrial applications. I have studied the direct oxidation of benzene in the gas phase using only molecular O_2, which is an inexpensive oxidant. Cu impregnated on HZSM-5 has been found to catalyse the one-step synthesis of phenol form benzene and O_2 [23,24]. It has also been reported that the Cu/HZSM-5 catalyst with TiO_2 added (Cu/Ti/HZSM-5) improves phenol formation [25]. However, the obtained selectivity of phenol is quite low due to by-products formed by the excess oxidation of benzene and phenol to CO and CO_2. In the present paper, I attempt to improve the selectivity of phenol over Cu/Ti/HZSM-5. The effect of Ti addition is also described in detail by means of O_2 uptake measurements.

3.2. Experimental

All materials were obtained commercially. The HZSM-5 (Si/Al atomic ratio = 29) zeolite was purchased from ZEOLIST. $Cu(OAc)_2 \cdot H_2O$, $[TiO(C_2O_4)_2] \cdot nH_2O$, benzene, toluene, and 2-propanol were purchased from

Nacalai Tesque. All the chemicals were used with any further purification.

Cu impregnated on HZSM-5 (Cu/HZSM-5) catalyst was prepared by an impregnation method with HZSM-5 zeolite and $Cu(OAc)_2 \cdot H_2O$ in distilled water. The obtained solid was dried out at 393 K overnight, and then calcined under airflow at 1273 K for 5 h. The samples were designated as Cu/HZSM-5 and contained 0.70 wt% Cu.

Cu and Ti supported HZSM-5 (Cu/Ti/HZSM-5) catalysts were prepared by an impregnation method as follows. $TiO(C_2O_4)_2 \cdot nH_2O$ as the source of Ti and HZSM-5 were added to distilled water, and evaporated to druness. The obtained solid was dried out at 393 K overnight, and then calcined under airflow at 773 K for 5 h. The obtained Ti/HZSM-5 was mixed with $Cu(OAc)_2 \cdot H_2O$ in distilled water, evaporated, and then dried out at 393 K. The obtained solid was calcined under airflow at 1273 K for 5 h. The samples were composed of 0.70 wt% Cu and 0.26–0.74 wt% Ti (Ti/Cu atomic ratio = 0.5–1.4).

The direct oxidation of benzene in gas-phase was performed using a conventional continuous flow system with a fixed-bed Pyrex glass reactor (internal diameter = 18 mm) at atmospheric pressure. The catalyst was calcined at 773 K for 2 h under airflow and purged with N_2 gas for 30 min at 773 K before the reaction. The reaction conditions were as follows: W (catalyst weight) = 0.5 g; F (total flow rate) = 2.12×10^{-3} mol/min; W/F = 2.36×10^2 g-cat min/mol; reaction temperature = 673 K; benzene partial pressure = 3.75 kPa; O_2 partial pressure = 1.27–20.26 kPa; and balance gas = N_2. The reaction products were trapped at 223 K using a refrigerant

(liquid nitrogen + diethyl malonate) and dissolved with a solution of toluene and 2-propanol (1:1 v/v). The products (phenol, hydroquinone, and *p*-benzoquinone) were analysed with a high performance liquid chromatograph (Jasco, LC-2000 Plus) equipped with a C18 column using a mixed solution carrier of 0.1 vol% phosphoric acid aqueous solution and acetonitrile (1:1 v/v). The gaseous products, such as CO and CO_2, were analysed with a gas chromatograph equipped with Thermal Conductivity Detector (TCD) using stainless steel columns containing active carbon (1 m) and molecular sieves 13X (3 m) at 323 K under H_2 carrier. Yields of phenol, hydroquinone, *p*-benzoquinone, CO, or CO_2, and the selectivity of phenol were calculated using the following equation:

Yield of phenol, hydroquinone, or p-benzoquinone (%) =

$$\frac{mole\ number\ of\ [phenol,\ hydroquinone,\ or\ p-benzoquinone]}{mole\ number\ of\ benzene\ fed} \times 100$$

Yield of CO_x (%) =

$$\frac{1/6 \times mole\ number\ of\ [CO\ and\ CO_2]}{mole\ number\ of\ benzene\ fed} \times 100$$

Selectivity of phenol (%) =

$$\frac{mole\ number\ of\ phenol}{total\ mole\ number\ of\ liquid\ phase\ products\ and\ 1/6 \times [CO\ and\ CO_2]} \times 100$$

The photoluminescence spectra of Cu/HZSM-5 were recorded using a fluorescence spectrophotometer (F-7000, HITACHI) with a Xenon lamp as

the excitation light source at 73 K in vacuum. The fluorescence was generated by continuous-wave, near-UV excitation at 280 nm.

The O_2 uptake on the surface of the catalyst was measured using a constant-volume-type semi-micro gas-adsorption apparatus connected to a quartz cell in which the catalyst was charged. The catalyst was calcined under an O_2 atmosphere at 773 K for 1 h. After calcination, the catalyst was evacuated at 773 K for 1 h, and then reduced under a CO atmosphere at 773 K for 1 h. The dead volume in the cell at 673 K was measured by charging 1.3 kPa of He gas. The total uptake of O_2 was measured after O_2 adsorption equilibrium under 2.6 kPa of O_2 at 673 K. After the evacuation at 673 K for 1 h, the reversible adsorbed uptake of O_2 was measured by charging 2.6 kPa of O_2. The calculated irreversible uptake of O_2 could be defined as the amount of O_2 which selectively adsorbed on the Cu surface of catalyst [12]. The amount of Cu^+ site was estimated by the O_2 uptake measurement.

3.3. Results and Discussion

3.3.1. Catalytic test of Cu/HZSM-5

The benzene oxidation reaction was performed over Cu/HZSM-5 at 673 K under airflow (mole ratio N_2:O_2:benzene = 4:1:0.18). The time profiles of the product yields and phenol selectivity are shown in Figure 1. The yield of phenol increases over time and attains a maximum yield of 2.3%

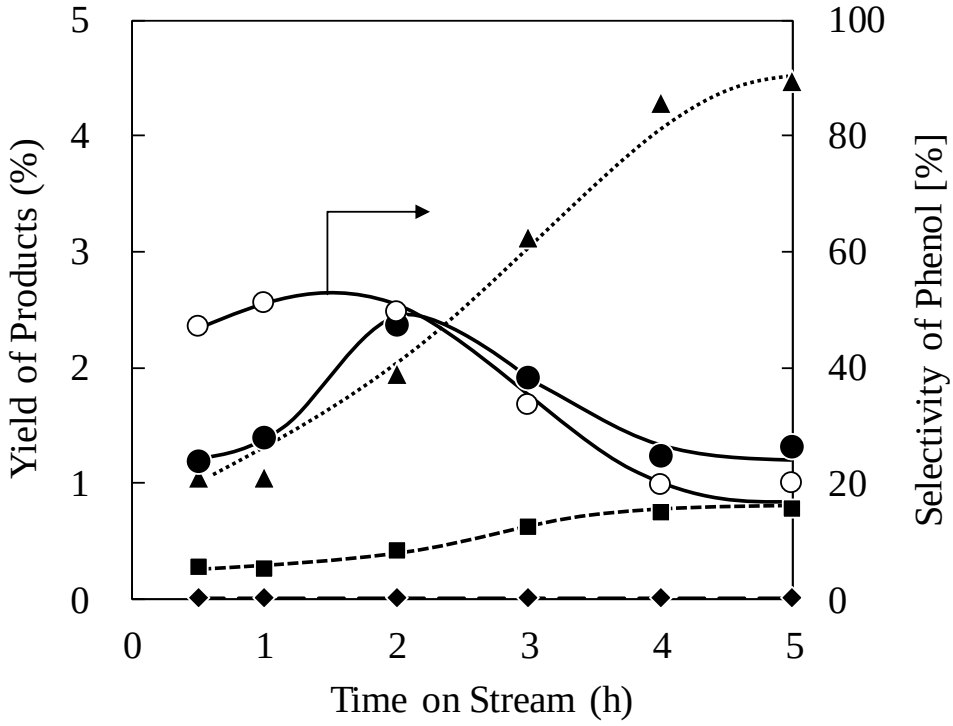

Figure 1. Time profiles of the product yields for the oxidation of benzene over the Cu/HZSM-5 catalyst.

Catalyst; Cu/HZSM-5 (Cu = 0.7 wt%, Si/Al = 29)

Total pressure; 101.32 kPa (N_2 : O_2 : Benzene = 4 : 1 : 0.18)

Yield of phenol (●), hydroquinone (◆), *p*-benzoquinone (■), and COx (▲) : Selectivity of phenol (○)

within 2 h. The selectivity of phenol is 48.0% at 2 h. When the reaction time is prolonged beyond 5 h, the yield and selectivity of phenol decrease to 1.3% and 20.0%, respectively. The selectivity of phenol is decreased by the increase in the yield of by-products, such as *p*-benzoquinone and COx ($CO + CO_2$). The yield of highly oxidized by-products increases with the reaction progress, suggesting that phenol formation may decrease over time due to the excess oxidation of benzene and phenol. To investigate the role of O_2 during benzene oxidation, after halting the supply of O_2 in the gas phase, the phenol and by-product yields were measured.

Figure 2 shows the time profile of benzene oxidation over Cu/HZSM-5 with and without O_2 supply. The reaction was carried out by supplying the gas, which includes N_2, O_2, and benzene, into the reactor for 1.5 h (term A). All product yields increase over time during term A, and phenol, which is the main product, is obtained in a 2.5% yield at a reaction time of 1.5 h. The supply of O_2 and benzene was stopped at 1.5 h, and then only N_2 was fed into the reactor for 30 min to remove the benzene, oxidation products, and gaseous O_2 (term B). At a reaction time of 2 h, neither benzene nor any of the products are detected, thus confirming their removal by purging with N_2 gas for 30 min. Benzene and N_2 gas were then supplied to the reactor for 3 h (term C). Phenol is only obtained in a yield of 0.6% with a selectivity of 99% after 2.5 h of reaction, and then the yield of phenol gradually decreased until 5 h. It is speculated that molecular O_2 in the gas phase causes the formation of by-products. It also reveals that lattice O_2 on Cu/HZSM-5 gets involved in the oxidation of benzene to phenol, which can

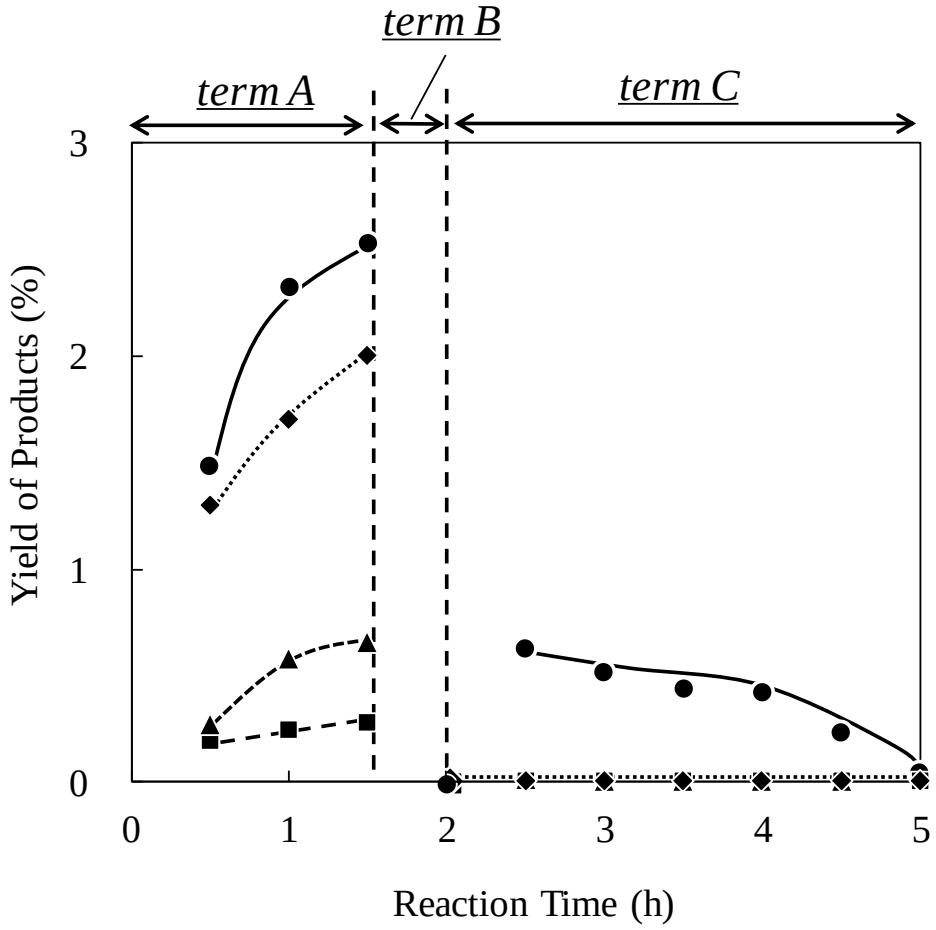

Figure 2. Time profile of benzene oxidation with or without oxygen.

Catalyst; Cu/HZSM-5 (Cu = 0.7 wt%, Si/Al = 29)

Yield of phenol (●), hydroquinone (■), *p*-benzoquinone (▲), COx (◆)

Total pressure, 101.32 kPa,

Reaction flow condition;

term A; N_2 : O_2 : Benzene = 4 : 1 : 0.18

term B; N_2 : O_2 : Benzene = 5 : 0 : 0

term C; N_2 : O_2 : Benzene = 5 : 0 : 0.18

proceed without gaseous O_2.

3.3.2. Dependence of O_2 partial pressure on the phenol formation activity

The benzene oxidation reaction over Cu/HZSM-5 catalyst was performed under various partial pressures of O_2. Hence, the influence of O_2 in the gas phase on the catalytic performance was investigated. Reactions under various mole ratios of O_2/N_2 with constant flow were carried out. As shown in Figure 3, phenol is obtained in a yield of 2.3% with a selectivity of 44% under 20.0 kPa of O_2 partial pressure. In the case of 1.3 kPa of O_2 partial pressure, phenol is obtained in a yield of 1.7% with a selectivity of 94%. The yields of benzoquinone and COx decrease drastically with decreasing O_2 pressure, while the yield of phenol remains almost constant. This result indicates that gas-phase O_2 is involved in the formation of by-products, whereas phenol is formed with high selectivity under lower O_2 partial pressure.

The reaction over Cu/HZSM-5 under lower O_2 partial pressure leads to the extremely high selectivity of phenol; however, the phenol yield with Cu/HZSM-5 remains low. Our laboratory has previously reported that Ti addition to Cu/HZSM-5 leads to a higher phenol yield [25]. The catalytic performance of Cu/Ti/HZSM-5 under various O_2 partial pressures was evaluated, and the results are shown in Figure 4. In the reaction under an O_2 partial pressure of 20 kPa, phenol is obtained in a yield of 3.3% with a

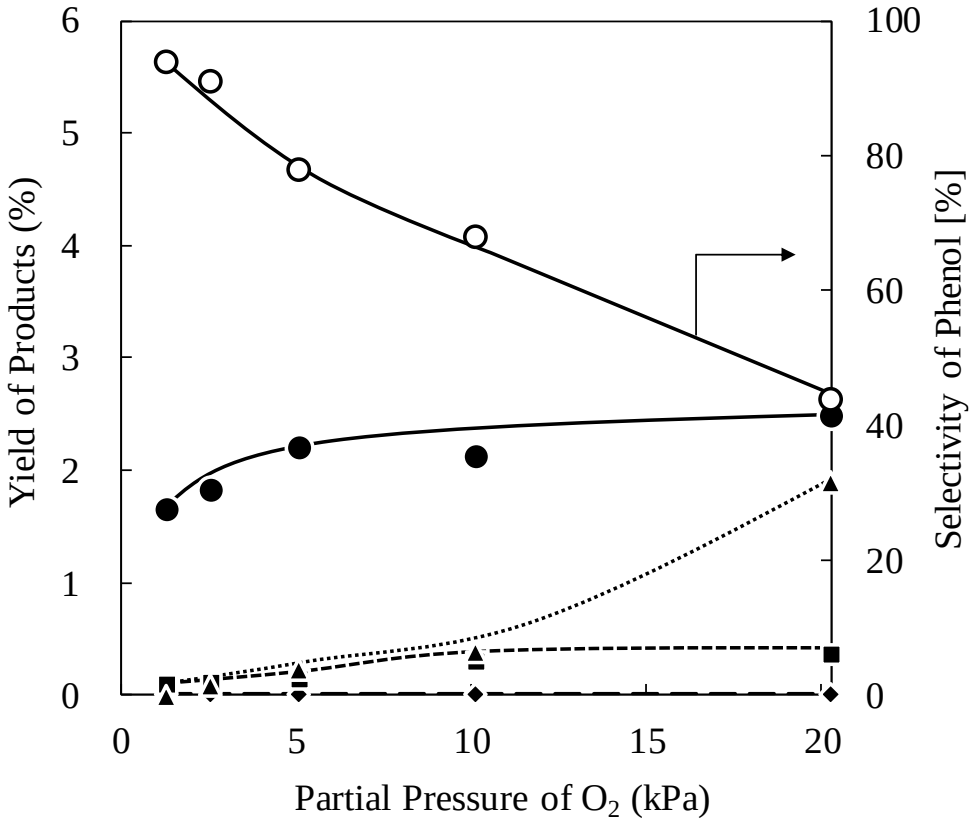

Figure 3. Dependence of the O_2 pressure for benzene oxidation over the Cu/HZSM-5 catalyst.

Catalyst; Cu/HZSM-5 (Cu = 0.7 wt%, Si/Al = 29),

Total pressure, 101.32 kPa,

Yield of phenol (●), hydroquinone (■), p-benzoquinone (▲) and COx (◆) : Selectivity of phenol (○)

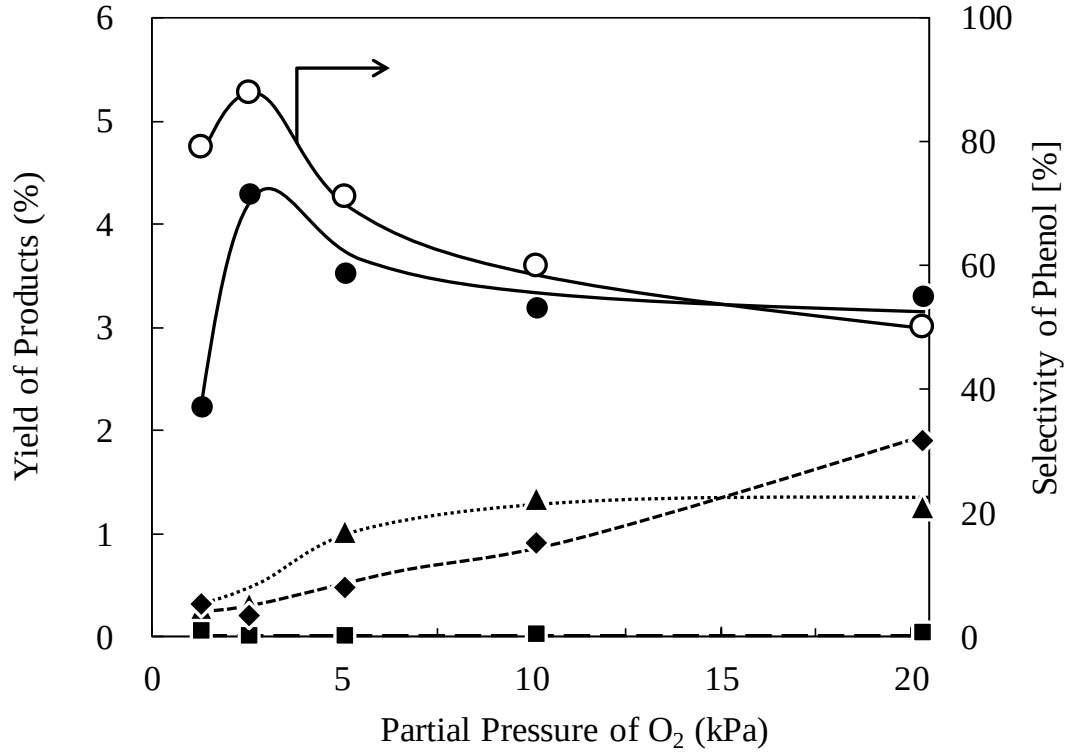

Figure 4. Dependence of the O_2 pressure for benzene oxidation over the Cu/Ti/HZSM-5 catalyst.

Catalyst; Cu/Ti/HZSM-5 (Cu = 0.7 wt%, Ti/Cu = 0.7, Si/Al = 29),

Total pressure; 101.32 kPa,

Yield of phenol (●), hydroquinone (■), p-benzoquinone (▲) and COx (◆) , Selectivity of phenol (○)

selectivity of 50.0%. On the other hand, phenol is obtained in a yield of 4.3% with the highest selectivity of 88.0% under an O_2 partial pressure of 2.5 kPa. The phenol selectivity increases with decreasing O_2 partial pressure, and the phenol yield increases remarkably over Cu/Ti/HZSM-5. I found that Cu/Ti/HZSM-5 represents high activity for the selective oxidation of benzene under lower partial pressure of O_2.

3.3.3. Effect of Ti addition to Cu/HZSM-5

It has previously been reported that the oxidation products are formed through the redox cycle between Cu^+ and Cu^{2+} [24]. I investigated the relationship between the oxidative state of Cu and phenol formation by characterising the oxidative state of Cu in Cu/HZSM-5 during the reaction using photoluminescence spectroscopy (see Figure 5). The photoluminescence band assigned to Cu^+ is hardly observed in the spectra of Cu/HZSM-5 before the reaction and after 0.5 h of reaction. This result indicates that most of the Cu before the reaction is in the oxidation state of +2. The peak appears around 450 nm after 1.5 h of reaction, and increases further after 3.0 h of reaction. Previous studies have reported that the absorption band at around 280–300 nm and the photoluminescence band at around 400–500 nm are attributed to the electronic excitation of the Cu^+ ion and its reverse radiative deactivation, respectively [25, 26]. It is clear that most of the Cu^{2+} species are reduced to Cu^+ species during the reaction, and phenol production proceeds through the redox cycle of Cu.

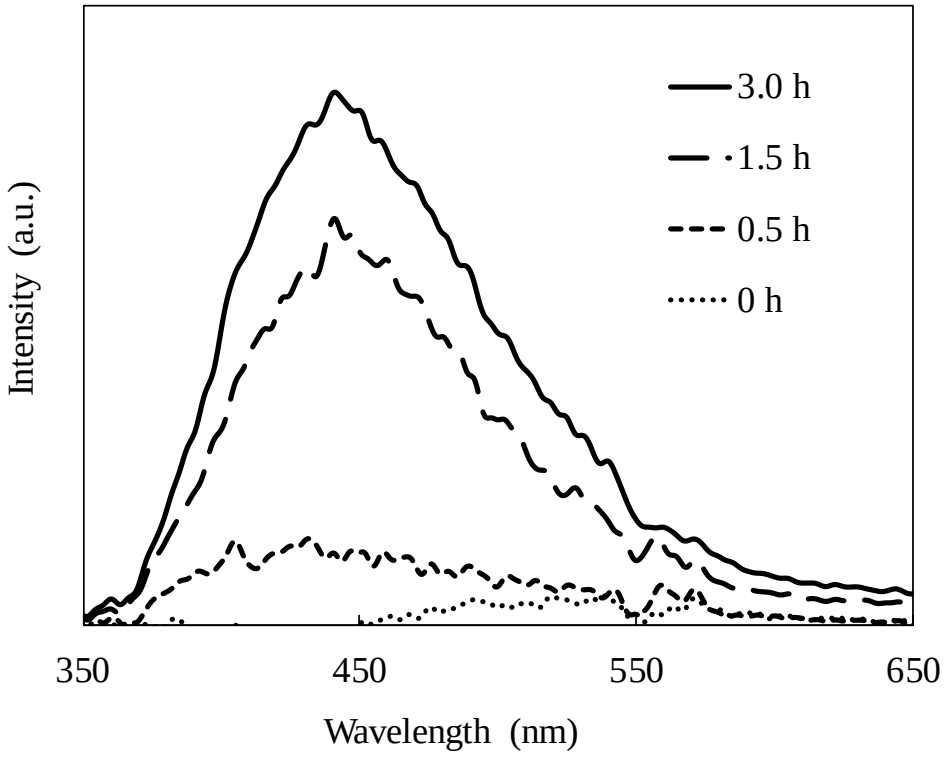

Figure 5. Photoluminescence spectra of Cu/HZSM-5 during the oxidation reaction benzene with molecular oxygen. The fluorescence was generated by continuous-wave, near-UV excitation at 280 nm from a Xenon lamp.

The amount of Cu^+ sites can be estimated by measuring the O_2 uptake of the catalysts [27]. The amount of O_2 uptake of Cu/Ti/HZSM-5 with different Ti/Cu mole ratios was measured. The O_2 uptake of the sample was measured as follows: Cu/Ti/HZSM-5 samples were heated at 773 K for 1 h in the presence of CO in order to reduce Cu species from Cu^{2+} to Cu^+. These reduced samples were then exposed to O_2 gas (2.6 kPa) at 673 K, which selectively adsorbs to Cu^+ sites. The amount of O_2 adsorbed on Cu^+ sites was measured after adsorption equilibrium was attained. The relationship between O_2 uptake and the Ti/Cu atomic ratio of the catalysts is shown in Figure 6. The yield of phenol and O_2 uptake of the catalysts having different Ti/Cu atomic ratios are represented by black circles and white squares, respectively. Titania addition leads to an increase in catalytic activity, and Cu/Ti/HZSM-5 having 0.7 of Ti/Cu atomic ratio shows the maximum yield of phenol (4.3%). The O_2 uptake also increases with increasing Ti addition, and Cu/Ti/HZSM-5 (Ti/Cu = 0.7) shows the maximum amount of O_2 uptake (2.5 μmol/g-cat). This indicates that the amount of Cu^+ sites is closely related to the catalytic activity of phenol formation. It is found that the selective formation reaction of phenol efficiently proceeds through the formation of Cu^+ sites, which increases by Ti addition, even under the lower partial pressure of O_2. The increase of Cu^+ sites by Ti addition is caused by either a dispersion of Cu particles or a change of the electronic state of Cu. The decrease of phenol yield and O_2 uptake over Cu/Ti/HZSM-5 having Ti/Cu atomic ratios greater than 0.7, may occur because the Cu surface is covered by Ti. Thus, the Cu^+ species of the

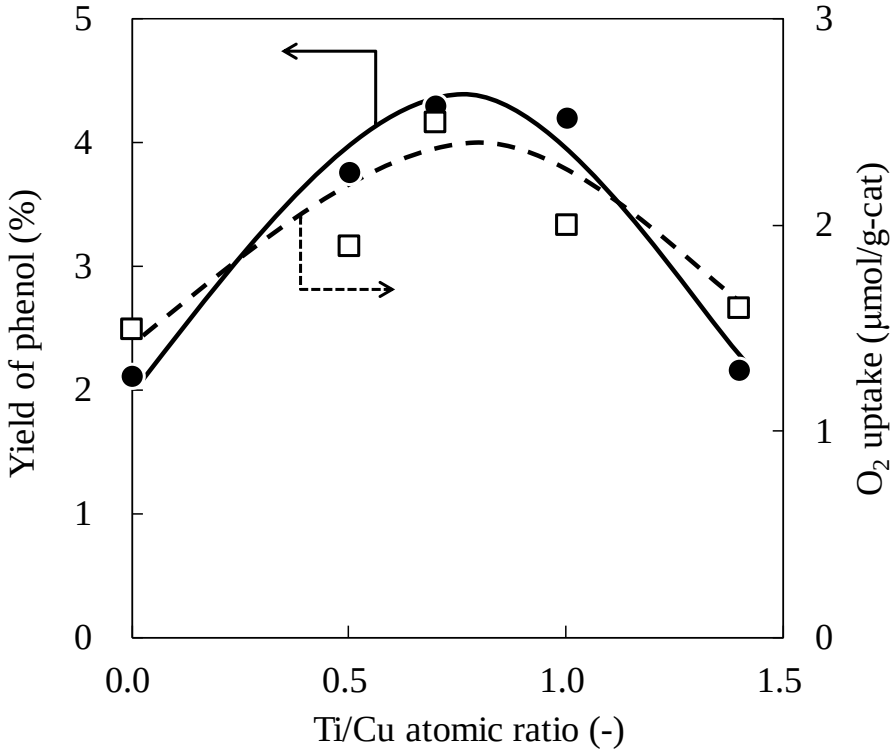

Figure 6. Effect of Ti content ratio in Cu/Ti/HZSM-5 on O_2 uptake and phenol yield.

Catalyst; Cu/Ti/HZSM-5 (Cu = 0.7 wt%, Ti/Cu = 0 - 1.4, Si/Al = 29)

Total pressure; 101.32 kPa (N_2 : O_2 : Benzene = 20 : 1 : 0.18)

O_2 uptake (□), Yield of phenol (●)

catalyst surface plays a significant role in the phenol formation. Cu/Ti/HZSM-5 catalysts achieve extremely high yield and selectivity of phenol for the direct oxidation of benzene under a lower O_2 partial pressure because of the increase in the number of Cu^+ sites and the prevention of by-products.

3.4. Conclusion

The catalytic direct oxidation of benzene was carried out using Cu/HZSM-5 with Ti and molecular O_2 in the gas phase for one-step synthesis of phenol. The result of benzene oxidation in the presence or absence of O_2 in the flow reveals that the lattice O_2 spec for ies of the catalyst is involved in phenol formation and the excess O_2 in the gas-phase is involved in by-product formation. The decrease of O_2 partial pressure prevented formation of the by-products, and thus improved the phenol selectivity considerably. Addition of Ti to Cu/HZSM-5 improved the phenol yield, and led to the increase of Cu^+ sites, which was closely related to the phenol formation activity of Cu/Ti/HZSM-5. The Cu and Ti supported HZSM-5 catalyst (Ti/Cu atomic ratio = 0.7) exhibited high yield (4.3%) and high selectivity (88.0%) for the direct oxidation of benzene to phenol under lower O_2 partial pressure. The investigation of the Cu/Ti/HZSM-5 catalyst under lower O_2 partial pressure suggests that this catalyst could effectively produce phenol from benzene in a one-step synthesis procedure.

References

1. R. H. Crabtree, *J. Chem. Soc., Dalton Trans.*, (2001) 2437–2450.
2. A. Corma, P. Esteve, A. Martínez, *J. Catal.*, 161 (1996) 11–19.
3. C. Parmeggiani, F. Cardona, *Green Chem.*, 14 (2012) 547–564.
4. J. U. Ahmad, M. T. Räisänen, M. Leskelä, T. Repo, *Appl. Catal A: Gen.*, 180 (2012) 411–412.
5. I. Fernandez, N. Khiar, *Chem. Rev.*, 103 9 (2003) 3651–3706.
6. Y. Ichihashi, Y. Kamizaki, N. Terai, K. Taniya, S. Tsuruya, S. Nishiyama, *Catal. Lett.*, 134 (2010) 324–329.
7. G. I. Panov, G. A. Sheveleva, A. S. Kharitonov, V. N. Romannikov, *Appl. Catal. A: Gen.*, 82 (1992) 31–36.
8. V. S. Chernyavsky, L. V. Pirutko, A. K. Uriarte, A. S. Kharitonov, G. I. Panov, *J. Catal.*, 245 2 (2007) 466–469.
9. J. S. Yoo, A.R. Sohail, S.S. Grimmer, J.Z. Shyu, *Appl. Catal. A: Gen.*, 117 (1994) 1–16.
10. J. Jia, K. S. Pillai, W. M. H. Sachtler, *J. Catal.*, 221 (2004) 119–126.
11. H. Yanga, J. Chena, J. Li, Y. Lv, S. Gao, *Appl. Catal. A: Gen.*, 415–416 16 (2012) 22–28.
12. S. Sumimoto, C. Tanaka, S. Yamaguchi, Y. Ichihashi, S. Nishiyama, S. Tsuruya, *Ind. Eng. Chem. Res.*, 45 (2006) 7444–7450.
13. K. Nomiya, H. Yanagibayashi, C. Nozaki, K. Kondoh, E. Hiramatsu, Y. Shimizu, *J. Mol. Catal. A: Chem.*, 114 1–3 (1996) 181–190.
14. M. Stöckmann, F. Konietzni, J. U. Notheis, J. Voss, W. Keune, W. F

Maier, *Appl. Catal. A: Gen.*, 208 1–2 (2001) 343–358.

15. K. M. Parida, D. Rath, *Appl. Catal. A: Gen.*, 321 2 (2007) 101–108.
16. Y. Liu, K. Murata, M. Inaba, *Catal. Commun.*, 6 10 (2005) 679–683.
17. T. D. Bui, A. Kimura, S. Ikeda, M. Matsumura, *J. Am. Chem. Soc.*, 132 24 (2010) 8453–8458.
18. Y. Seo, Y. Mukai, T. Tagawa, S. Goto, *J. Mol. Catal. A: Chem.*, 120 1–3 (1997) 149–154.
19. T. Miyake, M. Hamada, H. Niwa, M. Nishizuka, M. Oguri, *J. Mol. Catal. A: Chem.*, 178 1–2 (2002) 199–204.
20. K. Takata, S. Yamaguchi, S. Nishiyama, S. Tsuruya, *J. Mol. Catal. A: Chem.*, 225 (2005) 125–130.
21. T. Miyahara, H. Kanzaki, R. Hamada, S. Kuroiwa, S. Nishiyama, S. Tsuruya, *J. Mol. Catal. A: Chem.*, 176 (2001) 141–150.
22. A. Okemoto, Y. Inoue, K. Ikeda, C. Tanaka, K. Taniya, Y. Ichihashi, S. Nishiyama, *Chem. Lett.*, 43 (2014) 1734–1736.
23. H. Yamanaka, R. Hamada, H. Nibuta, S. Nishiyama, S. Tsuruya, *J. Mol. Catal. A: Chem.*, 178 (2002) 89–95.
24. R. Hamada, Y. Shibata, S. Nishiyama, S. Tsuruya, *Phys. Chem. Chem. Phys.*, 5 (2003) 956–965.
25. G. Spoto, A. Zecchina, S. Bordiga, G. Ricchiardi, G. Marta, G. Leofanti, G. Petrini, *Appl. Catal. B: Environ.*, 3 (1994) 151–172.
26. H. Yamashita, M. Matsuoka, K. Tsuji, Y. Shioya, M. Anpo, *J. Phys. Chem.*, 100 (1996) 397–402.
27. Y. Shibata, R. Hamada, T. Ueda, Y. Ichihashi, S. Nishiyama, S. Tsuruya,

Ind. Eng. Chem. Res., 44 (2005) 8765–8772.

4. Reaction Mechanism and Catalyst Design of Organic and Inorganic Semiconductors for Photocatalysis

Chapter 4.1. Visible-Light-Responsible Tungsten Oxide for Photo-oxidation of Cyclohexane

4.1.1. Introduction

Selective oxidation of hydrocarbons is an important process in the field of petroleum industrial chemistry. The partial oxidation of hydrocarbons has been widely studied for the manufacture of alcohols, aldehydes, ketones, carboxylic acids, and epoxides, which are important chemical intermediates [1-6]. The selective oxidation of cyclohexane is of great interest because the products, cyclohexanone and cyclohexanol, are intermediate compounds for synthetic fibers and fine chemicals [7-10]. The process is performed by using cobalt or manganese salts as homogeneous catalysts under harsh conditions [11-14]. This process requires high energy, and undesirable byproducts are generated through the reaction, which complicate the recovery/separation steps. The development of an environment friendly method for the selective oxidation of cyclohexane has been sought in achievement of the green chemistry. Photocatalytic reactions proceed by solar energy which is a renewable energy. Photocatalytic processes can be operated under mild conditions, such as room temperature and ambient pressure. Inorganic semiconductors, such as titanium oxide, vanadium oxide, and niobium oxide have been used for various photocatalytic reactions [15-19]. Titanium oxide (TiO_2) is a very

efficient photocatalyst for the photodegradation of organic substrates and hydrogen production [20-27]. The main drawback of TiO_2 photocatalyst is an UV absorber due to its large band gap (3.2 eV) located in the UV region of solar radiation, which is only 4% of the incoming solar energy [28, 29]. Therefore, the use of visible-light-sensitive photocatalysts is an active research field.

Tungsten oxide (WO_3) semiconductor has a band gap energy of 2.8 eV which is corresponding to the light of 460 nm in the visible region [30-32]. WO_3 is expected as the photocatalyst for selective oxidation of hydrocarbons due to its chemical stability, non-toxicity, and moderate oxidizing power [33]. Some researchers reported the photo-oxidation of hydrocarbons such as methane, and 2-propanol over WO_3 [34, 35]. In these studies, high selectivity for partial oxidation products was achieved over WO_3 photocatalysts. The main drawback of WO_3 is its low activity, thus it is required to develop WO_3 photocatalysts with high activity. It is also important to understand the reaction mechanism for developing high activity catalysts.

In previous study, WO_3 photocatalysts were employed for cyclohexane photo-oxidation using molecular oxygen under visible light irradiation [36, 37]. The catalysts successfully promote partial oxidation and Pt loading on WO_3 led to higher activity than pure WO_3. I have studied the cyclohexane photo-oxidation over WO_3 and TiO_2 binary oxide catalysts. It was found that the physical mixing of TiO_2 with WO_3 led to the higher photocatalytic activity for cyclohexane photo-oxidation under visible light

irradiation [38]. However, the physical mixing effect of TiO_2 has not been demonstrated. In this work, the photocatalytic oxidation of cyclohexane was performed over WO_3 photocatalysts and WO_3 mixed with TiO_2 photocatalysts. The effect of TiO_2 in the cyclohexane photo-oxidation was investigated. The reaction mechanism of cyclohexane photo-oxidation over WO_3 photocatalysts were also investigated by ESR measurement and isotope labeling studies using $^{18}O_2$ and cyclohexane-d_{12}.

4.1.2. Experimental

4.1.2.1. Catalyst preparation

WO_3 was obtained from [Nacalai Tesque (extra-pure reagent)] and calcined at 673 K for 3h in air flow. TiO_2 was supplied by the Catalysis Society of Japan as a standard reference catalyst (JRC-TIO-2-7, 9, 11) and calcined at 673 K for 3 h in air flow.

Pt/WO_3 was prepared by photodeposition method. WO_3 powder (1 g) was dispersed into aqueous solution of H_2PtCl_6 (13 mg; Tanaka Kikinzoku Kogyo K K.) and ethanol (25 mL; Nacalai Tesque) under UV light (λ>260 nm) irradiation for 2 h. The resulting mixture was filtered, washed with ion exchanged water, and then dried at 373 K overnight. The obtained solid was designated Pt/WO_3 (the amount of Pt loading was 0.5 wt%). The amount of Pt loading was calculated by (Pt (g)/WO_3 (g))$\times$100.

4.1.2.2. Characterisation

BET surface area was measured by nitrogen physisorption (BELSORP). Catalyst (50mg) was pretreated 473 K in N_2 flow (50 mL/min) for 2 h. Measurement was carried out at 77 K

Electron spin resonance (ESR) measurements were done with a TE-260 at room temperature and calibrated with a MnO standard. For the N-tert-Butyl-α-phenylnitrone (PBN) spin-trapping ESR experiments, catalyst and PBN were suspended in cyclohexane and magnetically stirred at room temperature under visible light irradiation for 3 min. The supernatant was poured into an ESR cell, and then ESR spectrum was recorded at room temperature.

4.1.2.3. Cyclohexane photo-oxidation

Physical mixing $Pt/WO_3 + TiO_2$ catalysts with different TiO_2 contents were prepared by physical mixing method. These catalysts were described Pt/WO_3-TIO-*X*(Y) [Y=0~100 wt%]. The wt% of TiO_2 was calculated by TiO_2 (g)/($Pt/WO_3 + TiO_2$ (g)) × 100. The liquid-phase photo-oxidation of cyclohexane under visible light irradiation was carried out using a quartz batch reactor of 30 mL. Catalyst (50 mg) and cyclohexane (10 mL; Nacalai Tesque) were added to the reactor. The reactor bubbled with Ar or O_2 gas flow (100 mL/min) for 15 min. The reaction solution was magnetically stirred under irradiation with a 500W Xenon lamp (Usio SX-UI501XQ)

through a color filter (λ>420 nm) for 1 h at room temperature. The liquid-phase products were analyzed by gas chromatograph (Shimazu GC-18A) equipped with FID. The gas-phase products were analyzed by gas chromatograph (Shimazu GC-8A) equipped with TCD.

The gas-phase photo-oxidation of cyclohexane under visible light irradiation was carried out by using a quartz batch reactor equipped with a gas line. A quartz cell contains catalyst (0.5 g) was connected the reactor and evacuated in vacuum for 10 min. Cyclohexane or cyclohexane-d_{12} (5.0 kPa) was supplied to the reactor. Reactant in gas phase was trapped at 77 K for 10 min. Then, oxygen-$^{18}O_2$ (1.0 kPa) was introduced to the reactor. The trapped reactant was vaporized at room temperature. The reactor was irradiated with a 500 W Xenon lamp through a color filter (λ>420 nm). After the reaction, products were analyzed by the mass spectroscopy (QME220).

4.1.3. Results and discussion

4.1.3.1. Photo-oxidation reaction mechanism of cyclohexane over WO_3 photocatalyst

Table 1 shows the product yields for cyclohexane photo-oxidation under visible light irradiation (λ>420 nm) over WO_3, Pt/WO_3 and TiO_2 with molecule oxygen. No photocatalytic activity is observed over TiO_2. The yields of cyclohexanone and cyclohexanol over WO_3 with oxygen are 31.3

Table 1. Photo-oxidation of cyclohexane over WO_3, Pt/WO_3 and TiO_2 under visible light irradiation (λ>420 nm)[a].

Catalyst	Atmosphere	Yield of products (μmol/g-cat)			
		Cyclohexanone	Cyclohexanol	1/6 CO_2	Total
WO_3	O_2	31.3	23.3	1.2	55.8
Pt/WO_3[b]	O_2	96.9	53.9	3.6	154.4
TiO_2	O_2	0	0	0	0
Pt/WO_3[b]	Ar	22.9	2.9	1.2	27.0

a: Reaction conditions: cyclohexane (10 mL), catalyst (50 mg), irradiate time (1 h), O_2 or A r(1 atm)

b: Pt loading was 0.5 wt%

μmol/g-cat and 23.3 μmol/g-cat, respectively. Pt loading on the WO_3 leads to higher photocatalytic activity than that of pure WO_3. It is suggested that Pt on the WO_3 works as an electron acceptor and enhances charge separation [39]. These results indicate that WO_3 effectively works as a photocatalyst for cyclohexane photo-oxidation under visible light irradiation. On the other hand, cyclohexanone and cyclohexanol are produced over Pt/WO_3 without oxygen. The yields of cyclohexanone and cyclohexanol over Pt/WO_3 under Ar atmosphere are 22.9 μmol/g-cat and 2.9 μmol/g-cat, respectively. Similar results are obtained with different Ar purging time ranging from 15 to 60 min. It is seems that dissolved oxygen is removed by Ar purge for 15 min, thus this photo reaction is not influenced by dissolved oxygen. It is found that cyclohexanone and cyclohexanol are produced without molecular oxygen although the product yields decrease. Then it is not clear that how molecular oxygen works in this reaction. To investigate the role of molecular oxygen during the photo reaction, photocatalytic oxidation of cyclohexane over Pt/WO_3 is performed with oxygen-$^{18}O_2$ instead of $^{16}O_2$. The yield of cyclohexanone isotopes produced during the reaction was analyzed by mass spectroscopy. Figure 1 shows the time profiles of cyclohexanone isotope yields for the cyclohexane photo-oxidation with $^{18}O_2$ over Pt/WO_3. Cyclohexanone including ^{18}O is not observed until 6 h. On the other hand, cyclohexanone including ^{16}O is observed in the initial period of the reaction until 6 h. In this reaction, ^{16}O atom exists only in lattice of WO_3. Hence, it is suggested that cyclohexanone is produced through the reaction with lattice oxygen in WO_3.

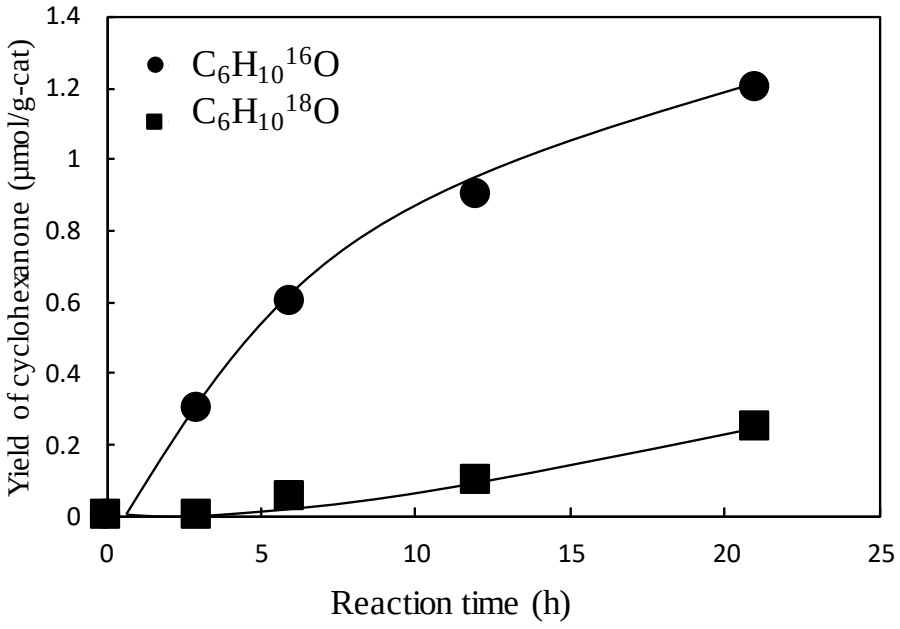

Figure 1. Time profile for yield of cyclohexanone isotopes formed during photo-oxidation of cyclohexane over Pt/WO_3 with $^{18}O_2$. Reaction conditions: catalyst (0.5 g), cyclohexane (5.0 kPa), O_2 (1.0 kPa).

Cyclohexanone including ^{18}O is observed in the later period from 6 h to 21 h. These results are explained by the following process. In the initial period of the reaction, cyclohexanone including ^{16}O forms through the reaction with ^{16}O in the lattice of WO_3. Then molecule oxygen ($^{18}O_2$) is supplied as a lattice oxygen in WO_3. In the later period of reaction, cyclohexanone including ^{18}O forms through the reaction with ^{18}O incorporated as lattice oxygen in WO_3. Hence, cyclohexanone seems to be produced through the reaction with lattice oxygen in WO_3. The formation of cyclohexanone under Ar atmosphere supports this idea.

H_2O was also detected as a by-product during the formation of cyclohexanone. However, the mechanism of H_2O formation has not yet been obvious during cyclohexane photo-oxidation. Then photocatalytic oxidation of cyclohexane-d_{12} over Pt/WO_3 was performed by using $^{18}O_2$. The isotopes distribution of H_2O was analyzed by mass spectroscopy. The results are shown in Fig. 2. $H_2{}^{18}O$ and $HD^{16}O$ are observed until 3 h. Yield of these isotopes increases with the reaction time until 9 h. H atom in $H_2{}^{18}O$ seems to be derived from the OH group of catalytic surface since cyclohexane-d_{12} has no H atom. It is suggested that $H_2{}^{18}O$ forms through the reaction of molecular oxygen ($^{18}O_2$) with OH group of catalytic surface in multi-electron reduction of molecular oxygen ($^{18}O_2$) [39]. $HD^{16}O$ probably forms through the reaction of D_{12}-cyclohexane with OH group of catalytic surface [34]. It is speculated that H atom of cyclohexane is interacted with OH group of catalytic surface and cyclohexyl radicals are produced as intermediate during the reaction.

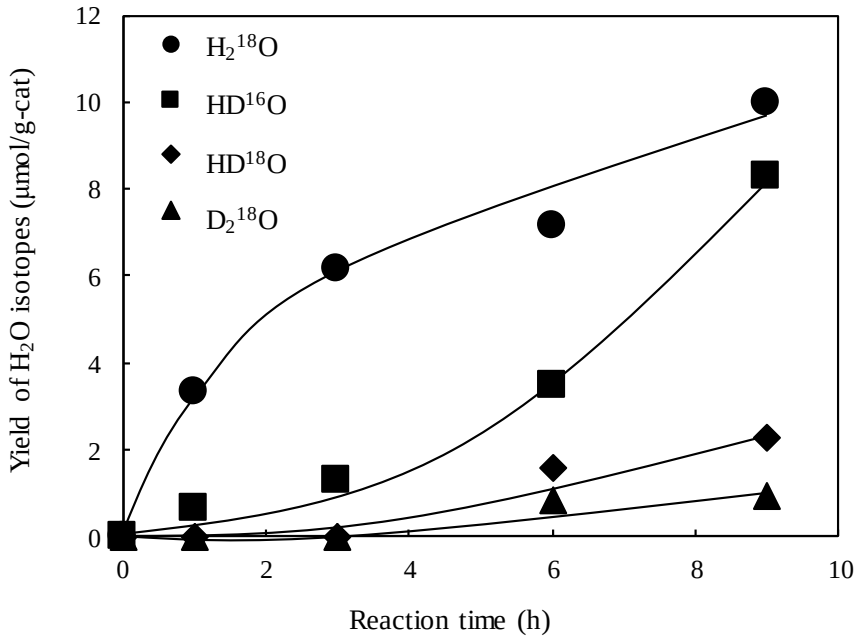

Figure 2. Time profile for yield of H_2O isotopes formed during photo-oxidation of D_{12}-cyclohexane over Pt/WO_3 with $^{18}O_2$.

Reaction conditions: catalyst (0.5 g), cyclohexane (5.0 kPa), O_2 (1.0 kPa).

The spin trapping technique using PBN is employed to detect the radical intermediates formed during reactions [40]. Hence, the radical intermediate of this reaction was observed by ESR measurement using PBN as a spin trap agent. Figure 3 shows the ESR spectra of the mixture of PBN and Pt/WO_3 in cyclohexane. A signal at g = 2.005 observed in Fig. 3 (a) is assigned to PBN [40]. A slight signal at g = 2.009 observed in Fig. 3 (b) is assigned to the PBN-cyclohexyl radical adducts [40]. A significant signal of PBN-cyclohexyl radical adducts is observed in spectrum Fig. 3 (c). These results indicate that the cyclohexyl radical is formed under visible light irradiation with Pt/WO_3.

The addition of PBN to reaction suspension influenced product yields (see Figure S1). The product yields of cyclohexanone and cyclohexanol are 96.9 μmol/g-cat and 53.9 μmol/g-cat, respectively over Pt/WO_3. In the presence of PBN, the product yields of cyclohexanone and cyclohexanol were 4.8 μmol/g-cat and 23.2 μmol/g-cat, respectively. The addition of PBN to cyclohexane led to significant decrease of product yields. It is suggested that cyclohexyl radical is the reaction intermediate of this photo reaction.

4.1.3.2. Photo-oxidation reaction of cyclohexane over Pt/WO_3 mixed with TiO_2

It has been reported that the physical mixing of TiO_2 (P25) and WO_3 leads to higher photocatalytic activity than that of WO_3 for the cyclohexane

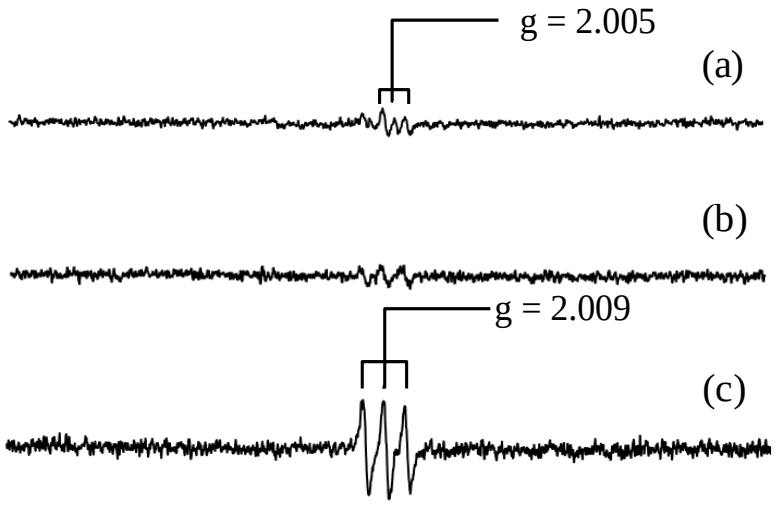

Figure 3. ESR spectra for PBN spin adducts signal obtained by (a) cyclohexane + PBN, (b) cyclohexane + PBN + Pt/WO_3 and (c)cyclohexane + PBN + Pt/WO_3 with light irradiation.

photo-oxidation [38]. However, the effect of TiO_2 mixing with WO_3 has not been clear. Then cyclohexane photo-oxidation over Pt/WO_3 mixed with various TiO_2 was performed to investigate the influence of TiO_2 on photocatalytic activity. TiO_2 was obtained from Catalysis Society of Japan and calcined at 673 K for 3 h in air flow (described as TIO-*X* (*X*=3, 4, 6, 7)). Table 2 shows the product yields for cyclohexane photo-oxidation under visible light irradiation (λ>420 nm) over Pt/WO_3-TIO-*X*. The physical mixing of TIO-*X* with Pt/WO_3 leads to higher photocatalytic activity than that of Pt/WO_3. The highest yield is obtained over Pt/WO_3-TIO-*7* (421.7 μmol/g-cat of cyclohexanone and 145.5 μmol/g-cat of cyclohexanol). The photocatalytic activities of Pt/WO_3-TIO-*X* seem to increase with an increase of BET surface area of TiO_2. Figure 4 shows the relationship between yield of products over several catalysts and the BET surface area of TiO_2. The product yields over these catalysts are shown in Table 3. The yield of cyclohexanone and cyclohexanol are proportional to BET surface area of TiO_2. It is found that product yields are just influenced by the BET surface area of TiO_2.

An ESR measurement was performed to investigate the influence of TiO_2 mixing with Pt/WO_3 on the generation of a cyclohexyl radical. Figure 5 shows the ESR spectra of cyclohexane solution including PBN with Pt/WO_3-TIO-*7*. Figure 5 (a) shows no significant signal. Figure 5 (b), which is the spectrum of cyclohexane solution including PBN with Pt/WO_3 irradiated with visible light, shows signal at g = 2.009 assigned to the PBN-cyclohexyl radical adducts [40]. Figure 5 (c), which is the spectrum of

Table 2 Photo-oxidation of cyclohexane over Pt/WO_3-TIO-X under visible light irradiation (λ>420 nm)[a].

Catalyst	Crystal phase of TIO-X		BET surface area of TIO-X (m^2/g)	Yield of products (μmol/g-cat)			
	Anatase	Rutile		Cyclohexanone	Cyclohexanol	1/6 CO_2	Total
Pt/WO_3 [b]	-	-	-	96.9	53.9	3.6	154.4
Pt/WO_3-TIO-3	0	100	46	220.4	82.5	2.0	302.9
Pt/WO_3-TIO-4	71	29	48	215.6	82.9	0.9	298.5
Pt/WO_3-TIO-6	100	0	58	289.9	109.6	1.3	400.8
Pt/WO_3-TIO-7	100	0	108	421.7	145.5	2.2	562.7

a: Reaction conditions: cyclohexane (10 mL), catalyst (50 mg), irradiate time (1 h), O_2 (1 atm) *b:* Pt loading was 0.5 wt%.

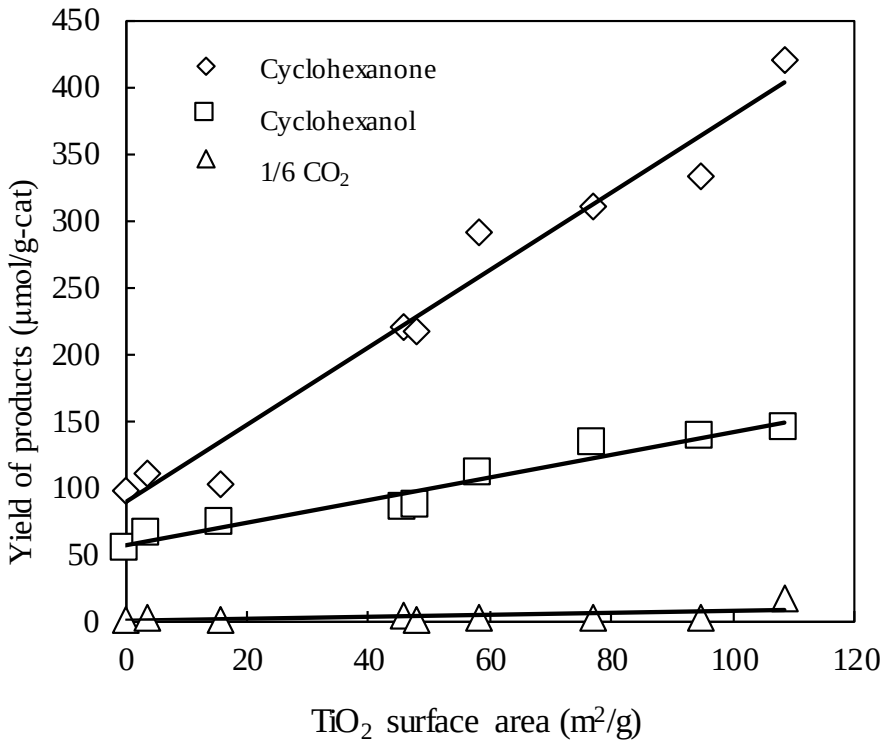

Figure 4. Effect of the surface area of TiO_2 mixed with Pt/WO_3 on the product yields of the photo-oxidation of cyclohexane under visible light irradiation (λ>420 nm).

Table 3. Photooxidation of cyclohexane over Pt/WO_3-TIO-X under visible light irradiation (λ>420 nm)[a].

Catalyst	Crystal phase		BET suface area of TIO-X (m^2/g)	Yield of products (μmol/g-cat)			
	Anatase	Rutile		Cyclohexanone	Cyclohexanol	1/6 CO_2	Total
Pt/WO_3[b]	-	-	-	96.9	53.9	3.6	154.4
Pt/WO_3-TIO-2	100	0	16	102.1	71.2	1.0	173.4
Pt/WO_3-TIO-3	0	100	46	220.4	82.5	2.0	302.9
Pt/WO_3-TIO-4	71	29	48	215.6	82.9	0.9	298.5
Pt/WO_3-TIO-5	8	92	4	107.4	63.4	1.3	172.2
Pt/WO_3-TIO-6	100	0	58	289.9	109.6	1.3	400.8
Pt/WO_3-TIO-7	100	0	108	421.7	145.5	2.2	562.7
Pt/WO_3-TIO-9	100	0	95	333.3	136.3	1.3	470.9
Pt/WO_3-TIO-11	91	9	77	310.9	131.0	0	441.9

a :Reaction conditions: cyclohexane (10 mL), catalyst (50 mg), irradiate time (1 h), O_2 (1 atm)

b: Pt loading was 0.5 wt%

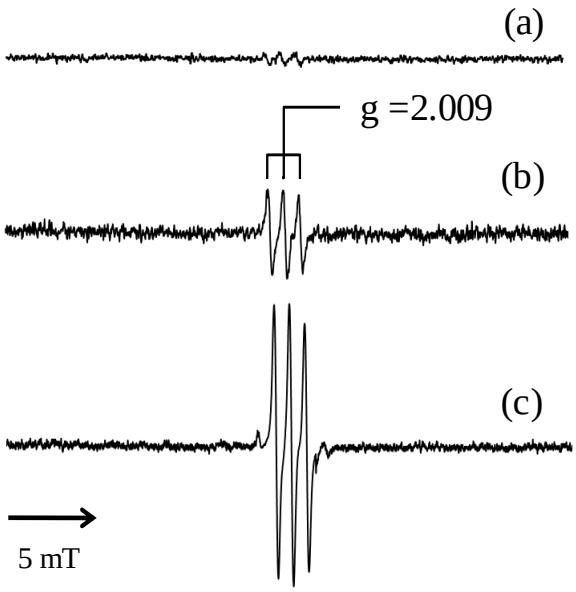

Figure 5. ESR spectra of the PBN spin adducts for (a) cyclohexane + PBN + Pt/WO_3 –TIO-7, (b) cyclohexane + PBN + Pt/WO_3 with light irradiation, and (c) cyclohexane + PBN + Pt/WO_3 –TIO-7 with light irradiation.

cyclohexane solution including PBN with Pt/WO_3-TIO-*7* irradiated with visible light, shows stronger signal at g=2.009 than that of spectrum Fig. 5 (b). It is found that the formation of cyclohexyl radical is promoted by TiO_2 mixing with Pt/WO_3. According to the result obtained from Fig. 4, it is speculated that surface of TiO_2 contributes to the cyclohexane photooxidation reaction. Hence, it seems that surface of TiO_2 contributes to the formation of cyclohexyl radical or stabilization of cyclohexyl radical.

4.1.4. Conclusion

The cyclohexane photo-oxidation proceeded under visible light irradiation over WO_3 photocatalysts, and cyclohexanone and cyclohexanol were obtained with high selectivity. The results of cyclohexane photo-oxidation with $^{18}O_2$ indicate that the lattice oxygen of WO_3 is involved in products formation. It is found from ESR measurement and the reaction in the presence of PBN that cyclohexyl radical is generated as a reaction intermediate. Pt/WO_3-TIO-*X* catalyst exhibited higher photocatalytic activity than that of Pt/WO_3 for the photocatalytic oxidation of cyclohexane. The physical mixing of TiO_2 improves products yield due to the increase in formation amount of cyclohexyl radical. The investigation of the WO_3 and TiO_2 binary catalyst which is prepared by physical mixing method suggests that this catalyst improves photocatalytic activity for the cyclohexane photo-oxidation under visible light irradiation.

References

1. R. H. Crabtree, *J. Chem. Soc. Dalton Trans.*, (2001) 2437–2450.
2. A. Corma, P. Esteve, A. Martinez, *J. Catal.*, 161 (1996) 11–19.
3. C. Parmeggiani, F. Cardona, *Green Chem.*, 14 (2012) 547–564.
4. J. U. Ahmad, M. T. Raisanen, M. Leskela, T. Repo, *Appl. Catal. A: Gen.*, 180 (2012) 411–412.
5. I. Fernandez, N. Khiar, *Chem. Rev.*, 103 9 (2003) 3651–3706.
6. P. A. A. Ignacio-de Leon, C. A. Contreras, N. E. Thornburg, A. B. Thompson, J. M. Notestein, *Appl. Catal. A: Gen.*, 511 (2016) 78–86.
7. J. M. Thomas, R. Raja, G. Sankar, G. G. Bell, *Nature*, 398 (1999) 227–230.
8. U. Schuchardt, D. Cardoso, R. Sercheli, R. Pereira, R.S. da Cruz, M.C. Guerreiro, D. Mandelli, E. V. Spinace, E.L. Pires, *Appl. Catal. A: Gen.*, 211 (2001) 1–17.
9. G. W. Parshall, S. D. Ittel, *Homogenous Catalysis,* 2nd ed., Wiley, New York, 1992 Chapter 10.
10. H.H. Szmant, *Organic Building Blocks of the Chemical Industry*, Wiley, NewYork, 1989.
11. M. T. Musser, *Cyclohexanol and Cyclohexanone, Ullmann's Encyclopedia of Industrial Chemistry*, Wiley-VCH Verlag, Weinheim, 2007.
12. R. A. Sheldon, J. K. Kochi, *Metal-Catalyzed Oxidation of Organic Compounds*, Academic Press, New York, 1981, Chapters 2 and 11.

13. U. Schuchardt, R. Pereira, M. Rufo, *J. Mol. Catal. A: Chem.*, 135 (1998) 257–262.
14. M. H. N. Olsen, G. C. Salomão, V. Drago, C. Fernandes, A. Horn Jr., L. C. Filho, O. A. C. Antunes, *J. Supercrit. Fluids,* 34 (2005) 119–124.
15. J. W. Huang, W. Z. Huang, J. Liu, S. G. Hu, L. N. Ji, *J. Mol. Catal. A: Chem.*, 156 (2000) 275–278.
16. C. C. Guo, M. F. Chu, Y. Liu, D. C. Guo, X. Q. Liu, *Appl. Catal. A: Gen.*, 246 (2003) 303–309.
17. G. Huang, C. C. Guo, S. S. Tang, *J. Mol. Catal. A: Chem.*, 261 (2007) 125–130.
18. E. Amin, S. Nasser, P. H. Mohammad, *Appl. Catal. A: Gen*., 321 (2007) 135–139.
19. B. C. Hu, W. Y. Zhou, D. S. Ma, Z. L. Liu, *Catal. Commun.*, 10 (2008) 83–85.
20. A. Maldotti, A. Molinari, R. Amadelli, *Chem. Rev.* 102 (2002) 3811–3836.
21. Y. Shiraishi, T. Hirai, *J. Photochem. Photobiol. C: Photochem.*, 9 (2008) 157–170.
22. D. Tomova, V. Iliev, A. Eliyas, S. Rakovsky, *Sep. Purif. Technol.*, 156 (2015) 715–723.
23. Y. Ichihashi, M. Yamaguchi, Y. Nishikawa, K. Taniya, S. Tsuruya, S. Nishiyama, *Res. Chem. Intermed*., 36 (2010) 463–472.
24. S. M. Rodriguez, C. Richter, G. B. Galvez, M. Vincent, *Sol. Energy*, 56 (1996) 401–410.

25. S. Irmak, E. Kusvuran, O. Erbatur, *Appl. Catal. B: Environ.*, 54 (2004) 85–91.
26. E. B. Azevedo, F. R. Aquino Neto, M. Dezotti, *Appl. Catal. B: Environ.*, 54 (2004) 165–173.
27. W. Baran, A. Makowski, W. Wardas, *Dyes Pigm.*, 76 (2008) 226–230.
28. H. Tang, K. Prasad, R. Sanjine's, P. E. Schmid, F. Levy, *J. Appl. Phys.*, 75 (1994) 2042–2047.
29. T. Lindgren, J. M. Mwabora, E. Avendano, J. Jonsson, A. Hoel, C. G. Granqvist, *J. Phys. Chem. B*, 107 (2003) 5709–5716.
30. W. Erbs, J. Desilvestro, E. Borgarello, M. Gratzel, *J. Phys. Chem.*, 88 (1984) 4001–4006.
31. C. E. Taylor, R. P. Noceti, *Catal. Today*, 55 (2000) 259–267.
32. M. A. Gondal, A. Hameed, Z. H. Yamani, A. Arfaj, *Chem. Phys. Lett.*, 392 (2004) 372–377.
33. M. J. Munoz-Batista, A. Kubacka, R. Rachwalik, B. Bachiller-Baeza, M. Fernandez-Garcia, *J. Catal.*, 309 (2014) 428–438.
34. K. Villa, S. Murcia-Lopez, T. Andreu, J. R. Morante, *Catal. Commun.*, 58 (2015) 200–203.
35. O. Tomita, T. Otsubo, M. Higashi, B. Ohtani, R. Abe, *ACS Catal.*, 6 (2016) 1134–1144.
36. Y. Shiraishi, Y. Sugano, S. Ichikawa, T. Hirai, *Catal. Sci. Technol.*, 2 (2012) 400–405.
37. W. Wu, Z. Fu, S. Tang, S. Zou, X. Wen, Y. Meng, S. Sun, J. Deng, Y. Liu, D. Yin, *Appl. Catal. B: Environ.*, 154 (2015) 113–119.

38. Y. Ichihashi, S. Saijo, M. Taniguchi, K. Taniya, S. Nishiyama, *Mater. Sci. Forum*, 658 (2010) 149–152.
39. R. Abe, H. Takami, N. Murakami, B. Ohtani, *J. Am. Chem. Soc.*, 130 (2008) 7780–7781.
40. P. Boarini, V. Catassiti, A. Maldotto, R. Amedelli, *Langumuir*, 14 (1998) 2080–2085.

Chapter 4.2. Visible-Light-Responsible Titanium Oxide by Doping with Ferrous Ions for Photodecomposition of Ammonia

4.2.1. Introduction

As global energy needs continue to increase, fossil fuel resources are depleted, and serious environmental problems arise; modern society has been seeking new technologies to effectively address these issues [1–4]. Hydrogen has been identified as a promising future energy carrier. There is much interest in finding ways to produce hydrogen from renewable energy supplies, such as solar and wind resources, to avoid the emission of greenhouse gases inevitably released by its production from fossil fuels. Photocatalytic water splitting using solar energy can contribute a solution to problems arising from environmental and energy issues related to hydrogen production [5–7]. However, water splitting cannot proceed without sacrificial carbon-containing materials such as methanol or ethanol.

The photodecomposition of ammonia is an anticipated methodology as hydrogen production processes implement these requirements [8–12]. The photocatalytic process proceeds at room temperature and atmospheric pressure by only using clean and inexhaustible light energy. Furthermore, ammonia has a number of advantages as a hydrogen storage carrier as

follows: First, CO_2 is not exhausted in ammonia decomposition since it does not contain carbon. Second, ammonia can be easily transported and stored, as severe conditions are not necessary for its liquefaction. Finally, hydrogen content percentage in one molecule (NH_3: 17.6%) is high in comparison with that in other hydrogen storage carriers such as liquefied petroleum gas (LPG). As mentioned above, this photocatalytic process has the possibility of contributing to the establishment of a hydrogen energy recycling-based society.

Titanium dioxide (TiO_2) is an important semiconductor material used in a variety of applications, such as photo-splitting of water [1], photovoltaic devices [13], liquid solar cells [14], surface wettability conversion [15], and degradation of pollutants and toxic materials [16–19]. This wide applicability can be attributed to its nontoxicity, low cost, photostability, redox efficiency, and availability. However, the low efficiency of hydrogen production with TiO_2 is mainly due to its large bandgap (3.2 eV) located in the UV region of solar radiation, which accounts for only 4 % of the incoming solar energy [20,21], rendering the overall process impractical. Therefore, any shift in optical response from the UV to the visible range will have a profound positive effect on the photocatalytic efficiencies of TiO_2 materials [22–24]. TiO_2 doped with other low-cost 3d transition metals such as Fe and Cr [5,25] can extend its light absorption to the visible spectrum and improve the separation efficiency of photo-induced electrons and holes. Owing to the two main reasons stated above, TiO_2 doped with these low-cost metals can also display a higher photocatalytic activity of H_2

production than un-doped TiO_2 [5,25]. Furthermore, it should be noted that TiO_2 doped with Fe displays higher photocatalytic activity than TiO_2 containing other 3d transition-metal dopants [5,26–28]. Numerous studies pertaining to Fe-doped TiO_2 applied toward the decomposition of organic substances have been reported in the literature [29–36]. However, there are no reports of the application of TiO_2 doped with 3d transition metals toward H_2 production from ammonia. In this study, I have investigated the photodecomposition of ammonia by using several 3d transition metal-doped TiO_2 photocatalysts for the utilization of visible light.

4.2.2. Experimental

Metal-doped TiO_2 photocatalysts (M-TiO_2, M: dopant element) were prepared by a solid-state reaction [37]. A mixture of starting materials consisting of TiO_2 (Degussa P25), Cr_2O_3 (Nacalai Tesque), Fe_2O_3 (Nacalai Tesque), and H_2O was evaporated to dryness in a hot water bath at 363 K. The mixture was calcined at 1273 K for 10 h in air (M-TiO_2). For comparison, Fe loaded on a TiO_2 photocatalyst (Fe/TiO_2) was also prepared by the impregnation method with an aqueous solution of $[Fe(NO_3)_3]\cdot 9H_2O$. TiO_2 calcined at 1273 K was added into an aqueous solution in which the precursor was dissolved. The solution was evaporated to dryness in a hot water bath at 353 K. The sample was dried and then calcined under air-flow at 723 K (Fe/TiO_2). Platinization of M-TiO_2 or Fe/TiO_2 (Pt loading:

0.5 wt%) was carried out using a photodeposition method involving the irradiation of an aqueous suspension of TiO_2 with a 500 W Xe lamp for 2 h in the presence of methanol, H_2O, and H_2PtCl_6 [38]. After irradiation, the filtered Pt/M-TiO_2 sample was collected, washed with distilled water and then freeze-dried. The obtained sample was designated as Pt/M-TiO_2 (*n*) where *n* represents the content of metal doping.

The structural characterization of Pt/M-TiO_2 was carried out by X-ray diffraction (XRD) using CuKα radiation (Rigaku RINT-2100). Diffuse reflection (DR) spectra were obtained using a UV-visible diffuse reflectance (UV-vis-DR) spectrometer (Hitachi U-3210D) and were converted from reflection to absorption by the Kubelka–Munk method. Electron spin resonance (ESR) signals from both Fe^{3+} and Ti^{4+} ions were recorded in the X-band ($\lambda \cong 3.2$ cm) at room temperature on a spectrometer using a quartz dewar. The ESR signals were registered by the lack of saturation in the field range of 500–5500 G.

The photocatalytic reaction was carried out in a quartz-glass batch reactor. The photocatalyst (40 mg) was suspended in 5 mL of ammonia aqueous solution (0.59 mol/L). The reactor was purged with an Ar gas flow for 15 min. The reaction solution was then stirred with a magnetic stirrer and irradiated with a Xe lamp (500 W) through a color filter (Hoya UV-25) for 8 h. The gas phase products were analyzed by gas chromatography (Shimadzu GC-8A) equipped with a thermal conductivity detector using Ar carrier gas.

4.2.3. Results and Discussion

4.2.3.1. Photodecomposition reaction of aqueous ammonia

UV light irradiation of Pt loaded on TiO_2 photocatalysts (Pt/M-TiO_2) leads to the decomposition of an aqueous ammonia solution to hydrogen and nitrogen at room temperature. Table 1 shows the photocatalytic H_2 evolution from an aqueous solution of NH_3 over Pt-loaded TiO_2 photocatalysts modified with Fe or Cr (Pt/M-TiO_2, M = Fe, Cr) under UV light irradiation. In case of the reaction over Pt/TiO_2 with only H_2O as a reactant, no formation of H_2 was observed (Entries 1, 2). The photocatalytic activity of ammonia photodecomposition was increased when TiO_2 was doped with Fe (Pt/Fe-TiO_2), while the photocatalyst doped with Cr (Pt/Cr-TiO_2) showed almost similar photocatalytic activity as Pt/TiO_2 (Entries 2–4). Moreover, Pt/Fe-TiO_2 gave higher activity than TiO_2 impregnated with Fe (Pt/Fe/TiO_2, Entry 5). It is reported that when Cr^{3+} ions are partly substituted for Ti^{4+} ions in TiO_2, oxygen defects and/or Cr^{6+} ions are formed to keep the charge balance [37,39]. Cr^{6+} ions may play a role in the recombination centers between photogenerated electrons and holes. It is thus suggested that, for the above reasons, the Pt/Cr-TiO_2 photocatalyst deactivated in comparison with Pt/Fe-TiO_2 photocatalyst.

Reaction activity was examined using the Pt/Fe-TiO_2 photocatalyst, which had the highest activity. Fig. 1 shows the time profiles of H_2 and N_2 yields in the photocatalytic reaction of NH_3 solution over Pt/Fe-TiO_2. The

Table 1. Photocatalytic yield of H_2 under various conditions: Pt loading, 0.5 wt%; Fe and Cr dopant, 1.0 wt%.

Entry no.	Catalyst	Reactant	Yield of H2 (μmol/g-cat.)
1	Pt/TiO_2	H_2O	0
2	Pt/TiO_2	NH_3+H_2O	18
3	$Pt/Cr\text{-}TiO_2$	NH_3+H_2O	14
4	$Pt/Fe\text{-}TiO_2$	H_2O	0
5	$Pt/Fe\text{-}TiO_2$	NH_3+H_2O	27
6	$Pt/Fe\text{-}TiO_2$	NH_3+H_2O	10

formation of hydrogen and nitrogen is observed as soon as the reaction solution is exposed to UV light irradiation. The formation of products is not observed under dark conditions. The above results indicate that this reaction proceeds photocatalytically. Small quantities of N_2 formation was detected at the reaction time of 2 h and 3 h, although it was hard to determine the quantity. Nitrogen and hydrogen was found to be produced by the ratio of 1:3 until 7 h (see Fig. 1). It was seemed that nitrogen and hydrogen stoichiometrically produced from NH_3. From the mass spectrometry by using the deuterium oxide (D_2O), the photodecomposition of NH_3 in D_2O solution caused not the formation of D_2, but the formation of H_2. Hence, hydrogen formation is established as being derived from the photodecomposition of ammonia. As shown in Fig. 1 and Table 1, Pt/Fe-TiO_2 also gave the highest yield of H_2 via NH_3 photodecomposition. Therefore, further investigation was carried out for the most active Pt/Fe-TiO_2 photocatalyst.

4.2.3.2. Characterization of Fe-TiO_2 photocatalyst

The UV-vis-DR spectra of several photocatalysts are shown in Fig. 2. As made evident from the spectra, the light absorption edge of Fe-doped TiO_2 (Fe-TiO_2) was remarkably red-shifted to the visible light range compared with both TiO_2 impregnated with Fe (Fe/TiO_2) and pure TiO_2. The red shift in the absorption edge of Fe-TiO_2 can be attributed to the excitation of 3d electrons of Fe^{3+} ions to the TiO_2 conduction band (charge-

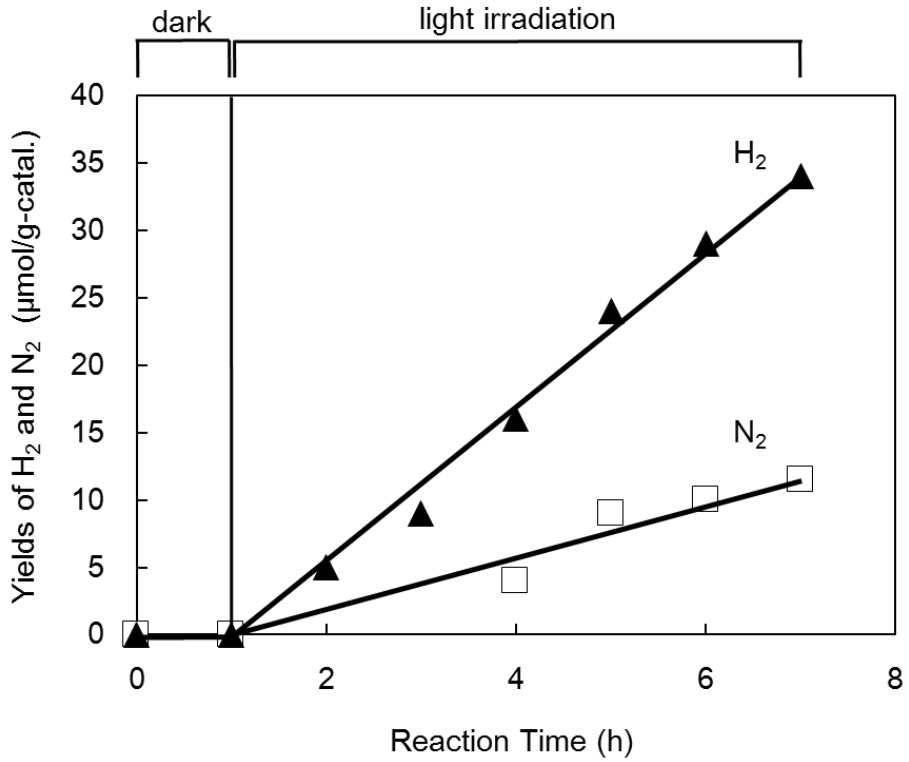

Figure 1. Time profiles of H_2 and N_2 yields for the photodecomposition of NH_3 aq. over Pt/Fe-TiO_2.

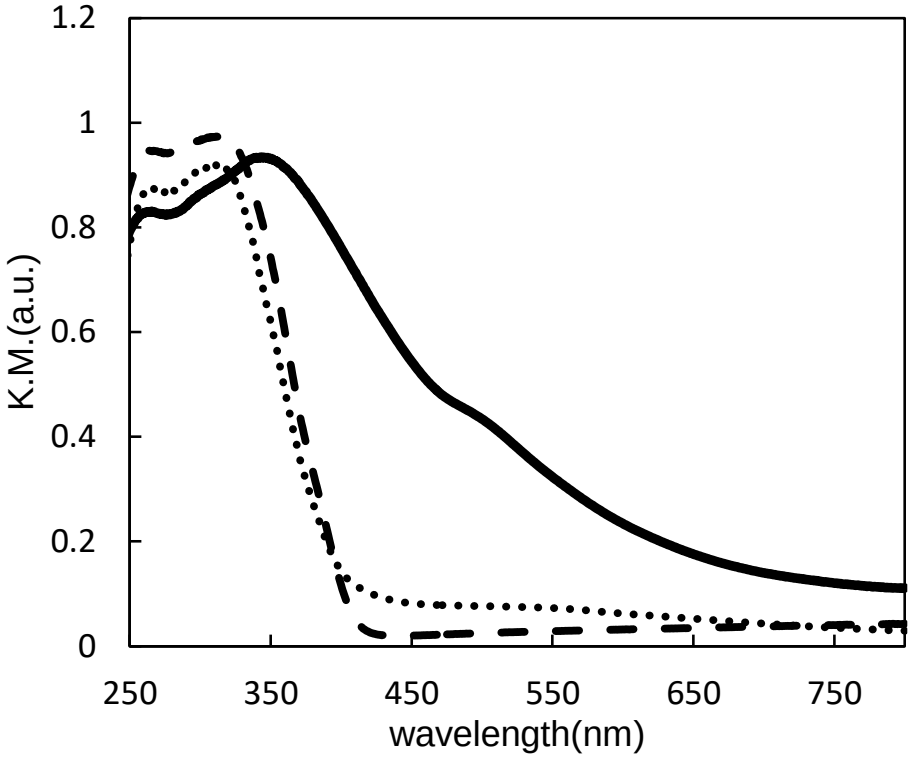

Figure 2. UV-vis-DR spectra of Fe-TiO_2, Fe/TiO_2 and TiO_2 photocatalysts.

transfer transition) [25]. From the photoluminescence measurements of Pt/Fe-TiO_2, Pt/Fe/TiO_2, and Pt/TiO_2 catalysts, the photoluminescence spectrum attributed to the impurity band was observed in only Pt/Fe-TiO_2 catalyst. Therefore, it is speculated that doping with Fe produces an impurity level in TiO_2. Accordingly, the substitution of Fe for Ti^{4+} may lead to the effective utilization of irradiated light. The decomposition of aqueous ammonia was also demonstrated over Fe loaded on TiO_2 photocatalysts prepared by an impregnation method (Fe/TiO_2). No effects attributed to Fe loading could be observed; the Fe/TiO_2 photocatalyst was not observed to utilize visible light ($\lambda > 420$ nm).

The ESR spectra of each catalyst are shown in Fig. 3. ESR spectroscopy is the technique for detecting and monitoring very low levels of transition metal–ion dopants [40]. Fig. 3(a)-(c) shows the spectra of Pt/TiO_2, Pt/Fe/TiO_2 and Pt/Fe-TiO_2 respectively. No peaks are observed in the spectrum of Pt/TiO_2 (see Fig. 3(a)); it is obvious that peaks attributed to Pt and Ti atoms are not observed. The spectrum of Pt/Fe/TiO_2 (Fig. 3(b)) has a signal at g = 2.08, which is assigned to the Fe^{3+} spin (S = 5/2) on the surface of TiO_2 [41, 42]. This observation verifies that Fe^{3+} exists within the anatase crystal lattice. In addition, the spectrum of the Pt/Fe-TiO_2 shown in Fig. 3(c) has signals present at g = 2.63, 3.37, 5.63, and 8.31, which are assigned to Fe^{3+} ions substituting for Ti^{4+} in the TiO_2 rutile lattice [43]. The Fe dopant can be inserted into the TiO_2 lattice as a Fe impurity band below the conduction band and above the valance band of TiO_2, creating an optical band gap [6, 44]. It has been reported that electrons in the valence

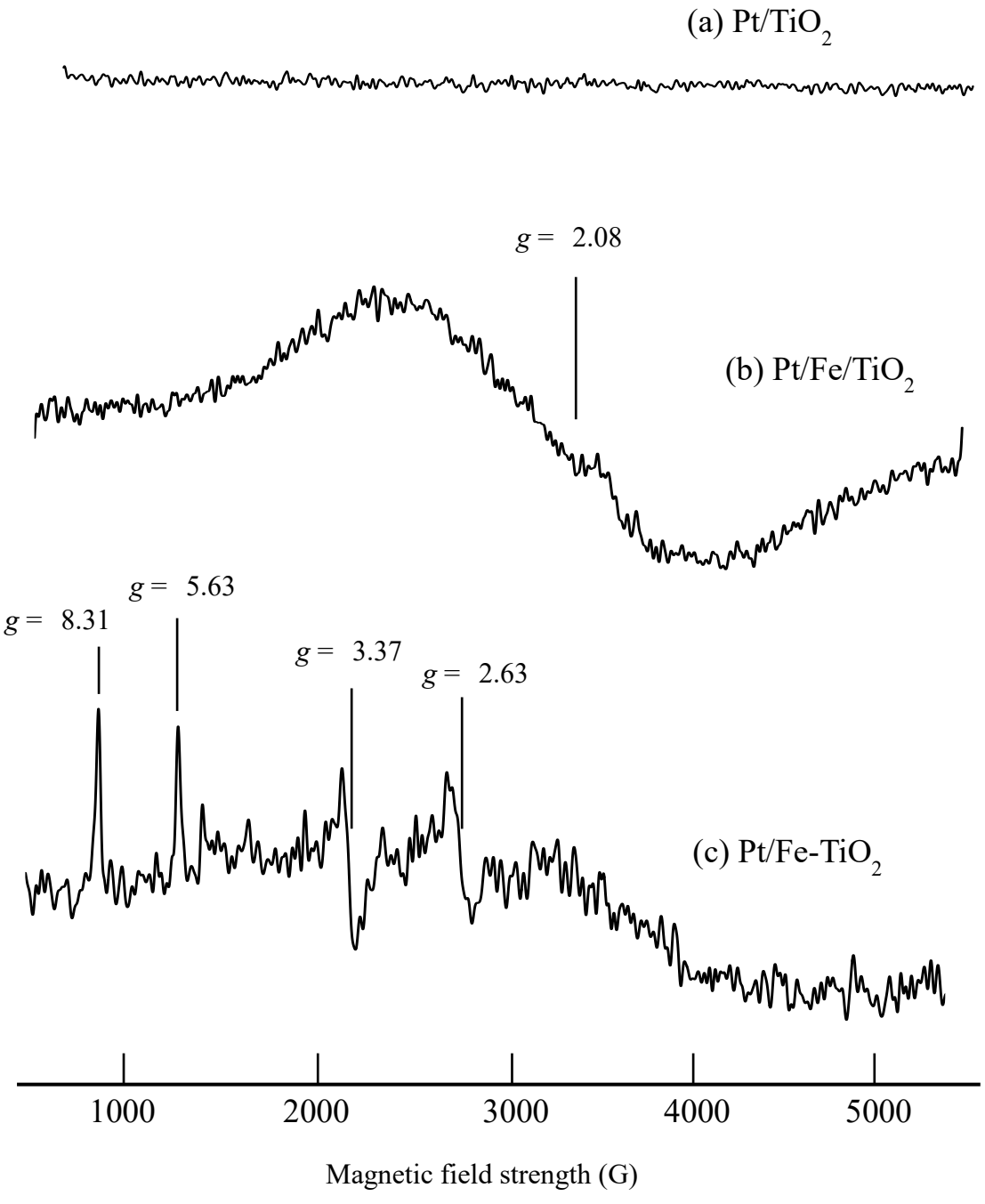

Figure 3. ESR spectra of Pt/TiO_2 (a), $Pt/Fe/TiO_2$ (b) and $Pt/Fe\text{-}TiO_2$ (c) photocatalysts.

band of TiO_2 can firstly transfer to the Fe impurity band, and these electrons can then transfer from the impurity band to the conduction band through absorption of other photons. The excited electrons appear in the conduction band and holes in the valence band are subsequently formed [6]. Therefore, it is speculated that the substitution of Ti^{4+} with Fe^{3+} in Fe-TiO_2 leads to the effective utilization of irradiated light owing to the presence of a Fe impurity band.

Fig. 4 shows the XRD patterns of TiO_2 photocatalysts. Only rutile TiO_2 peaks were observed, and no peaks attributed to Fe or Cr species can be observed in these patterns. Fe^{3+} metal ions have an effective diameter comparable to those of Ti^{4+} ions. Thus, it is suggested that the dopant metals substituted for portions of the Ti^{4+} sites in TiO_2 crystal do not effect a change in the TiO_2 structure [37]. According to the above results obtained from UV-vis, ESR, and XRD analyses, it is speculated that TiO_2 has the ability to use not only UV light but also visible light by substituting Fe^{3+} for Ti^{4+} in its lattice.

4.2.4. Conclusion

Photocatalysts prepared by the loading of Pt on metal-doped TiO_2 (Pt/M-TiO_2) are shown to effectively decompose aqueous NH_3 to H_2 and N_2 under UV irradiation at room temperature. The Pt-loaded TiO_2 photocatalyst modified with iron (Pt/Fe–TiO_2) led to a higher activity than

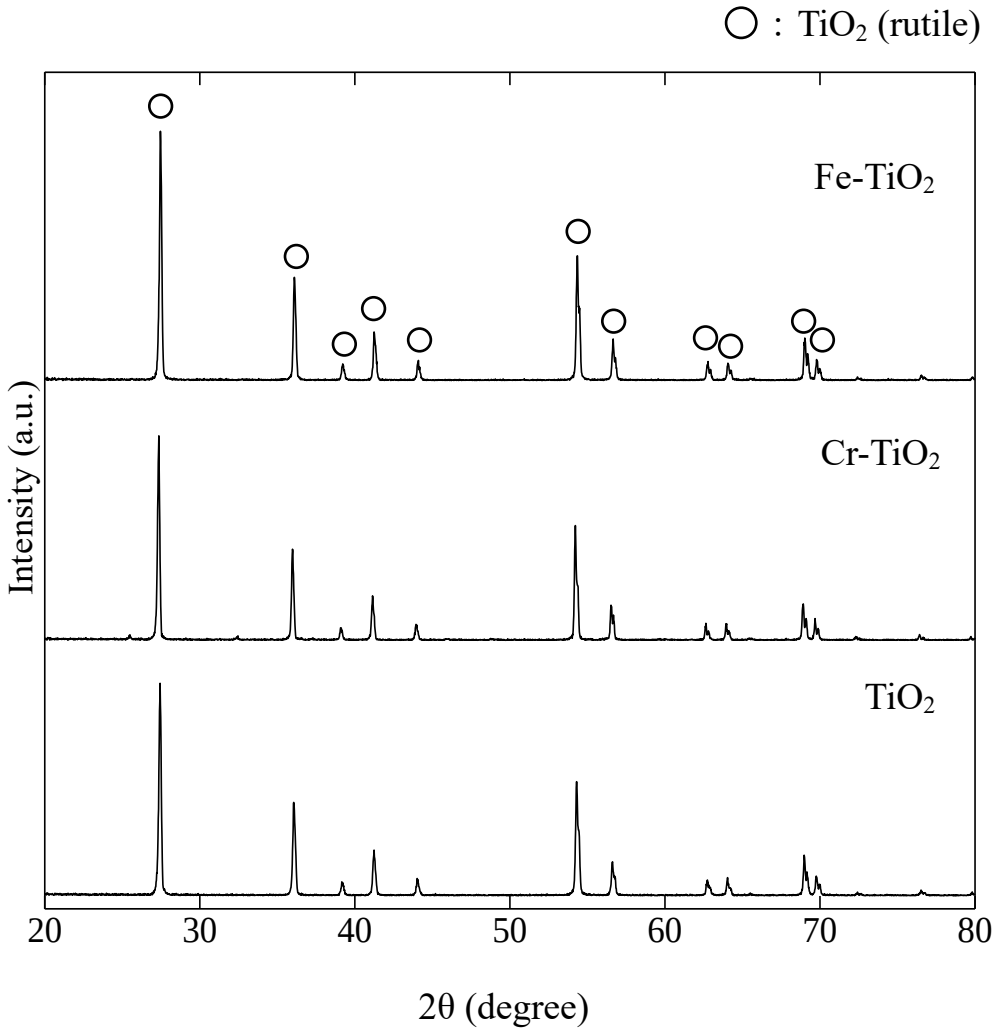

Figure 4. XRD patterns of TiO_2 and metal ion-doped TiO_2 photocatalysts.

either chromium-doped (Pt/Cr–TiO_2) or undoped TiO_2 photocatalysts (Pt/TiO_2). It was found from UV–vis, ESR, and XRD measurements that by substituting Fe^{3+} for Ti^{4+}, the resulting Fe–TiO_2 catalyst material might allow for the effective utilization of irradiation light owing to the presence of a Fe impurity band, thereby leading to its higher activity.

References

1. A. Fujishima, K. Honda, *Nature*, 238 (1972) 37–39.
2. K. Maeda, R. Abe, K. Domen, *J. Phys. Chem. C*, 115 (2011) 3057–3064.
3. J. P. Dorian, H. T. Franssen, D. R. Simbeck, *Energy Policy*, 34 (2006) 1984–1991.
4. Y. Mu, X. J. Zheng, H. Q. Yu, R. F. Zhu, *Int. J. Hydrogen Energy*, 31 (2006) 780–785.
5. R. Dholam, N. Patel, M. Adami, A. Miotello, *Int. J. Hydro. Energy*, 34 (2009) 5337–5346.
6. T. Sun, E. Liu, J. Fan, X. Hu, F. Wu, W. Hou, Y. Yang, L. Kang, *Chem. Eng. J.*, 228 (2013) 896–906.
7. M. Momirlan, T. N. Veziroglu, *Renew. Sust. Energy Rev.* 6 (2002) 141–179.
8. K. Kitagawa, S. Saijo, Y. Ichihashi, S. Nishiyama, *13th Asia Pacific Confederation of Chemical Engineering Congress* (2010) 10295.
9. Q.S. Li, K. Domen, S. Naito, T. Onishi, K. Tamaru, *Chem. Lett.* (1983)

321−324.

10. M. Kaneko, N. Gokan, N. Katakura, Y. Takei, M. Hoshino, *Chem. Commun*., 2005 (2005) 1625–1627.
11. N. Maffei, L. Pelletier, J. P. Charland, A. McFarlan, *J. Power Sources*, 140 (2005) 264–267.
12. L. Pelletier, A. McFarlan, N. Maffei, *J. Power Sources*, 145 (2005) 262–265.
13. A. L. Linsebigler, G. Lu, J. T. Yates, *Chem. Rev.* 95 3 (1995) 735–758.
14. B. O' Regan, M. Gratzel, *Nature* 353 (1991) 737–740.
15. R. Wang, N. Sakai, A. Fujishima, T. Watanabe, K. Hashimoto, *J. Phys. Chem. B,* 103 (1999) 2188.
16. S. M. Rodriguez, C. Richter, G. B. Galvez, M. Vincent, *Sol. Energy*, 56 (1996) 401–410.
17. S. Irmak, E. Kusvuran, O. Erbatur, *Appl. Catal., B: Environ.*, 54 (2004) 85–91.
18. E. B. Azevedo, F. R. A. Neto, M. Dezotti, *Appl. Catal., B: Environ.*, 54 (2004) 165–173.
19. W. Baran, A. Makowski, W. Wardas, *Dyes Pigm.*, 76 (2008) 226–230.
20. H. Tang, K. Prasad, R. Sanjine`s, PE. Schmid, F. Lévy, *J. Appl. Phys.*, 75 (1994) 2042–2047.
21. T. Lindgren, J.M. Mwabora, E. Avendaño, J. Jonsson, A. Hoel, C.G. Granqvist, et al., *J. Phys. Chem. B*, 107 (2003) 5709–5716.
22. R. Asahi, T. Morikawa, T. Ohwaki, K. Aoki, Y. Taga, *Science* 293 (2003) 269–271.

23. M. Anpo, Y. Ichihashi, M. Takeuchi, H. Yamashita, *Res. Chem. Intermed.*, 24 (1998) 143–149.
24. H. Yamashita, Y. Ichihashi, M. Takeuchi, S. Kishiguchi, M. Anpo, *J. Synchrotron Radiat.*, 6 (1999) 451–452.
25. M.A. Khan, S. I. Woo, O. B. Yang, *Int. J. Hydrogen Energy*, 33 (2008) 5345–5351.
26. L. Pan, J. J. Zou, X. W. Zhang, L. Wang, *Ind. Eng. Chem. Res.*, 49 (2010) 8526–8531.
27. E. D. Jeong, P. H. Borse, J. S. Jang, J. S. Lee, O. S. Jung, H. Chang, J. S. Jin, M. S. Won, H. G. Kim, *J. Ceram. Process. Res.*, 9 (2008) 250–253.
28. W. Choi, A. Termin, M. R. Hoffmann, *J. Phys. Chem.*, 98 (1994) 13669–13679.
29. J. A. Navio, G. Coloh, M. I. Litter, G. N. Bianco, *J. Mol. Catal. A: Chem.*, 106 (1996) 267–276.
30. J. W. Shi, *Chem. Eng. J.* 151 (2009) 241–246.
31. Y. Cong, J. L. Zhang, F. Chen, M. Anpo, D. N. He, *J. Phys. Chem. C*, 111 (2007) 10618–10623.
32. J. Zhu, J. Ren, Y.N. Huo, Z.F. Bian, H.X. Li, *J. Phys. Chem. C*, 111 (2007) 18965–18969.
33. L. F. Liu, F. Chen, F. L. Yang, Y. S. Chen, J. Crittenden, *Chem. Eng. J.*, 181–182 (2012) 189–195.
34. Z. J. Li, W. Z. Shen, W. S. He, X. T. Zu, *J. Hazard. Mater.*, 155 (2008) 590–594.
35. B. Naik, K. M. Parida, *Ind. Eng. Chem. Res.*, 49 (2010) 8339–8346.

36. J. X. Li, J. H. Xu, W. L. Dai, H. X. Li, K. N. Fan, *Appl. Catal. B: Environ.*, 85 (2009) 162–170.
37. H. Kato, A. Kudo, *J. Phys. Chem. B*, 106 (2002) 5029–5034.
38. J. Nemoto, N. Gokan, H. Ueno, M. Kaneko, *J. Photochem. Photobiol. A: Chem.*, 185 (2007) 295–300.
39. T. Ishii, H. Kato, A. Kudo, *J. Photochem. Photobiol. A: Chem.*, 163 (2004) 181–186.
40. T. A. Egerton, E. Harris, E. J. Lawson, B. Mile, C. C. Rowlands, *Phys. Chem. Chem. Phys.*, 3 (2001) 497–504.
41. K. T. Ranjit, B. Viswanathan, *J. Photochem. Photobiol. A: Chem.*, 108 (1997) 79–84.
42. J. Zhu, F. Chen, J. Zhang, H. Chenb, M. Anpo, *J. Photochem. Photobiol. A: Chem.*, 180 (2006) 196–204.
43. N. G. Maksinov, I. L. Mikhailova, V. F. Anufrenko, *Kinet. Catal.* 13 (1973) 1162.
44. Y. Yalcin, M. Kilic, Z. Cinar, *Appl. Catal., B: Environ.*, 99 (2010) 469–477.

Chapter 4.3. Reaction Mechanism of Ammonia Photodecomposition Catalysed by Titanium Oxide

4.3.1. Introduction

Photocatalytic reactions have been widely investigated in owing to its potential applications in environmental cleaning and energy generation with increasing concerns on environment and energy issues caused by the utilization of nonrenewable fossil fuels. [1-3]. One of the photocatalytic reactions is a process to produce H_2 as energy resources and it is expected to contribute to the establishment of H_2 production for renewable energy economically and environmentally [1, 2, 4, 5].

It is well known that there are no sources of free H_2 in nature. Hydrogen is produced from hydrogen-containing compounds [6]. The photocatalytic splitting of water has been considered an excellent alternative source of energy since Fujishima and Honda reported the potential use of titanium dioxide (TiO_2) as a photoelectrode for water electrolysis and the production of oxygen and hydrogen [3]. Recently, the use of NH_3 has been made many efforts to develop technology for storage and supply of H_2 [6, 7]. NH_3 has high energy density and high hydrogen storage capacity of 17.6 wt% in comparison with other carriers such as cyclohexane, ethanol, and liquefied petroleum gas (LPG). CO_2 is not exhausted from the NH_3 decomposition

since it does not include carbon. NH_3 can be easily stored and transported in liquid because NH_3 gas is liquefied by pressuring to 8.5 MPa at 20℃. Photodecompositions have attracted much attention in terms of milder reaction conditions and a lower environmental burden than thermal decompositions. Thus, photocatalytic reactions for H_2 production in an aqueous NH_3 solution are so much useful and fascinating [8-10].

TiO_2 is one of the most popular materials for photocatalysis because of its low price, availability, chemical stability, low toxicity, and light conversion efficiency [11-17]. TiO_2 is an indirect band gap semiconductor with energy gap of 3.2 eV. TiO_2 have good optical properties and good photocatalytic activity in the UV region [18]. However, its photocatalytic efficiency is still relatively low because of the fast recombination of photoinduced charge carriers. Many strategies have been developed in order to improve the photocatalytic efficiency of TiO_2 through doping with a second component which promotes photon-to-electron conversion efficiency and charge separation. Our laboratory has recently demonstrated that the loading of Pt on Fe doped TiO_2 photocatalyst displays a higher activity of H_2 production on the NH_3 decomposition [10]. However, to the best our knowledge, the mechanism of the NH_3 decomposition are still not well understood [7-10]. Quantum chemical calculation is very effective method to reveal the microcosmic mechanism of complex chemical reaction, it can provide the information about change of the structure and the chemical reaction energy [21]. It may provide hints for further developments of efficient catalytic systems.

In this study, an attempt is made to produce H_2 from the NH_3 (aq.) decomposition catalyzed by noble metal free TiO_2 photocatalysts. I report theoretical calculations to investigate the detailed reaction mechanism and describe experiments designed to more deeply probe the mechanism of these reactions. A combination of ESR measurement results and DFT calculations have led us to propose reasonable reaction mechanism [22-28].

4.3.2. Experimental

4.3.2.1. Catalyst preparation

Metal loaded TiO_2 (JRC-TIO-4 supplied from the Catalysis Society of Japan) photocatalysts were prepared by the impregnation method with an aqueous solution of $Ni(NO)_3 \cdot 6H_2O$ (0.26 g) in ion exchanged water (50 ml). TiO_2 (1.00 g) was added into an aqueous solution in which the precursor was dissolved. The mixture was evaporated in vacuum at 353 K, and then the sample was dried overnight at room temperature. The obtained powder was calcined under airflow at 723 K for 5 h, and then reduced by hydrogen at 723 K for 3 h. The obtained solid was designated as 5 wt% M/TiO_2 (M=V, Cr, Mn, Fe, Co, Cu, Zn, and Pt by using NH_4VO_3, $Cr(NO_3)_2 \cdot 6H_2O$, $Mn(NO_3)_2 \cdot 6H_2O$, $Fe(NO_3)_3 \cdot 9H_2O$, $CoCl_2 \cdot 6H_2O$, $Cu(NO_3)_2 \cdot 3H_2O$, $Zn(NO_3)_2 \cdot 6H_2O$, H_2PtCl_6).

4.3.2.2. Photocatalytic decomposition of NH_3

Hydrogen production from the photocatalytic reaction was performed in a quartz-glass batch reactor. The prepared solid (20 mg) was suspended in 5 mL of ammonia aqueous solution (0.59 mol/L). The reactor was purged with Ar gas flow for 20 min to remove air completely. The reaction solution was magnetically stirred and irradiated with a Xe lamp (500 W) through a color filter (Hoya UV-25) for 3 h. The gas phase products were analyzed by gas chromatography (Shimadzu GC-8A) equipped with a thermal conductivity detector using Ar carrier gas and by mass spectrometry using a quadrupole mass spectrometer (QME220).

4.3.2.3. Characterisation

The powder X-ray diffraction (XRD) measurement was performed using a Rigaku RINT-2100 system with Cu Kα radiation (λ=1.5406 Å). Electron spin resonance (ESR) data was recorded using a X-band spectrometer (BRUKER ESR300E). The experimental procedure for the photocomposition of NH_3 was as follow: the catalyst was placed into a glass cell with a quartz ESR cell and an attached 3-way stopcock. The cell was charged with H_2 (100 Torr), heated at 623 K for 30 min, and then evacuated at room temperature to remove H_2 completely. The reduced sample was transferred into the ESR cell, followed by introduction of gaseous NH_3 (110 Torr) for absorbing NH_3 to the sample surface. NH_3 charged in the cell was

then evacuated until the pressure inside decreased less than 3 Torr. ESR spectrum was recorded at 77 K under UV light irradiation.

4.3.2.4. Computational methods

Calculation model is shown in Fig. 1. DFT calculations were performed using the Gaussian 03 package. All calculations used the spin-unrestricted hybrid density functional B3LYP and a basis set (LanL2DZ) and molecular geometries of all models were fully optimized. And also calculations were applied triplet excited state (Spin=triplet) owing to account for TiO_2 photoexcitation.

4.3.3. Results and discussion

4.3.3.1. Photocatalytic decomposition of NH_3

Photocatalytic H_2 production from NH_3 over as-prepared TiO_2 catalysts (M/TiO_2) loaded with variety of metal is evaluated under UV irradiation in an aqueous NH_3 solution at room temperature (see Table 1). It is found that H_2 is obtained in a yield of 8.7 μmol/g-catalyst over pure TiO_2 (Entry1). Photocatalytic activities of TiO_2 catalysts loaded several transition metals except Ni are almost equal to that of pure TiO_2 (Entry 2-7). It is found that Ni/TiO_2 effectively enhances H_2 formation (Entry 8). The time

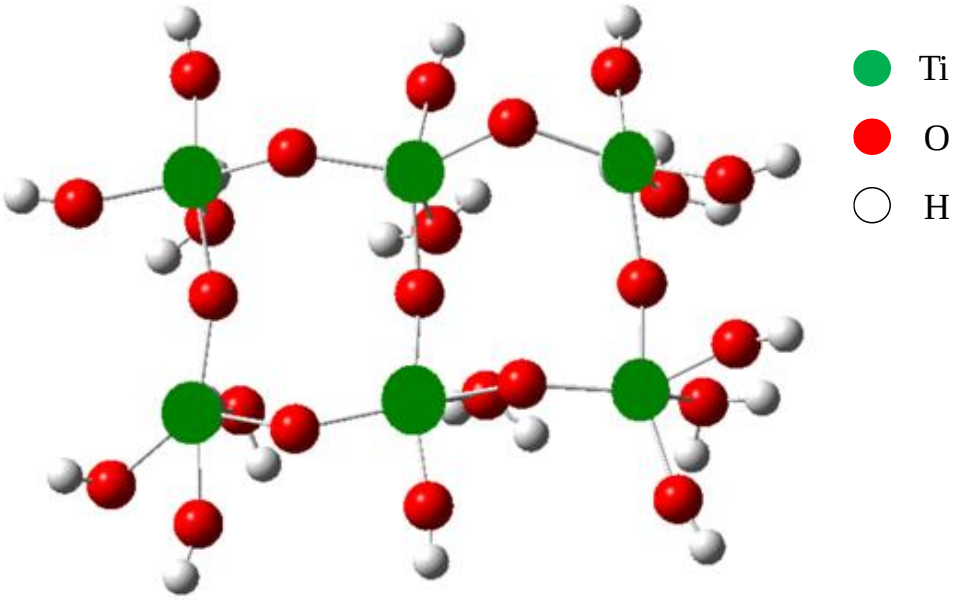

Figure 1. TiO_2 cluster model.

Table 1. Photocatalytic yield of H_2 over M/TiO_2 (0.5 wt%).

Entry no.	Catalysts	Yield of H_2 (μmol/g-cat.)
1	TiO_2	8.7
2	V/TiO_2	6.0
3	Cr/TiO_2	7.0
4	Mn/TiO_2	7.2
5	Fe/TiO_2	6.7
6	Co/TiO_2	6.3
7	Cu/TiO_2	6.8
8	Ni/TiO_2	131.7
9	Ni/TiO_2[a]	8.4

[a]Without reduction.

profiles of H_2 and N_2 yields in the NH_3 (aq.) decomposition over Ni/TiO_2 is represented in Fig. 2. No formation of H_2 and N_2 is observed during dark condition. UV light irradiation causes the formation of H_2 and N_2, and the yields linearly increase with increasing reaction time. H_2 and N_2 are found to be produced at a rate of 1:3, indicating they are stoichiometrically produced from the NH_3 photodecomposition. It is also confirmed hydrogen forms from the NH_3 decomposition by MS using deuterium oxide (D_2O). As shown in Fig. 3, the signal of H_2 (m/z = 2) is observed but not found the signal of D_2 (m/z = 4) on the NH_3 decomposition in D_2O solution. Hence, it is clear that hydrogen formation is derived from the photodecomposition of NH_3.

4.3.3.2. Characterisation of R-Ni/TiO_2

The XRD patterns of TiO_2 and Ni/TiO_2 before and after the reaction are shown in Fig. 4. In the diffractions of Fig. 4 (b) and (c), the peak assigned to Ni^0 (111) at 2θ=44.5 ° and the peaks attributed to rutile TiO_2 are observed [19-24]. Figure 4 (c) shows similar diffraction to that of Fig. 4 (b). This result indicates that crystal structures of TiO_2 and Ni metal are stable during the reaction in NH_3 aqueous solution. It is also suggested that Ni^0 on TiO_2 enhances the NH_3 decomposition because Ni^0 exists in the catalyst having a high catalytic activity.

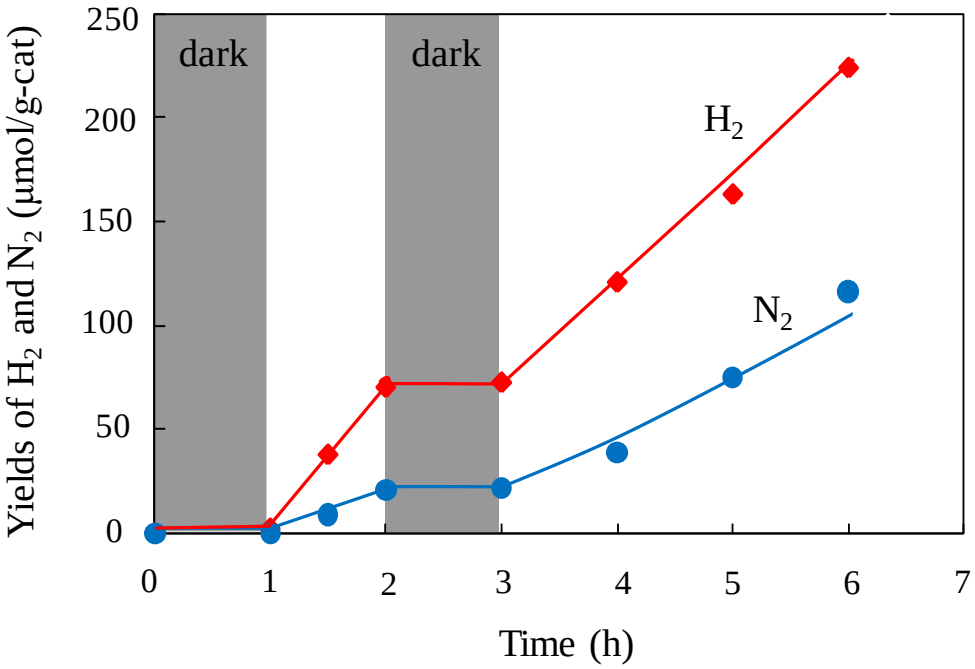

Figure 2. Time profiles of H_2 and N_2 yields for the NH_3 photodecomposition over Ni/TiO_2.

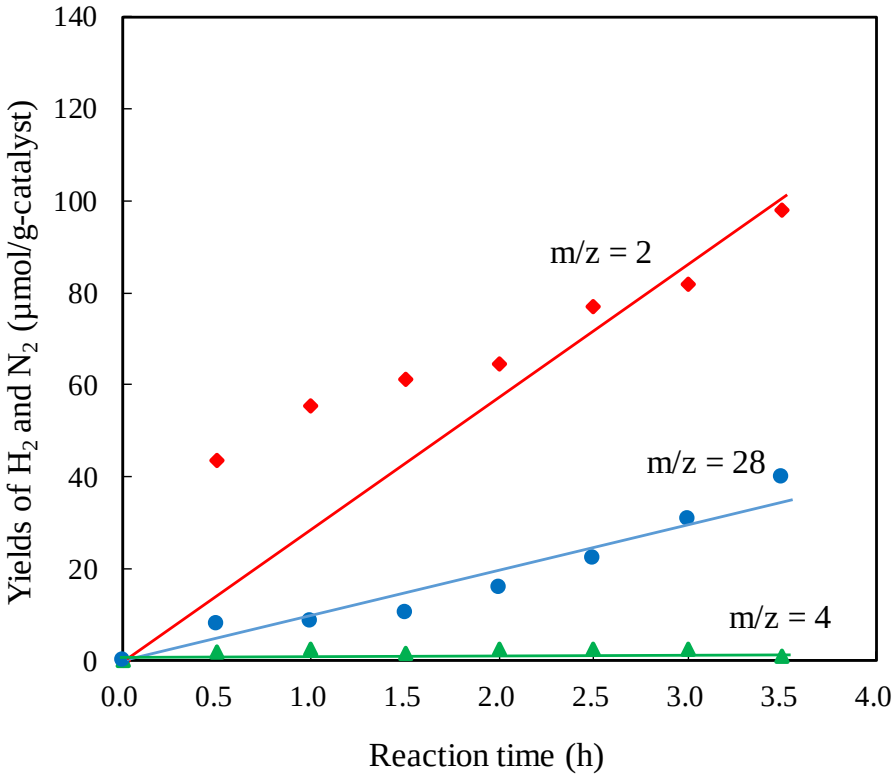

Figure 3. Time profiles of products yields for the NH_3 photodecomposition over Ni/TiO_2 (1.0 wt%) in gas phase reaction (Reactant : $NH_3 + D_2O$).

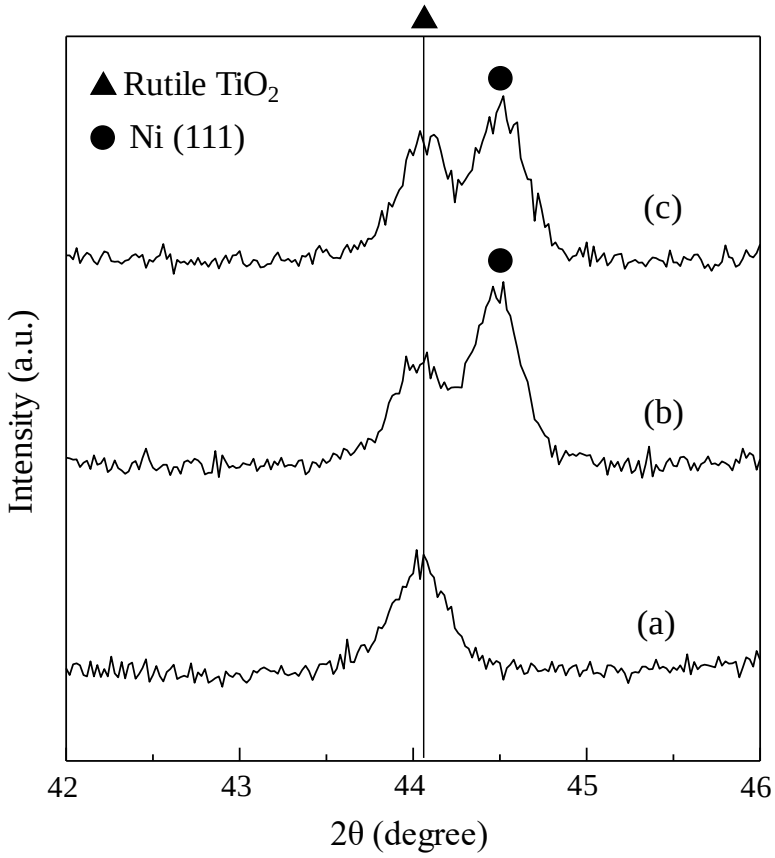

Figure 4. XRD patterns of TiO_2 (a), Ni/TiO_2 before the reaction (b) and Ni/TiO_2 after the reaction (c).

4.3.3.3. Reaction mechanism of NH_3 decomposition over TiO_2 photocatalyst

ESR measurement was employed to observe the formation of intermediates during the NH_3 decomposition reaction. The ESR spectra of Ni/TiO_2 are shown in Fig 5. Spectra of Fig. 5 (a) and (b) exhibit a signal at g = 2.006 assigned to TiO_2 [25]. Spectrum of Fig. 5 (c), which is measured during UV irradiations, shows a signal at g=2.004 assigned to a NH_2 radical [26, 27]. The result of ESR measurement indicates that a NH_2 radical forms as a dominant intermediate from NH_3 photodecomposition. It is suggested that a NH_2 radical is formed through extraction of hydrogen atom from NH_3. To further investigate the reaction pathways in which H_2 and N_2 form via a NH_2 radical in the NH_3 decomposition, three pathways are proposed (see scheme 1). The Gibbs free energy is estimated for each elementary step of the three reaction pathways (see Fig. 6-8). The NH_3 absorption to TiO_2 surface is studied as the first step of the reaction mechanism in any pathways. The two molecules of NH_3 absorption to TiO_2 surface was exothermic step by 7.4 kcal/mol.

Route 1 is the reaction pathway of NH_3 photodecomposition via the NH radical through extraction of H atom (see scheme 1). Fig. 6 shows energy diagram from NH_3 absorption to the formation of N_2 and H_2 in route 1. The NH_2 radical forms through extraction of H atom from the NH_3 absorbing on TiO_2. The NH_2 radical formation step is 20.8 kcal/mol higher than the state of NH_3 absorption (*1*→*2*). H_2 desorption to form the NH

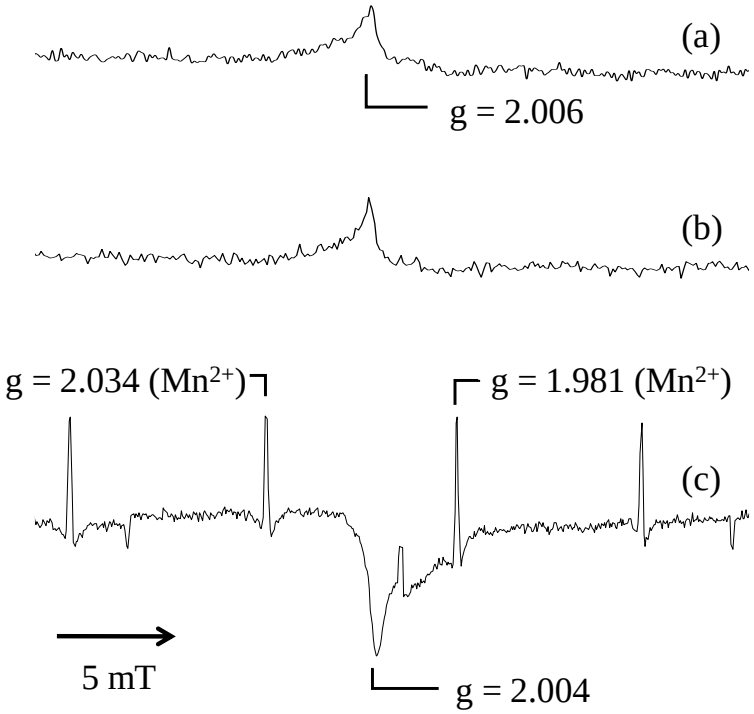

Figure 5. ESR spectra of Ni/TiO_2 (a), NH_3 absorption before photoirradiation (b), and under photoirradiation (c) in the NH_3 gas of 3 Torr at 77 K).

radicals occurs through extraction of each hydrogen atom from the two NH_2 radicals. The step of NH radical formation from the NH_2 radical requires 77.7 kcal/mol (*2→R1_3*). The N radical forms through extraction of H atom form the NH radical and is at the highest free energy in route 1 (*R1_3 →R1_4*). The coupling of N radicals gives N_2. (*R1_4→5→6*). The activation energy in route 1 for H_2 and N_2 formation from NH_3 decomposition is estimated to be 236 kcal/mol.

Route 2 is the reaction pathway of NH_3 photodecomposition via the H_2N-NH_2 which forms by the coupling of adjacent NH_2 radicals (see scheme 1). Fig. 7 shows energy diagram from NH_3 absorption to the formation of N_2 and H_2 in route 2. The NH_2 radical forms through extraction of H atom from the NH_3 absorbing on TiO_2 (*1→2*). The coupling of adjacent NH_2 radicals gives H_2N-NH_2. The NH_2-NH_2 formation is exothermic step by 14.9 kcal/mol (*2→R2,2'_4*). The N=N radical is given through extraction of two hydrogen molecules from the H_2N-NH_2 by 74.4 kcal/mol (*R2,2'_4→ 5*). After the formation of the N=N radical, N_2 is obtained from the N=N radical like route 1 (*5→6*). The N=N radical has the highest energy in route 2. The activation energy in route 2 for H_2 and N_2 formation from NH_3 decomposition is estimated to be 74.4 kcal/mol.

Route 2' is the reaction pathway of NH_3 photodecomposition via the H_2N-NH_2 formation step on which one NH_2 radical reacts with NH_3 in the gas phase (see scheme 1). Fig. 8 shows energy diagram from NH_3

absorption to the formation of N_2 and H_2 in route 2'. The NH_2 radical forms through extraction of H atom from the NH_3 absorbing on TiO_2 and has been located at a free energy of 23.4 kcal/mol (*1'→2'*). The H_2N-NH_3 forms by the coupling of the NH_2 radical and NH_3 molecule. The H_2N-NH_3 formation is exergonic step by 19.3 kcal/mol (*2'→R2'_3*). The H_2N-NH_2 forms through extraction of each hydrogen atom from two molecules of H_2N-NH_3 with H_2 desorption (*R2'_3→R2, 2'_4*). After the formation of the H_2N-NH_2, N_2 and H_2 form from H_2N-NH_2 as well as route 2 (*R2, 2'_4→5→6)*. The activation energy in route 2' for H_2 and N_2 formation from NH_3 decomposition is estimated to be 65.8 kcal/mol.

According to the above results obtained from DFT calculations, the activation energies for the NH_3 decomposition to N_2 and H_2 are 236 and 74.4 kcal/mol in pathways route 1 and route 2 respectively. The activation energy of route 2 is much lower than that of route 1. It is found that route 2 is more favorable pathway than route 1. Hence, it is suggested that H_2 and N_2 forms via H_2N-NH_2 from the NH_3 decomposition reaction. On the other hand, the required energy for the formation of H_2N-NH_2 as an intermediate are 20.8 and 7.8 kcal/mol in pathways route 2 and route 2' respectively. Therefore, the H_2N-NH_2 formation by the coupling of one NH_2 radical and ammonia is thermodynamically favored. The activation energies are estimated to be 74.4 kcal/mol, 59.2 kcal/mol respectively. But these required energies are not significantly different between route 2 and route 2'. There is a possibility that the NH_3 decomposition proceeds in both

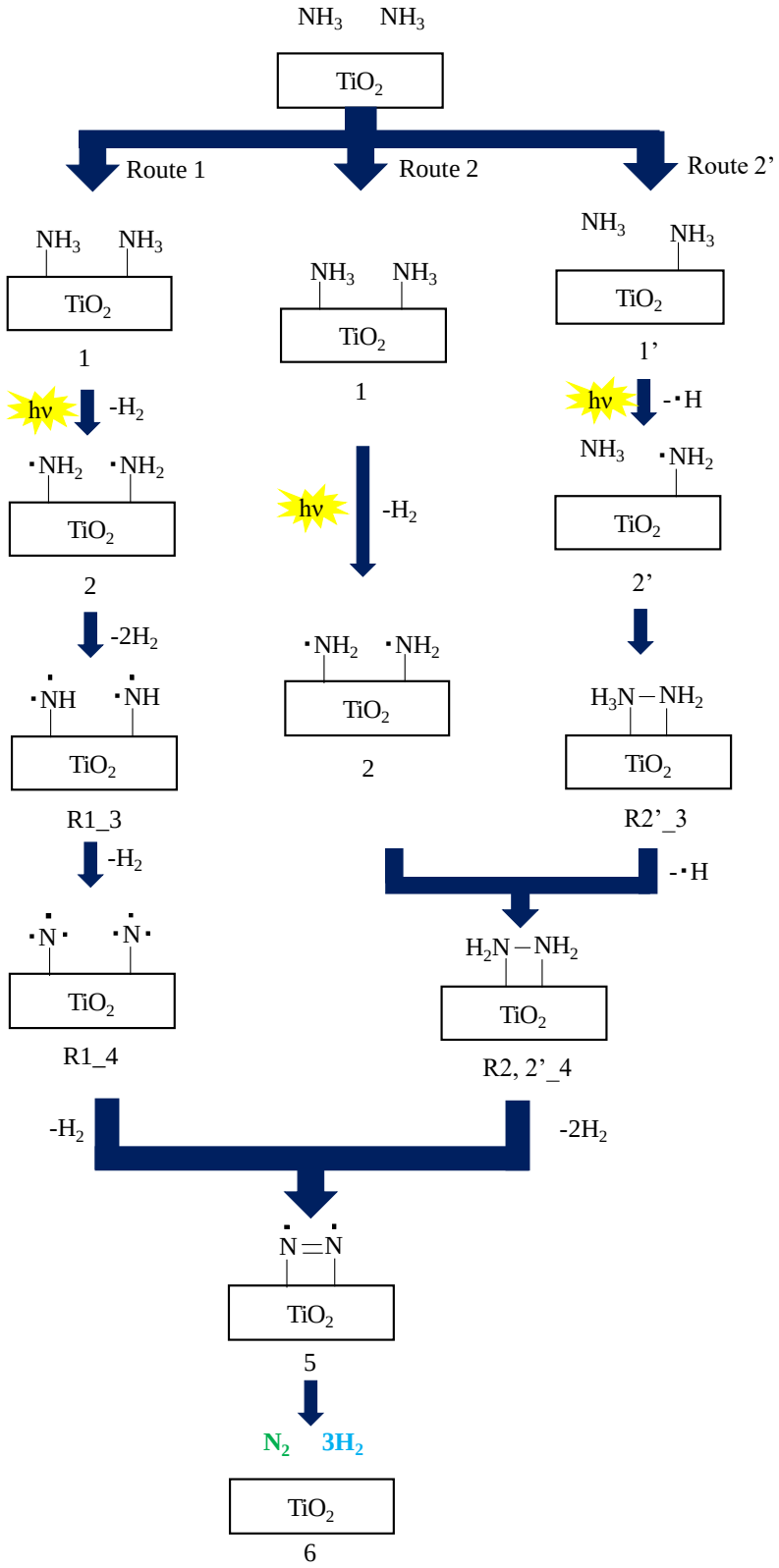

Scheme 1. Suggested reaction mechanism for NH_3 decomposition to N_2 and H_2 over TiO_2 photocatalyst.

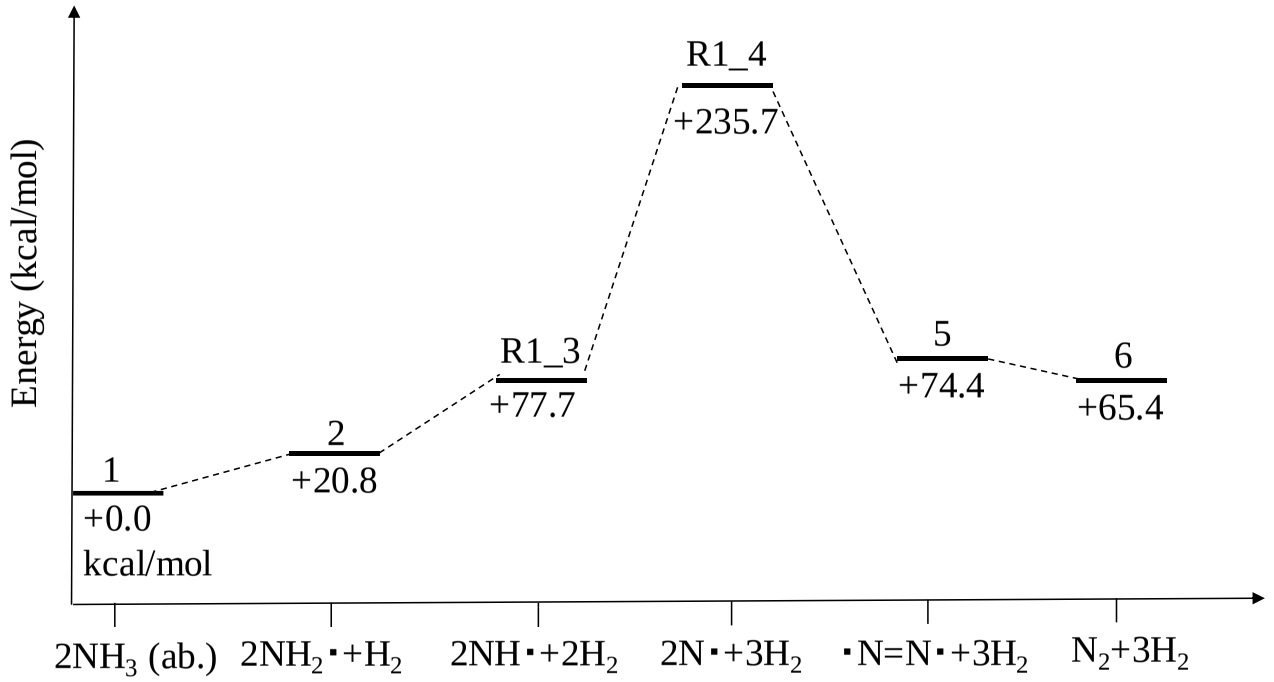

Figure 6. Energy diagram for the NH_3 decomposition to N_2 and H_2 in pathway route 1 over TiO_2 photocatalyst.

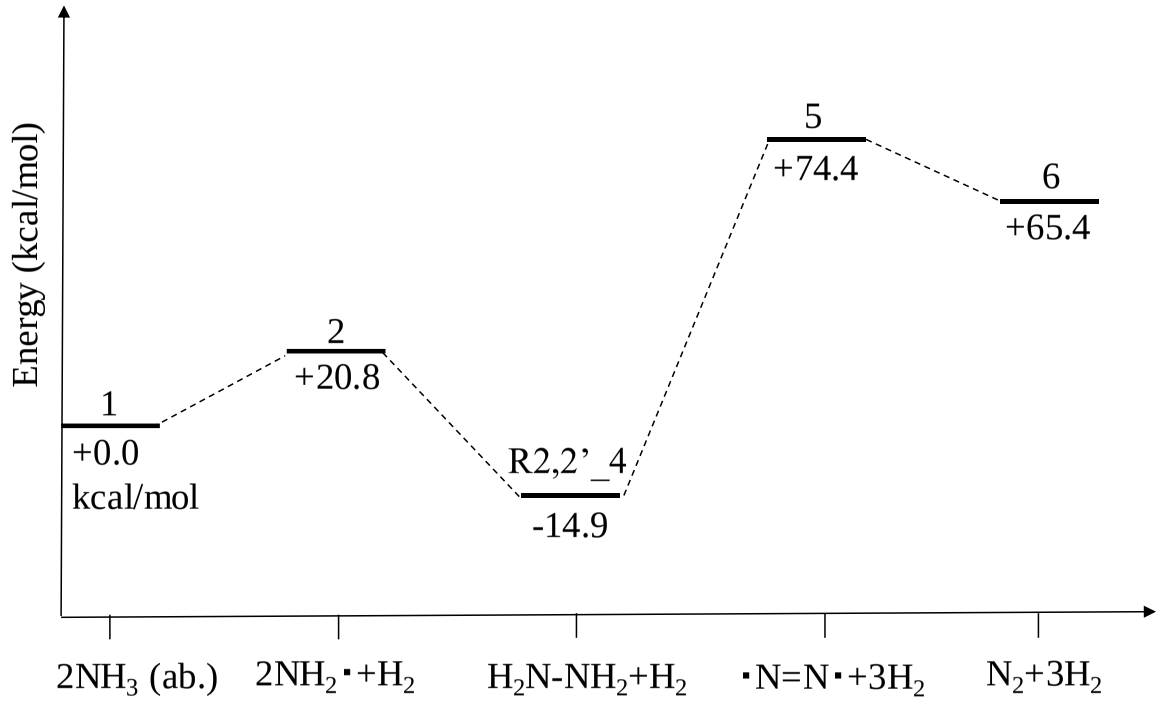

Figure 7. Energy diagram for the NH_3 decomposition to N_2 and H_2 in pathway route 2 over TiO_2 photocatalyst.

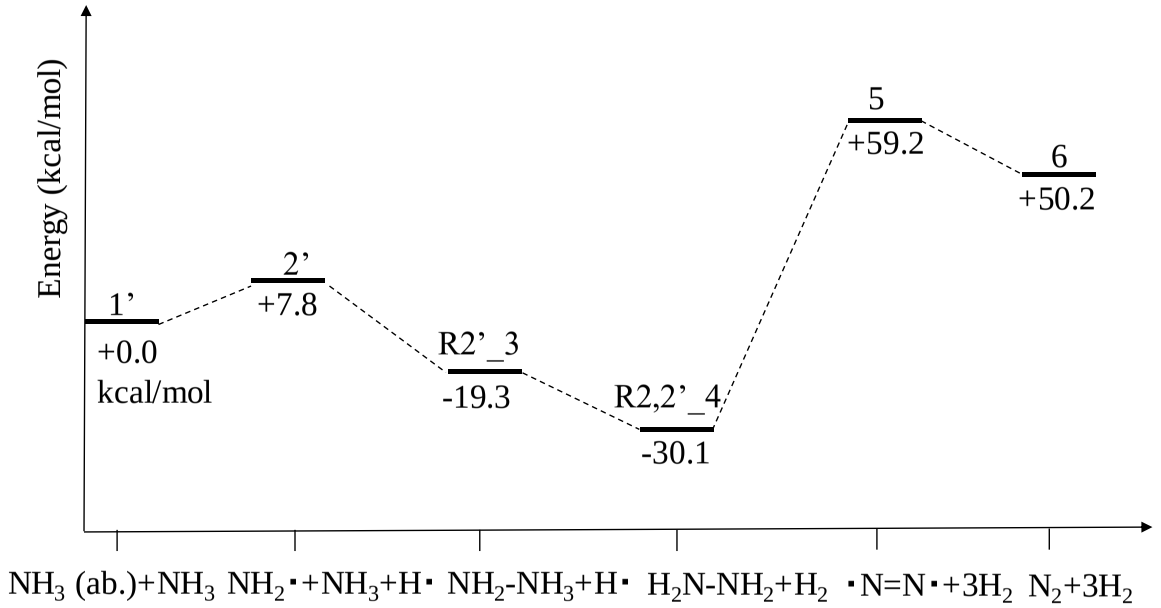

Figure 8. Energy diagram for the NH_3 decomposition to N_2 and H_2in pathway route 2’ over TiO_2 photocatalyst.

route 2 and route 2'. The remarkably improved photocatalytic performance should be ascribed to the existence of Ni^0 and it is seemed that Ni^0 enhances the reaction pathways via H_2N-NH_2 as an intermediate.

4.3.4. Conclusion

Ni/TiO_2 photocatalysts led to the highest activity among various metal-loaded photocatalysts on the NH_3 decomposition to N_2 and H_2. From ESR measurements, it was indicated that a NH_2 radical formed as an intermediate. To investigate the mechanism of the NH_3 decomposition, the two reaction pathways in which N_2 and H_2 formed through a NH_2 radical were considered : the formation of the NH radicals through extraction of each hydrogen atom from the two NH_2 radicals (route 1) or the formation of NH_2-NH_2 by the coupling of adjacent NH_2 radical (route 2). The activation energies in route 1 and route 2 were computed. The activation energies were estimated to be 236 kcal/mol, 74.8 kcal/mol respectively. It was found that route 2 was more favorable pathway than route 1. Reaction pathways in which N_2 and H_2 formed through NH_2-NH_2 were considered; route 2 or the formation of H_2N-NH_2 by reacting with one NH_2 radical and ammonia in the gas phase (route 2'). The activation energies were estimated to be 74.4 kcal/mol, 59.2 kcal/mol respectively. The activation energies in route 2 and route 2' were not significantly different, there was a possibility that the NH_3 decomposition proceeded in both route 2 and route

2' via the formation of NH_2-NH_2. Ni^0 might enhance the reaction pathways via H_2N-NH_2 because Ni^0 existed in the catalyst having a high catalytic activity. Our findings can serve as a reference for other similar photodecomposition reaction, which might open a new avenue to the design of more efficient catalytic systems.

References

1. J. Wang, P. Rao, W. An, J. Xu, Y. Men, *Appl. Catal., B: Environ.*, 195 (2016) 141–148.
2. A. F. Alkaim, T. A. Kandiel, F. H. Hussein, R. Dillert, D. W. Bahnemann, *Appl. Catal. A: Gen.*, 466 (2013) 32–37.
3. V. A. Ogarev, V. M. Rudoi, O. V. Dement'eva, *Russ. J. Physic. Chem. A*, 88 (2014) 181–191.
4. H. Yu, X. Huang, P. Wang, J. Yu, *J. Phys. Chem.*, 120 (2016) 3722–3730.
5. B. S. Huang, M. Y. Wey, *J. Nanopart. Res.* 16 (2014) 2178.
6. A. Cruz-López, A. C. L. Pozos, S. I. S. Vázqueza, R. Zanella, R. Gómez, *Mater. Res. Bull.*, 83 (2016) 603–608.
7. M. Reli, M. Edelmannov, M. Sihor, Petr Praus, L. Svoboda, K. K. Mamulova, H. Otoupalíkova, L. Capek, A. Hospodkova, L. Obalova, K. Kocí, *Int. J. Hydrog. Energy*, 37 (2012) 8530–8538.
8. N. Itoh, A. Oshima, E. Suga, T. Sato, *Catal. Today*, 236 (2014) 70–76.
9. A. Klerke, S. K. Klitgaard, R. Fehrmann, *Catal. Lett.*, 130 (2009) 541–

546.

10. K. Obata, K. Kishishita, A. Okemoto, K. Taniya, Y. Ichihashi, S. Nishiyama, *Appl. Catal., B: Environ.*, 160-161 (2014) 200–203.
11. R. Pol, M. Guerrero, E. García-Lecina, A. Altube, E. Rossinyol, S. Garroni, M. D. Baró, J. Pons, J. Sort, E. Pellicer, *Appl. Catal. B: Environ.*, 181 (2016) 270–278.
12. K. Siwinska-Stefanska, B. Kurc, *J. Power Sources*, 299 (2015) 286–292.
13. Y. T. Lin, C. H. Weng, H. J. Hsu, Y. H. Lin, C. C. Shiesh, *Int. J. Photoenergy*, (2013) 1–13.
14. L. Yang, M. Gao, B. Dai, X. Guo, Z. Liu, B. Peng, *Appl. Surf. Sci.*, 386 (2016) 337–344.
15. Y. Zou, S. Z. Kang, X. Li, L. Qin, J. Mu, *Int. J. Hydrog. Energy*, 39 (2014) 15403–15410.
16. Y. Luan, L. Jing, M. Xie, X. Shi, X. Fan, Y. Cao, Y. Feng, *Phys. Chem. Chem. Phys.,* 14 (2012) 1352–1359.
17. D. Ponnusamy, S. Madanagurusamy, *J. Electron. Mater.*, 44 (2015) 4726 ─4733.
18. M. Zalfani, B. Schueren, M. Mahdouani, R. Bourguiga, W. B. Yu, M. Wu, O. Deparis, Y. Li, B. L. Su, *Appl. Catal. B: Environ.*, 199 (2016) 187─ 198.
19. J. Nemoto, N. Gokan, H. Ueno, M. Kaneko, *J. Photochem. Photobiol. A*: *Chem.*, 185 (2007) 295─300.
20. J. Liu, B. Liu, Z. Ni, Y. Deng, C. Zhong, W. Hua, *Electr. Acta*, 150 (2014)

146─150.

21. M. Reli, N. Ambrozová, M. Sihor, L. Matejová, L. Capek, L. Obalová, Z. Matej, A. Kotarba, K. Kocí, *Appl. Catal., B: Environ.*, 178 (2015) 108 ─116.
22. S. Lin, Y. Pei, *J. Phys. Chem. C*, 118 (2014) 20346─20356.
23. G. Zhao, H. Liu, D. Zhang, X. Huang, X. Yang, *ACS Catal.*, 4 (2014) 2231─2240.
24. L. Liu, Y. Wu, T. Wang, X. Gao, J. Zhu, Y. Zhao, *J. Org. Chem.*, 79 (2014) 5074─5081
25. Z. Li, S. Chen, S. Gong, B. Feng, Z. Zhou, *Comput. Theor. Chem.*, 1088 (2016) 24–31.
26. Q. Lu, H. Yu, Y. Fu, *J. Am. Chem. Soc.*, 136 (2014) 8252─8260.
27. C. Miao, B. Wang, Y. Wang, C. Xia, Y. M. Lee, W. Nam, W. Sun, *J. Am. Chem. Soc.*, 138 (2016) 936─943.
28. V. P. Indrakanti, J. D. Kubicki, H. H. Schobert, *Energy Fuels*, 22 (2008) 2611–2618.
29. I. Onal, S. Soyer, S. Senkan, *Surf. Sci.*, 600 (2006) 2457–2469.
30. R. Wanbayor, V. Ruangpornvisuti, *J. Mol. Struct. Theochem.*, 952 (2010) 103–108.
31. V. Zunic, S. D. Skapin, D. Suvorov, *J. Am. Ceram. Soc*., 98 (2015) 2997–3005.
32. Y. Gönüllü1, A. A. Haidry, B. Saruhan, *Sens. Actuators. B*, 217 (2015)

78–87.

33. S. Ozkan, A. Mazare, P. Schmuki, *Electr. Acta*, 176 (2015) 819–826.
34. S. Sitthisa, W. An, D. E. Resasco, *J. Catal.*, 284 (2011) 90–101.
35. L. Qin, J. Xu, J. Lian, Z. Jiang, Q. Jiang, *Surf. Coat. Technol.*, 203 (2008) 142−147.
36. A. Kumara, J.T. Miller, A.S. Mukasyan, E.E. Wolf, *Appl. Catal. A: Gen.*, 467 (2013) 593−603.
37. S. Yamazoe, T. Okumura, T. Tanaka, *Catal. Today*, 120 (2007) 220−225.
38. H. Yuzawa, T. Mori, H. Itoh, H. Yoshida, *J. Phys. Chem. C*, 116 (2012) 4126−4136
39. F. Koksal, O. Cakir, İ. Gumrukcu, M. Birey, *Z. Naturforsch. A*, 40 (1985) 903−905
40. S. Kim, J. W. Ginsbach, J. Y. Lee, R. L. Peterson, J. J. Liu, M. A. Siegler, A. A. Sarjeant, E. I. Solomon, K. D. Karlin, *J. Am. Chem. Soc.*, 137 (2015) 2867−2874.

Chapter 4.4. Photocatalytic Decomposition of Water with Urea as a Reducing Agent for Wastewater Utilisation

4.4.1. Introduction

Currently, the rapidly increasing environmental pollution caused by the dependence on petroleum energy sources is a serious issue worldwide, attributed to the high consumption of petroleum resources and harmful chemicals released into the environment. Thus, for several decades, sustainable chemical processes, as well as environment-friendly energy sources, have been desired in industry [1-9]. In particular, hydrogen has attracted considerable attention as a promising energy carrier for a future low-carbon economy, which is used not only in electrochemical cells, but also as a fuel in internal engines [10-17]. The utilisation of hydrogen as an electrical energy carrier is actually limited because the current production of hydrogen from hydrocarbons requires a large amount of energy, as well as results in carbon dioxide evolution [18-20]. Therefore, it is imperative to develop green hydrogen production processes for realising a sustainable chemical society, where renewable sources of energy, such as solar energy, can be exploited.

Photocatalytic technology based on semiconductors has attracted

considerable attention in the fields of solar energy utilisation and environmental remediation. Several studies have been reported on the development of new semiconductors and their applications in photocatalysis, such as for the photodecomposition and removal of harmful chemical compounds [21-23], photosynthesis of chemical substances [24-26], and photodecomposition of water into hydrogen and oxygen [27,28]. In particular, the production of hydrogen via the photodecomposition of water is an active research area in photocatalysis, which typically utilises reducing agents. However, the use of reducing agents originating from petroleum resources only marginally contributes to savings with respect to the consumption of petroleum resources and emissions of carbon dioxide. Urea is expected to be used as a reducing agent for the photocatalytic production of hydrogen as it is a non-toxic organic compound and abundant in domestic wastewater. For photocatalysis, titanium dioxide (TiO_2) is typically used because of its wide range of applications, such as water decomposition, and chemical stability. However, its photocatalytic efficiency is quite low under visible light, which accounts for nearly half of the solar energy incident on the Earth's surface received from the sun [28]. Some researchers have reported the doping of TiO_2 with various cations for the improvement of photocatalytic efficiency [29–31]. To improve photocatalytic efficiency, it is highly important to design light absorption property of photocatalysts. This study reported the photocatalytic performance of two types of photocatalysts that are a Ta^{5+} and Cr^{3+} co-doped TiO_2 inorganic semiconductor and a metal-free picene organic

semiconductor. A Cr^{3+} single-doped TiO_2 has been reported [32], however, single-doping of Cr^{3+} ion often leads to formation of Cr^{6+} and decrease in photocatalytic efficiency. Addition of pentavalent metal ion into doped TiO_2 is expected to be high performance photocatalyst by charge compensation [33]. In this study, I selected tantalum (V) as a doped metal ion that is chemical stable. Co-doping with Ta^{5+} and Cr^{3+} possibly results in the narrowing of the band gap via the formation of new impurity levels between the conduction and valence bands, which in turn inhibits the rapid recombination of electron–hole pairs. Furthermore, I also developed a picene thin film photocatalyst as noble metal-free photocatalyst. Utilisation of organic materials is a new developing challenge in in the field of photocatalysis [34]. Picene has an optical gap of 3.2 eV close to the energy level of typical inorganic semiconductors, such as TiO_2 which is required for the decomposition of water. It is therefore expected to be an effective photocatalyst for hydrogen production from water. The photocatalytic performance of co-doped Ta^{5+} and Cr^{3+} TiO_2 and picene thin film photocatalysts were estimated by photocatalytic decomposition of water with urea. The decomposition product from urea, which has not been clarified thus far, was also investigated. This paper described the possibility of using urea as a non-petroleum reducing agent for the photodecomposition of water over various photocatalysts including inorganic semiconductors based on TiO_2 and organic semiconductors. The obtained catalysts were characterised by X-ray diffraction (XRD), X-ray photoelectron spectroscopy (XPS), and ultraviolet–visible (UV–Vis)

spectroscopy.

4.4.2. Experimental

4.4.2.1. Preparation of metal-modified TiO_2 photocatalysts

All materials were used as received. $NiNO_3 \cdot 6H_2O$, $AgNO_3$, $Cu(NO_3)_2 \cdot 3H_2O$, Ta_2O_5, and Cr_2O_3 were commercially obtained from Nacalai Tesque. H_2PtCl_6 was purchased from Tanaka Kikinzoku Kogyo. Metal-modified TiO_2 photocatalysts (M/TiO_2, M: dopant, Ni, Cu, Pt, and Ag) were fabricated by impregnation. In a typical process, 1.0 g of TiO_2 (JRC-TIO-11, Japan Reference Catalyst) and a metal precursor were completely dispersed in 50 mL of water, followed by evaporated to dryness in a water bath at 363 K. The obtained mixture was dried overnight in vacuum, calcined at 723 K for 5 h in air, followed by reduction under hydrogen for another 3 h. The solid thus obtained was referred to as M/TiO_2 (M: Ni, Cu, Pt, or Ag).

4.4.2.2. Preparation of TiO_2 photocatalysts co-doped with Ta and Cr

Doping of TiO_2 with Ta and Cr was performed by a simple solid reaction method. Ta_2O_5 and Cr_2O_3 were added to TiO_2, and the mixture was completely mixed. The powder was calcined at 1423 K for 10 h. The

solid thus obtained was designated Ta(x)-Cr(y)-TiO_2, where x and y represent the mol% of Ta and Cr dopants, respectively. Modification of Ta(x)-Cr(y)-TiO_2 with Ni was carried out by the method previously described in Section 2.1.1.

4.4.2.3. Preparation of picene thin-film photocatalysts

Picene can be used as the photocatalyst because its energy level is similar to the redox potential required for the decomposition of water into hydrogen. Picene powder, which was purified by sublimation, was obtained from NARD Institute, Ltd., Japan. A picene thin-film photocatalyst with film thickness of 300 nm was prepared by thermal vacuum evaporation using a SANYU SVC-700TM vacuum system. Quartz glass used as a film substrate were cut to the predetermined length and thickness (substrate size; 10 mm × 40 mm × 0.5 mm). The prepared catalysts were designated as Picene/SiO_2.

4.4.2.4. Catalyst test

A catalyst (20 mg) and 5 mL of an aqueous solution of urea (0.3 mol/L) were added into a quartz-glass batch reactor. The reactor was charged with Ar for completely removing air. The reaction mixture was stirred and irradiated using a 300-W Xe lamp equipped with a colour filter (Hoya UV-25) for 3 h. The gaseous products were analysed by gas chromatography

(Shimadzu GC-8A, Japan) equipped with a thermal conductivity detector (TCD) using Ar as the carrier gas. The products in the reaction were analysed using D_2O instead of H_2O as the reactant with a quadrupole mass spectrometer.

4.4.2.5. Characterisation

The structures of the TiO_2 photocatalysts were characterised by XRD with CuKα radiation (Rigaku RINT-2100). Diffuse-reflectance spectra were recorded on a UV–Vis diffuse-reflectance (UV–Vis-DR) spectrometer (Hitachi U-3210D), and data were converted from reflectance to absorbance by the Kubelka–Munk method. XPS spectra were recorded at room temperature on an ESCA-3400 (Shimadzu, Japan) electron spectrometer equipped with a Mg Kα (1253.6 eV) line of the X-ray source. Photoluminescence spectra were recorded on an F-7000 fluorescence spectrophotometer (Hitachi) equipped with a Xe lamp as the excitation light source at 73 K in vacuum. Fluorescence was generated by continuous-wave near-UV excitation at 280 nm.

4.4.3. Results and discussion

4.4.3.1. Photocatalytic formation of hydrogen from water with urea over various catalysts

The photocatalytic production of hydrogen was performed over various semiconductor materials via the photodecomposition of water using urea as the non-petroleum-derived reducing agent under light irradiation, and Table 1 shows the results. The photocatalytic activities of Ni/TiO_2 and Pt/TiO_2 (Entry 2 and 5) for the formation of hydrogen are superior to those of pure TiO_2, Cu/TiO_2, and Ag/TiO_2. Hence, Ni/TiO_2 is used as the standard photocatalyst for the decomposition of water with urea as it is more cost-effective than Pt/TiO_2. The optimum amount of Ni loading and reduction temperature for catalyst preparation were determined to be 1.0 wt% and 723 K, respectively (Figures S1, S2, and S3 in the Supporting Information). A low-molecular-weight organic semiconductor, such as picene, exhibits light absorption similar to the band gap of a typical inorganic photocatalyst [34-37]. As shown in the UV–Vis absorption spectra in Figure 1, the absorption peak of the picene thin-film sample is observed in the 250–400 nm region, as well as that of Ni/TiO_2. The absorption edge of the sample is 383 nm, and the optical gap is calculated to be 3.2 eV [34]. The lowest energy peak at 383 nm is attributed to the $S_0 \rightarrow S_1$ transition, corresponding to a single HOMO–LUMO excitation; this result is in agreement with a previously reported spectrum [38]. The optical gap is almost similar to that of typical

Table 1. Yield of hydrogen in the photocatalytic decomposition of water with urea over pure TiO_2, M/TiO_2 (M = Ni, Cu, Pt, Ag), and Picene/SiO_2.

Entry	Catalysts	Reactants	Hydrogen production (μmol)
1	TiO_2 [a]	water and urea	2
2	Ni/TiO_2 [a]	water and urea	69
3	Ni/TiO_2 [a]	water	0
4	Cu/TiO_2 [a]	water and urea	15
5	Pt/TiO_2 [a]	water and urea	57
6	Ag/TiO_2 [a]	water and urea	12
7	Picene/SiO_2 [b]	water and urea	16
8	Picene/SiO_2 [b]	water	0

Reaction conditions

Reactant: 5 mL of aqueous urea solution (0.3 mol/L)

Light source: >250 nm

Reaction time: 3 h

Reaction temperature: room temperature

[a] Catalysts: M/TiO_2 (M = Ni, Cu, Pt, Ag; Metal loading 1.0 wt%)

Pretreatment: Reduction with H_2 at 723 K

Yield of hydrogen was determined as amount of hydrogen per catalyst weight (μmol/g-cat).

[b] Catalysts: Picene/SiO_2 with film thickness of 300 nm

Yield of hydrogen was determined as amount of hydrogen per light irradiation area (μmol/m^2-cat).

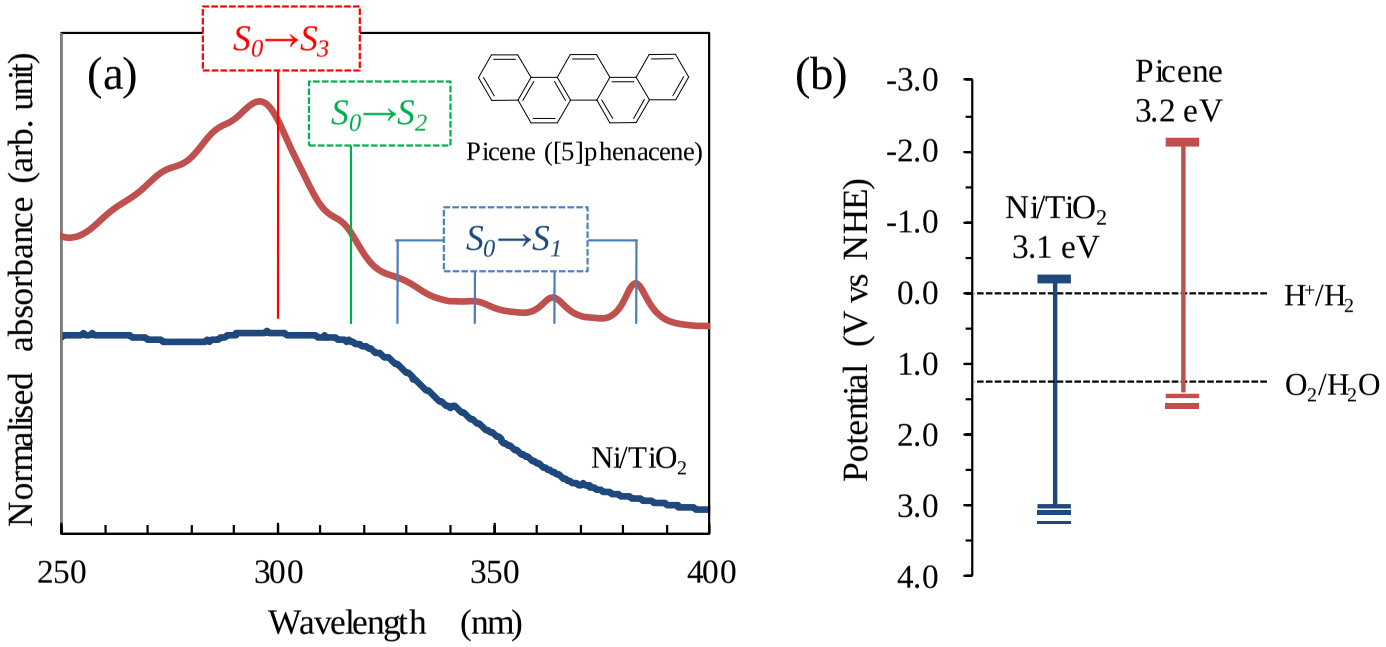

Figure 1. UV-Vis absorption spectrum (a) and energy level diagram (a) of Ni/TiO_2 and Picene/SiO_2.

TiO_2 photocatalysts. Thus, picene thin-film catalyst was also used for the photocatalytic decomposition of water with urea. Picene/SiO_2 exhibits the good activity with the hydrogen formation of 16 μmol/m^2-cat in the presence of urea (Entry 7). Although the observed activity is satisfactory, organic semiconductors demonstrate potential for photocatalytic chemistry by the tuning of molecular design and film deposition strategies. Utilisation of urea efficiently enhances hydrogen production from water photodecomposition catalysed by various catalysts including inorganic semiconductors based on TiO_2 and organic semiconductors based on picene thin-films.

4.4.3.2. Identification of decomposition products via the photocatalysis of water and urea

Figure 2 shows the yield of hydrogen obtained using Ni/TiO_2 with and without light irradiation. Hydrogen is not observed under dark condition, while hydrogen is produced under light irradiation, with no catalyst deactivation. The photocatalytic evolution of hydrogen is clearly observed, and no noticeable degradation of activity is confirmed during the reaction for at least 7 h. In addition, the reaction is performed using D_2O instead of H_2O as the reactant, and gaseous products were analysed using the quadrupole mass spectrometer (Table 2). Under all conditions, hydrogen formation is not observed; however, the formation of only heavy hydrogen is observed under light irradiation in the presence of urea. This result

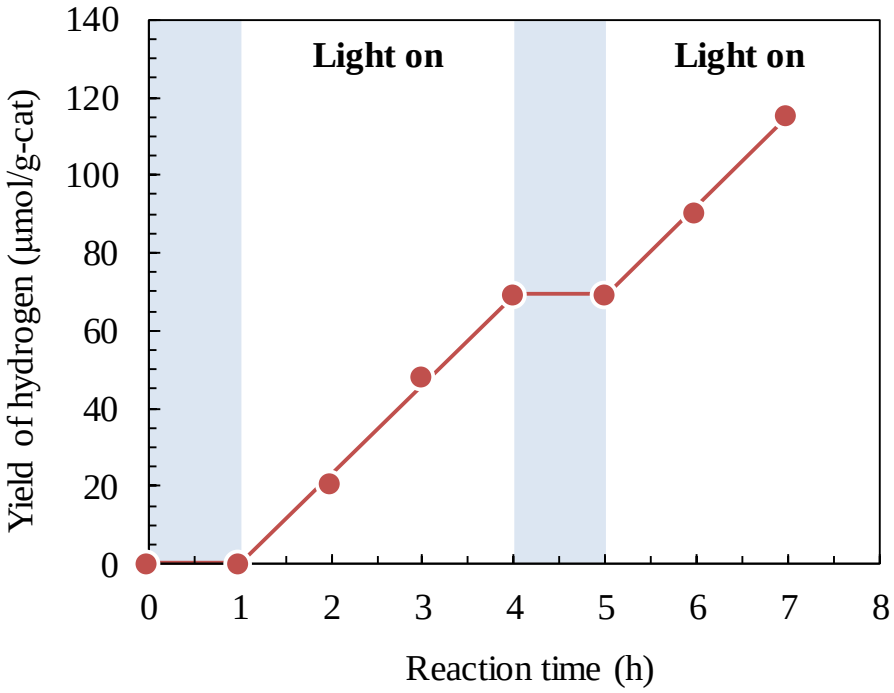

Figure 2. Time profile of hydrogen yield for the photodecomposition of water with urea over 1.0 wt% Ni/TiO_2 catalyst.

Table 2. Yield of H_2 and D_2 in the photocatalytic decomposition of heavy water under several condition over Ni/TiO_2 for 60 min.

Entry	Reactant	Light source	Yield* (μmol/g-cat)	
			H_2	D_2
1	D_2O	λ>250	0	0
2	D_2O + urea	Dark	0	0
3	D_2O + urea	λ>250	0	15

*determined by using mass spectroscopy

implies that hydrogen originates from H_2O, and this reaction represents the photocatalytic decomposition of H_2O using urea as the reducing agent [30]. As shown in Figure 3, nitrogen is also monitored as the by-product from the photodecomposition of water with urea. The result indicates that hydrogen and nitrogen are produced in a stoichiometric ratio of 3:1 from the photodecomposition of water with urea. Hence, the two nitrogen atoms of urea are thought to be converted into N_2, while the carbon atom of urea is thought to be converted into CO_2 [39,40]. However, CO_2 was hardly observed in the gas phase during the reaction by gas chromatography probably because it is almost dissolved in the reaction solution. For qualitatively evaluating CO_2 production, the change in the pH of the reaction solution during the reaction in the batch reactor was measured using a pH meter (Horiba LAQUAtwin, Japan). Changes in pH during the reaction under standard conditions were investigated, and Table 3 summarises the reaction results under alkaline conditions. In all cases, pH decreases with the progress of the reaction, and pH decreases from an initial pH of 9.2 to a pH of 7.2. CO_2 dissolved in water is widely known as the most common source of acidity by the formation of carbolic acid [41,42]. The reduction in pH of the reaction solution is attributed to the formation of carbolic acid during the reaction. Thus, the two nitrogen atoms and one carbon atom of urea are believed to be converted into N_2 and H_2CO_3, respectively, according to the following reaction (i).

$$(NH_2)_2CO + 2H_2O \xrightarrow[Ni/TiO_2]{h\nu} 3H_2 + N_2 + H_2CO_3 \qquad \text{(i)}$$

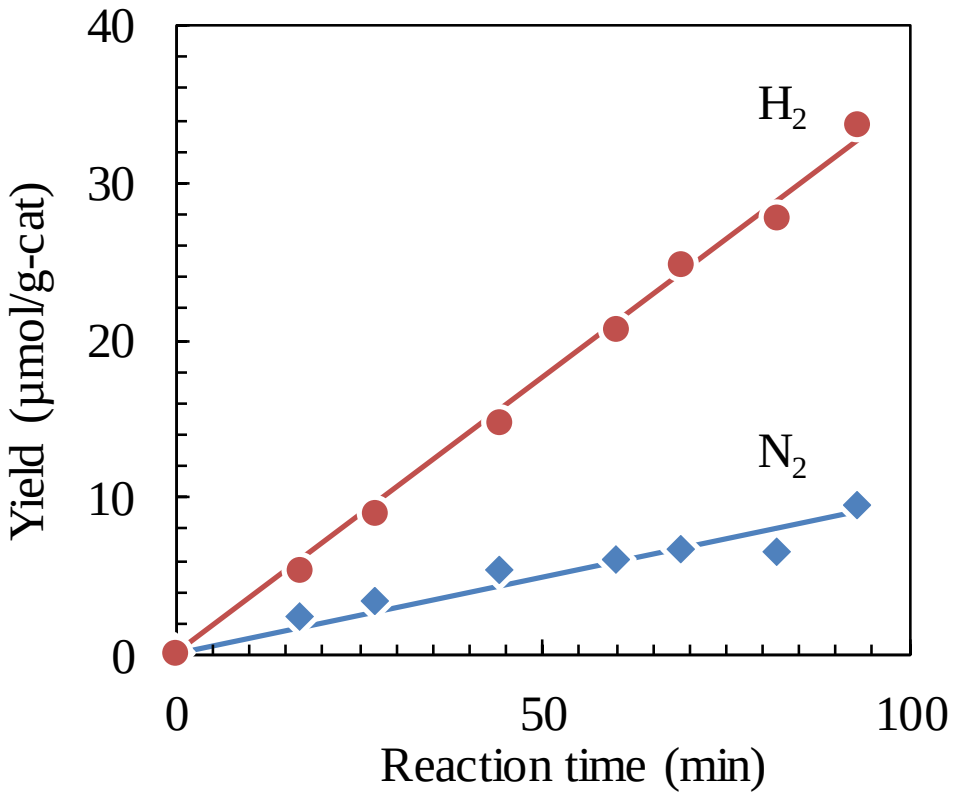

Figure 3. Yield of hydrogen and nitrogen over Ni/TiO_2 in the photocatalytic decomposition of water with urea.

Table 3. Yield of H_2 in the photocatalytic decomposition of water under several condition over Ni/TiO_2 for 2 h.

pH of the reaction solution		pH variation [b]	Yield of hydrogen [c] (μmol/g-cat)
initial	after the reaction [a]		
7.0	6.5	-0.5	60.7
9.2	7.2	-2.0	92.2
9.9	8.5	-1.4	89.9
10.8	10.1	-0.7	88.0
11.8	11.5	-0.3	89.8

[a] The pH of the aqueous urea solution including Ni/TiO_2 after UV light irradiation for 2 h.

[b] A variation in pH of the reaction solution in the photocatalytic decomposition of water with urea over Ni/TiO_2 for 2 h.

4.4.3.3. Photocatalytic activity of TiO_2 co-doped with Ta^{5+} and Cr^{3+}

The utilisation of solar energy for hydrogen generation is a challenge, attributed to insufficient visible-light power conversion. Kudo and co-workers have demonstrated that the incorporation of a transition metal, such as Cr^{3+} and Sb^{5+}, into a TiO_2 lattice results in the extension of the absorption band of TiO_2 [43]. The use of doped TiO_2 as the photocatalyst is motivated by the observation of higher catalytic activity under solar light. Hence, herein, a TiO_2 catalyst co-doped with Ta^{5+} and Cr^{3+} in a ratio of 3:2 was prepared and tested for the photodecomposition of water to hydrogen. Table 4 summarises the results obtained from the photocatalytic activity of Ni/TiO_2 with or without Ta^{5+} and Cr^{3+} dopants. Cr-doped TiO_2 exhibits extremely low activity probably caused by the formation of recombination centres (Entry 2), while co-doping with Ta^{5+} and Cr^{3+} leads to improved photocatalytic activity (Entry 3). To confirm the increased activity caused by the expansion of the absorption band, the reaction was performed under visible light irradiation (>420 nm; Entries 4–6). Ni/Ta(3)-Cr(2)-TiO_2 also exhibits higher activity than as compared to Ni/TiO_2 and Ni/Cr(2)-TiO_2 via visible-light irradiation. The addition of Ta^{5+} into Cr^{3+}-doped TiO_2 augments photocatalytic efficiency. The UV–Vis absorption spectra of these catalysts were analysed. A band extending to the visible region is observed for Ni/Ta-Cr-TiO_2 (Figure 4). Ni/Ta(3)-Cr(2)-TiO_2 exhibits excellent absorption properties in a wide visible range. Hence, Ni/Ta(3)-Cr(2)-TiO_2 efficiently catalyses the photodecomposition of water for

Table 4. Yield of hydrogen over Ni supported TiO_2 doped with Cr and Ta.

Entry	Catalyst [a]	Yield of hydrogen (μmol/g-cat)
1 [b]	Ni/TiO_2	69
2 [b]	$Ni/Cr(2)\text{-}TiO_2$	11
3 [b]	$Ni/Ta(3)\text{-}Cr(2)\text{-}TiO_2$	78
4 [c]	Ni/TiO_2	0.0
5 [c]	$Ni/Cr(2)\text{-}TiO_2$	1.4
6 [c]	$Ni/Ta(3)\text{-}Cr(2)\text{-}TiO_2$ [c]	16

*Ni Loading: 1.0 wt%

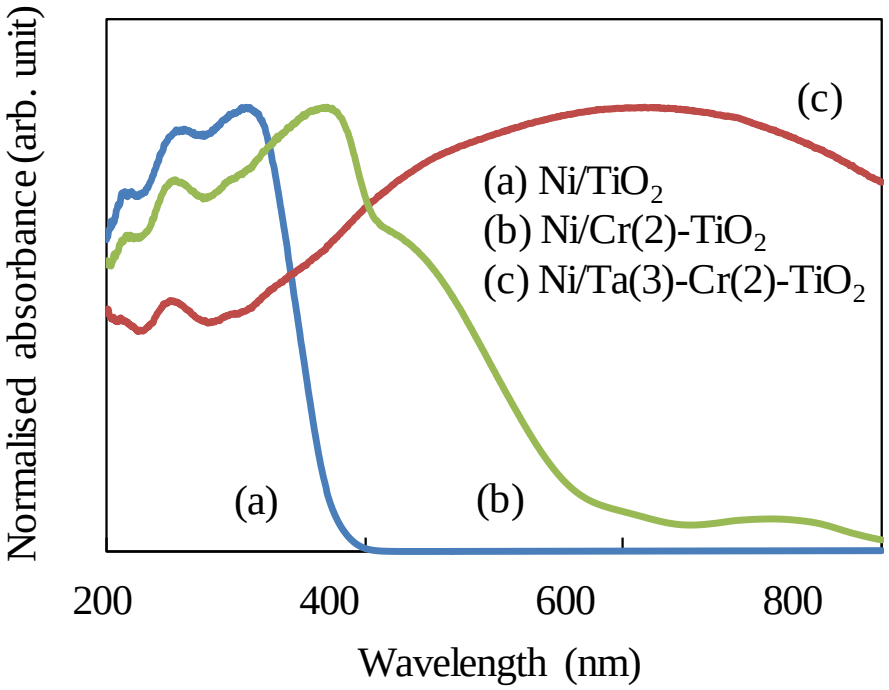

Figure 4. Diffuse reflection spectra of Ni/TiO_2 with and without Ta and Cr dopants.

hydrogen generation.

Ni/Ta(3)-Cr(2)-TiO_2 catalysts were prepared by co-doping of Ta^{5+} and Cr^{3+} into TiO_2 at different calcination temperatures (Figure 5). With increasing calcination temperature, the yield of hydrogen gradually increases, and Ni/Ta(3)-Cr(2)-TiO_2 calcined at 1473 K exhibits the highest activity. The crystal structures of the materials were analysed by XRD. All of the diffraction peaks are characteristic of rutile TiO_2 (Figure 6). High-intensity diffraction peaks observed for the sample calcined at 1423 K are attributed to the rutile phase, suggesting that high annealing temperature results in the acceleration of the crystallisation of rutile TiO_2. Ni/Ta(3)-Cr(2)-TiO_2 calcined at 1473 K exhibits high crystallinity and good activity. For optimising the atomic ratios of Ta^{5+} and Cr^{3+} co-doped into TiO_2, Ni/Ta(x)-Cr(y)-TiO_2 catalysts were prepared by co-doping at a range of Ta/Cr (0–2.0) at 1473 K and tested for the photodecomposition of water. Figure 7 shows the results obtained. Quite a low yield of hydrogen (10.8 μmol/g-cat.) is observed for Ni/Cr_2-TiO_2 doped with only Cr^{3+}, probably caused by the decrease of quantum efficiency where charge recombination is caused by the formation of Cr^{6+} as the recombination centre [43]. The additional doping of Ta into TiO_2 enhances catalytic activity. From the perspective of charge compensation with these dopants, the ideal atomic ratio of Ta/Cr in Ta(x)-Cr(y)-TiO_2 is expected to be 1.0. However, Ni/Ta(x)-Cr(y)-TiO_2 (Ta/Cr = 1.5) exhibits the best activity. Trivalent tantalum, as well as pentavalent tantalum, compounds are known to be stable [44]. The optimum atomic ratio of Ta/Cr = 1.5 is indicative of the presence of some trivalent tantalum

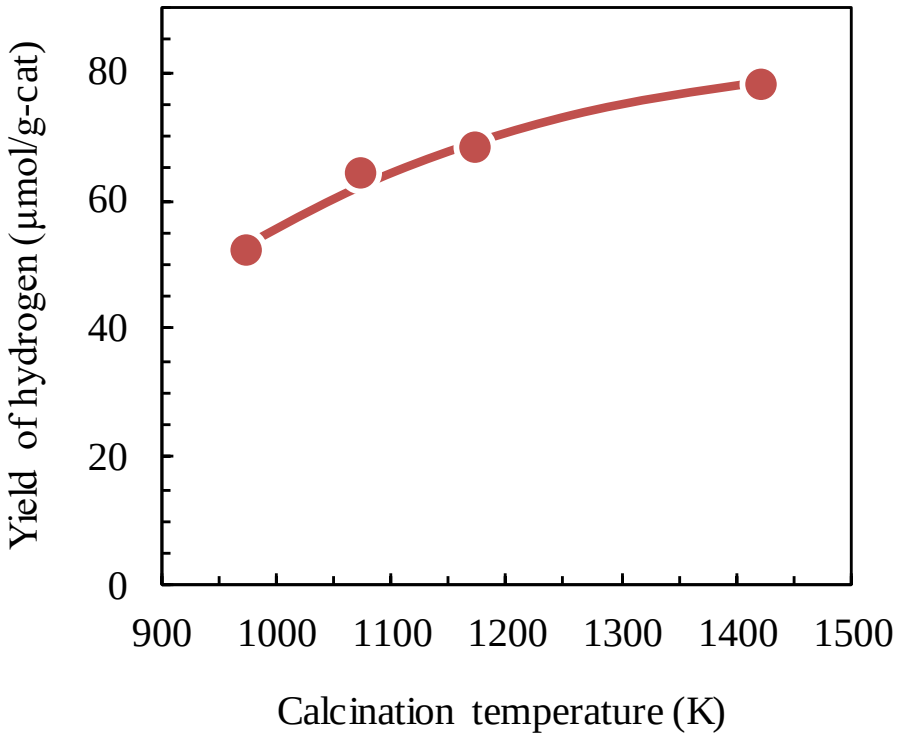

Figure 5. Yield of hydrogen over Ni/Ta(3)-Cr(2)-TiO_2 calcined at different calcination temperatures.

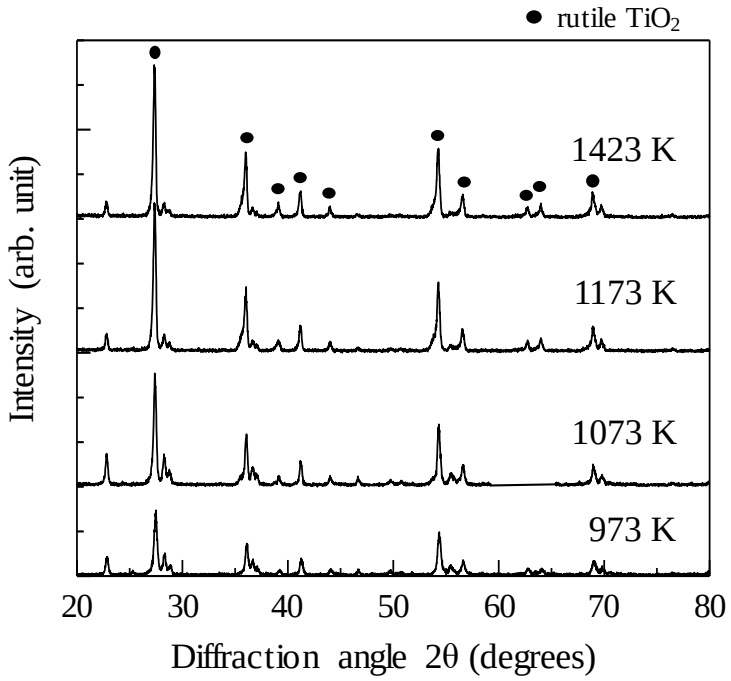

Figure 6. XRD patterns of Ta(3)-Cr(2)-TiO_2 calcined at different calcination temperatures.

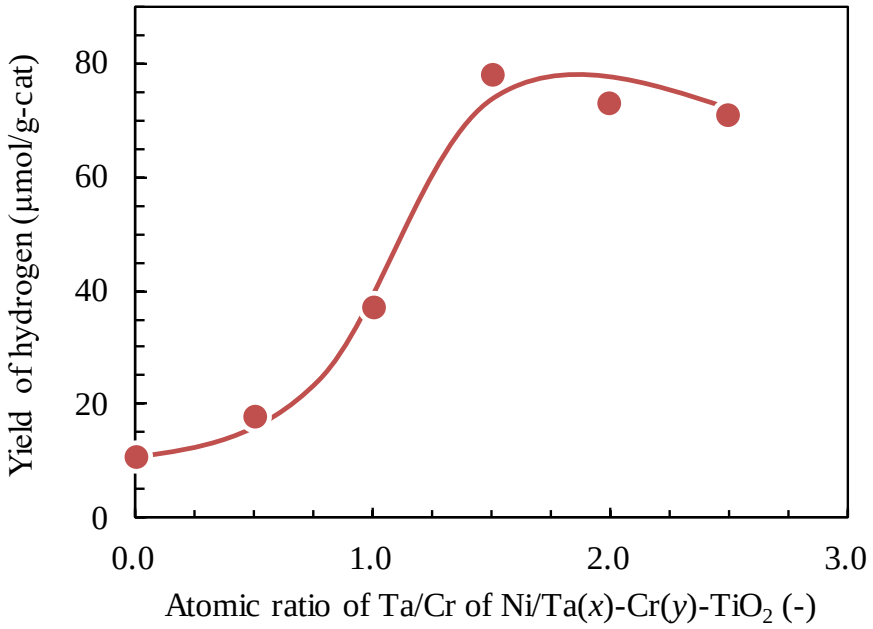

Figure 7. Yield of hydrogen via photocatalytic decomposition of water with urea by Ni/Ta(x)-Cr(y)-TiO_2 (Ta/Cr=0–2.5).

cations in the TiO_2 lattice. XRD was employed to investigate the sample structure (Figure 8). All of the diffractions peaks correspond to patterns characteristic of rutile TiO_2, indicating that the co-doped catalysts maintain the rutile crystal structure even after doping. Diffraction peaks of Ta_2O_5 are observed for Ni/Ta(x)-Cr(y)-TiO_2 (Ta/Cr = 2.0), which is doped with an excess of Ta^{5+} as compared to the stoichiometric ratio. On the basis of these results, a calcination temperature of 1473 K and a Ta/Cr atomic ratio of 1.5 were determined as optimum conditions for catalyst preparation.

4.4.4. Conclusions

Semiconductor-based photocatalysis for the production of hydrogen as a sustainable, carbon-free energy resource is one of the most attractive topics in catalyst chemistry, with considerable efforts focussed on the improvement of photocatalytic efficiency in the visible light region by solar light utilisation. In this study, the inorganic semiconductor TiO_2 doped with Ta^{5+} and Cr^{3+} and the organic semiconductor picene were used for the photocatalytic decomposition of water with urea as the sacrificial agent. Doping with Ta^{5+} and Cr^{3+} was found to extend the light absorption region and afford high activity for hydrogen production, attributed to the formation of impurity levels. TiO_2 doped with Ta^{5+} and Cr^{3+} in a ratio of 3:2 was chemically and thermally stable, exhibiting extremely good activity for the photodecomposition of water. Furthermore, the decomposition mechanism

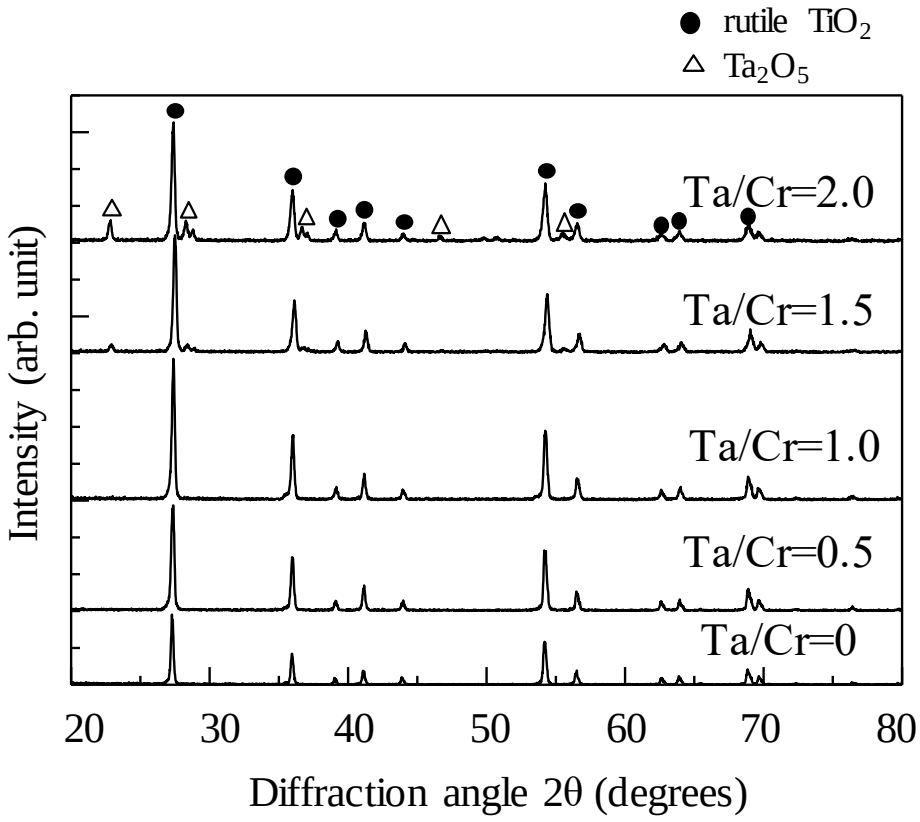

Figure 8. XRD patterns of Ta(x)-Cr(y)-TiO_2 (Ta/Cr=0–2.0) with different molar ratio of Ta/Cr.

of urea in water decomposition was investigated. Urea was found to be converted into N_2 and CO_2. This article will provide a good reference for photocatalytic production of hydrogen from water with urea as a non-petroleum promoter, that is proposed a green and sustainable process.

References

1. M. E. Himmel, S. Ding, D. K. Johnson, W. S. Adney, M. R. Nimlos, J. W. Brady, T. D. Foust, *Science*, 315 (2007) 804–807.
2. Y. Román-Leshkov, C. J. Barrett, Z. Y. Liu, J. A. Dumesic, *Nature*, 447 (2007) 982–985.
3. M. M. Alam, M. W. Murad, A. Hanifa, M. Noman, I. Ozturk, *Eco. Indic.*, 70 (2016) 466–479.
4. A. Boudghene Stambouli, *Renew. Sustain. Energy Rev.*, 15 (2011) 4507–4520.
5. J. Goldemberg, *Science*, 315 (2007) 808–810.
6. R. P. John, G.S. Anisha, K. M. Nampoothiri, A. Pandey, *Biores. Tech.*, 102 (2011) 186–193.
7. C. Zamfirescu, I. Dincer, *J. Power Sources*, 185 (2008) 459–465.
8. A. V. Shah, H. Schade, M. Vanecek, J. Meier, E. Vallat-Sauvain, N. Wyrsch, U. Kroll, C. Droz, J. Bailat, *Prog. Photovoltaic: Res. Appl.*, 12 (2004) 113–142.
9. A. Okemoto, Y. Tsukano, A. Utsunomiya, K. Taniya, Y. Ichihashi, S.

Nishiyama, *J. Mol. Catal. A: Chem.*, 411 (2016) 372–376.

10. A. Okemoto, Y. Inoue, K. Ikeda, C. Tanaka, K. Taniya, Y. Ichihashi, S. Nishiyama, *Chem. Lett.*, 43 (2014) 1734–1736.
11. S. Dunn, *Int. J. Hydro. Energy*, 27 (2002) 235–264.
12. A. Ozbilen, I. Dincer, M. A. Rosen, *Int. J. Hydro. Energy*, 36 (2011) 9514–9528.
13. T. Abbasi, S.A. Abbasi, *Renew. Sustain. Energy Rev.*, 14 (2010) 919–937.
14. Z. Xiong, C. K. Yong, G. Wu, P. Chen, W. Shaw, A. Karkamkar, T. Autrey, M. O. Jones, S. R. Johnson, P. P. Edwards, W. I. F. David, *Nat. Mater.*, 7 (2007) 138–141.
15. P. Du, R. Eisenberg, *Energy Environ. Sci.*, 5 (2012) 6012–6021.
16. L. J. Murray, M. Dincă, J. R. Long, *Chem. Soc. Rev.*, 38 (2009) 1294–1314
17. Y. Okada, E. Sasaki, E. Watanabe, S. Hyodo, H. Nishijima, *Int. J. Hydro. Energy*, 31 (2006) 1348–1356.
18. J. N. Armor, *App. Catal. A: Gen.*, 176 (1999) 159–176.
19. D. Baudouin, U. Rodemerck, F.Krumeich, A. Mallmann, K. C. Szeto, H. Ménard, L. Veyre, J. Candy, P. B. Webb, C. Thieuleux, C. Copéret, *J. Catal.*, 297 (2013) 27–34.
20. K. Jabbour, N. El Hassan, A. Davidson, P. Massiani, S. Casale, *Chem. Eng. J.*, 264 (2015) 351–358.
21. U. I. Gaya, A. H. Abdullah, *J. Photochem. Photobiol. C-Photochem. Rev.*, 9 (2008) 1–12.
22. M. N. Chong, B. Jin, C. W.K. Chow, C. Saint, *Water Res.*, 44 (2010)

2997–3027.

23. T. Maggos, J.G. Bartzis, P. Leva, D. Kotzias, *Appl. Phys. A*, 89 (2007) 81–84.
24. K. Shimizu, T. Kaneko, T. Fujishima, T. Kodama, H. Yoshida, Y. Kitayama, *App. Catal. A: Gen.*, 225 (2002) 185–191.
25. F.J. López-Tenllado, S. Murcia-López, D.M. Gómezc, A. Marinas, J.M. Marinas, F.J. Urbano, J.A. Navío, M.C. Hidalgo, J.M. Gatica, *Appl. Catal. A: Gen.*, 505 (2015) 375–381.
26. H. Yamashita, Y. Fujii, Y. Ichihashi, S. G. Zhang, K. Ikeue, D. R. Park, K. Koyano, T. Tatsumi, M. Anpo, *Catal. Today*, 45 (1998) 221–227.
27. J. Liu, Y. Liu, N. Liu, Y. Han, X. Zhang, H. Huang, Y. Lifshitz, S. Lee, J. Zhong, Z. Kang, *Science*, 347 (2015) 970–974.
28. R. Abe, *J. Photochem. Photobiol. C-Photochem. Rev.*, 11 (2010) 179–209.
29. R. Asahi, T. Morikawa, T. Ohwaki, K. Aoki, Y. Taga, *Science*, 293 (2001) 269–271.
30. K. Obata, K. Kishishita, A. Okemoto, K. Taniya, Y. Ichihashi, S. Nishiyama, *Appl. Catal. B: Environ.*, 160–161 (2014) 200–203.
31. A. Di Paola, E. García-López, S. Ikeda, G. Marcì, B. Ohtani, L. Palmisano, *Catal. Today*, 75 (2002) 87–93.
32. J. Zhu, Z. Deng, F. Chen, J. Zhang, H. Chen, M. Anpo, J. Huang, L. Zhang, *Appl. Catal. B: Environ.*, 62 3–4 (2006) 329–335.
33. A.M. Bakhshayesh, N. Bakhshayesh, *J. Coll. Int. Sci.*, 460 (2015) 18-28.
34. K. Nagai, T. Abe, Y. Kaneyasu, Y. Yasuda, I. Kimishima, T. Iyoda, H.

Imaya, *Chem. Sus. Chem.*, 4 (2011) 727–730.

35. S. R. Forrest, *Nature*, 428 (2004) 911–918.
36. A. Okemoto, K. Kishishita, S. Maeda, S. Gohda, M. Misaki, Y. Koshiba, K. Ishida, T. Horie, K. Taniya, Y. Ichihashi, S. Nishiyama, *Appl. Catal. B: Environ.*, 192 (2016) 88–92.
37. Y. Kubozono, X. He, S. Hamao, K. Teranishi, H. Goto, R. Eguchi, T. Kambe, S. Gohda, Y. Nishihara, *Eur. J. Inorg. Chem.*, (2014) 3806–3819.
38. S. Fanetti, M. Citroni, R. Bini, L. Malavasi, G. A. Artioli, P. Postorino, *J. Chem. Phys.* 137 (2012) 224506-1–224506-7.
39. L-C. Pop, I. Tantis, P. Lianos, *Int. J. Hydro. Energy*, 40 (2015) 8304–8310.
40. E. Urbańczyk, M. Sowa, W. Simka, *J. Appl. Electrochem.*, 46 (2016) 1011–1029.
41. L. Garcia-Gonzalez, H. Teichert, A.H. Geeraerd, K. Elst, L. Van Ginneken, J.F. Van Impe, R.F. Vogel, F. Devlieghere, *J. Supercrit. Fluids*, 55 (2010) 77–85.
42. C. Neal, W.A. House, K. Down, *Sci. Total Environ.*, 210–211 (1998) 173–185.
43. H. Kato, A. Kudo, *Phys. Chem. B*, 106 (2002) 5029–5034.
44. F. A. Cotton, C. A. Murillo, X. Wang, *Inorg. Chim. Acta*, 245 (1996) 115–118.

Chapter 4.5. Photodecomposition of Water Catalysed by Picene Organic Semiconductors

4.5.1. Introduction

Hydrogen has attracted attention as a potential environmentally clean energy fuel, as it can help in overcoming the side effects of greenhouse gas emission and realising a sustainable society [1-3]. In this regard, photocatalytic routes to hydrogen production, in particular the photodecomposition of water, have been the topic of extensive research [4-7]. Many researchers have reported photocatalytic reactions over inorganic semiconductors, with particular focus on enhancing their photocatalytic activity towards the water decomposition reaction. Sacrificial organic electron donors such as alcohols, organic acids, and hydrocarbons have often been employed as hole scavengers to enhance the efficiency of the photodecomposition of water [8-11]. To date, however, most of the photocatalysts used till date for the aforementioned reaction, however, are inorganic semiconductors with or without sacrificial agents or additives. Inorganic semiconductors are disadvantageous in that they require a high-temperature annealing step to ensure high performance. Moreover, because they have their individual energy levels associated with strong crystal structures and it is hard to make the energy level changes. Although many studies on inorganic photocatalysts involve arbitrary modification of

energy levels, it is difficult to synthesise noble metal oxide materials having arbitrary energy levels. In recent years, organic semiconductors have been increasingly used in new applications and to replace inorganic semiconductors in various fields. Organic semiconductor crystals have been extensively researched because of their high purity, long-range order, and unique optical structures. Consequently, there has been rapid development in organic electronics based on these crystals (organic light emitting diodes (OLEDs), integrated photonic circuits, and photovoltaic cells), as they have advantageous over traditional silicon-based semiconductor devices [12-17]. Additionally, the unique mechanical properties of organic semiconductors allow for the fabrication of flexible electronic devices such as mobile appliances and solar cells, whose market position has been strengthened because of their high mechanical flexibility and ease of mass production [18,19]. However, applications of organic semiconductors have been limited to the field of electronics. The photocatalytic properties of organic semiconductors, which differ from those of traditional inorganic semiconductors in terms of molecular orientation, intermolecular interactions, and wavelength selectivity, have not been investigated in detail. Consequently, there are only a few reports on the use of organic semiconductors as photocatalysts [20,21].

In this study, I used a photocatalytic system featuring an organic thin-film semiconductor for hydrogen evolution from water. Picene was chosen as the organic semiconductor because its band gap is close to the energy level of typical inorganic semiconductors, such as TiO_2, which is required for the

decomposition of water, as shown in Figure 1 [22,23]. Picene thin-film catalysts were prepared by thermal evaporation under vacuum, and the photocatalytic decomposition of water was performed in the presence of several sacrificial agents to evaluate the photocatalytic performance of the picene catalysts. The reaction was also performed using picene catalysts with different film thickness to investigate the influence of the film-forming state of picene crystal on the photocatalytic performance.

4.5.2. Experimental

4.5.2.1. Catalyst preparation

Pure picene powder was obtained from NARD Institute, Ltd, Japan. Picene film was deposited on a quartz glass substrate by thermal evaporation under vacuum using a SANYU SVC-700TM system. Before deposition, the substrate (quartz size; 10 mm × 40 mm × 0.5 mm) was cleaned using acetone in an ultrasonic bath, and dried at 333 K. The substrate was then placed in the substrate holder of the deposition system, which was positioned approximately 25 cm above a molybdenum boat containing the picene powder. The holder and boat were placed in a vacuum chamber that was pumped down to a base pressure of 10^{-4} Torr by using a diffusion pump. Subsequently, the molybdenum boat was heated by electric current of ~10 A to sublime picene, and the picene film was deposited on the substrate at a

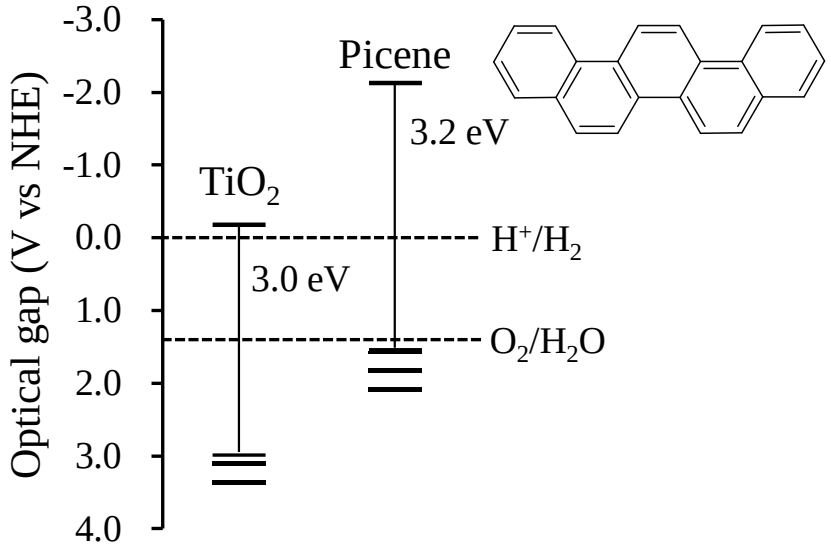

Figure 1. Energy level diagram of picene and TiO_2.

deposition rate of 0.2 nm s^{-1}.

4.5.2.2. Photocatalytic reaction for hydrogen formation from water

Water decomposition was carried out in a batch reactor system. The prepared catalyst (picene thin film/quartz; PTF/Q) and 5.0 mL aqueous urea solution (0.3 M) were placed in a 7.8 mL cylindrical quartz reactor. Dry argon gas was bubbled through the solution for 15 min to ensure complete removal of air, and then the entire reactor was purged with argon. The rector was placed at 5 cm from the window of lamp. Light irradiation was performed by using a 500W Xe lamp (USHIO, SX-UI501XQ) equipped with a 250 nm cut-off filter (HOYA UV-25) which was positioned at a distance of 1 cm from the window of the lamp. After the reaction was complete, the vapour-phase components were withdrawn by a syringe and analysed by gas chromatography (Shimadzu GC-8A) using a thermal conductivity detector (containing molecular sieve 13x column and Ar carrier).

4.5.2.3. Characterisation

The structure and crystallinity of the thin film were characterised by X-ray diffraction (XRD) using a RIGAKU RINT2100 system with Cu Kα (λ = 1.5406 Å) radiation. Standard scans were acquired from 5° to 30° (2θ) at a step size of 0.020° (2θ) and a dwell time of 1 s per step. Fine scans were acquired from 6° to 7° (2θ) at a step size of 0.002° (2θ) and a dwell time of

1 s per step. UV-visible spectra were recorded using a UV-visible absorption spectrophotometer (Hitachi U-3210D) in the region 200 to 800 nm at a step size of 1 nm. The optical gap was calculated from the absorption edge of the UV-vis absorption spectrum using the formula ΔE_{opt} (eV) = 1237.5/ λ (in nm).

4.5.3. Results and discussion

4.5.3.1. Structure of picene thin-film photocatalysts

The structural characterisation of PTF/Q of different film thickness was performed based on X-ray diffraction pattern measured at 298 K. The XRD patterns of the PTF/Q catalysts are shown in Figure 2. Diffraction lines in Figure 2 (a) ascribable to (001), (002), (003), and (004) reflections are observed, indicating highly oriented single crystal growth of the picene layer with vertical periodicity of 13.5 Å [24-26]. These diffraction patterns give an interphase distance with *c* axis length of 13.5 Å, which corresponds to the slightly tilted phase of picene crystal on a substrate. Picene clusters form a highly ordered and crystalline thin film that is nearly identical to those observed for the *c* axis in single crystals, as shown by the (00l) reflections [26]. These reflections indicate that the *a,b* planes of the grains are oriented parallel to the substrate surface. Hence, such Bragg reflections are attributed to the vertical orientation of most picene molecules on the quartz

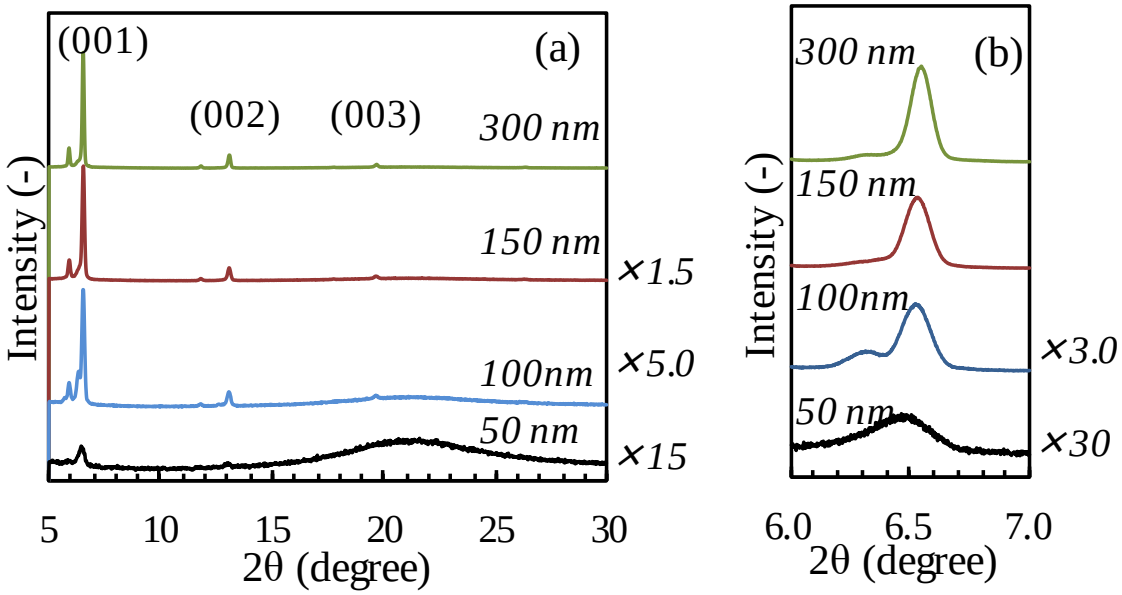

Figure 2. XRD patterns of PTF/Q of different film thickness; (a) the wide scans in the region 5.0° to 30.0°, (b) the narrow scans in the region 6.0° to 7.0°.

substrate [27] (see Figure S1 in Supporting Information). Figure 2 (b) shows the fine XRD scans in the region 6.0°–7.0°. All diffractions in Figure 2 (b) show two peaks, located at 6.30° and 6.54°, which are assigned to the vertical periodicity of 14.0 Å (Phase 1) and the slightly tilted crystalline phase of 13.5 Å (Phase 2), respectively [28]. The peak profiles were analysed using pseudo Voigt functions (see Figure S2 in Supporting Information), and an asymmetry peak was detected towards lower angles. The fitted pseudo Voigt profiles give the relative peak intensity as a parameter of non-uniformity of the crystal phase, which is a ratio calculated using the peak intensity of Phase 1 divided by that of Phase 2. The relative peak intensities of PTF/Q of different film thickness are shown in Figure 3. PTF/Q with a film thickness of 50 nm has the highest relative peak intensity, and the relative peak intensity drastically decreases as the film thickness of picene increases. An increase in the relative peak intensity indicates unevenness of the picene crystal phase due to the formation of polycrystalline picene film mixed with two phases. Thus, it is estimated that PTF/Q with the lower picene crystal thickness has a rough surface.

The UV-visible absorption spectra of PTF/Q of different film thickness are shown in Figure 4. Absorption peaks attributed to π-π* transitions of picene molecules are observed in the region 340–400 nm [29]. Although PTF/Q containing a thicker picene crystal is able to absorb a larger amount of light, film thickness has no influence on the absorption edge. The absorption edge of all samples is 383 nm, and the optical gap is calculated to be 3.2 eV by the formula ΔE_{opt} (eV) = 1237.5/λ (in nm); the calculated value

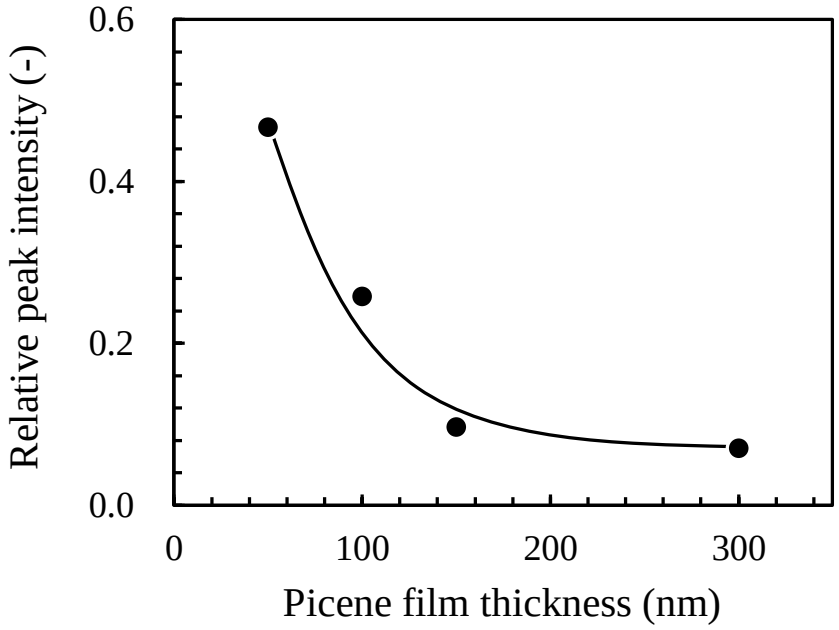

Figure 3. The relative peak intensity of PTF/Q with different film thickness of the picene film, which is calculated based on the XRD peak intensity of Phase 1 divided by that of Phase 2.

$$\textit{Relative peak intensity (-)} = \frac{\textit{Peak intensity of Phase 1}}{\textit{Peak intensity of Phase 2}}$$

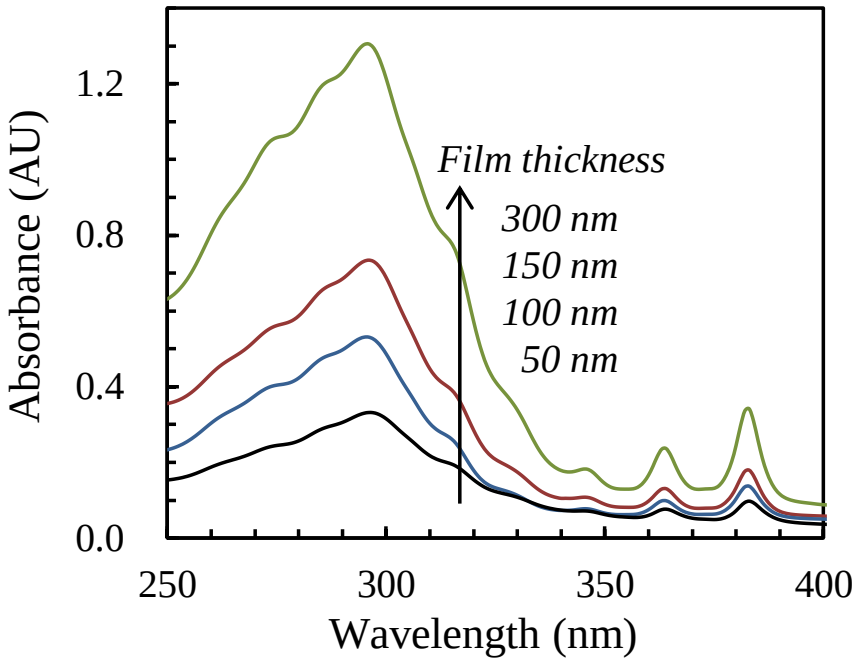

Figure 4. UV-vis absorption spectra of PTF/Q of different film thickness (50-300 nm).

is consistent with the literature data [12,30]. As this catalyst exhibits absorption over a wide range in the ultraviolet region, it is expected to work as a photocatalyst.

4.5.3.2. Photocatalytic tests

Table 1 shows the results for hydrogen production over PTF/Q with film thickness of 300 nm via the photodecomposition of water in the presence of several sacrificial agents for 8 h reaction time. Hydrogen production is not observed over a pure quartz substrate (entry 1), and without light irradiation (entry 2). These results indicate that hydrogen is not generated through the direct photodecomposition of picene or the chemical reaction of sacrificial agents on the picene film. Light irradiation onto PTF/Q in pure water leads to the slight formation of hydrogen (10 μmol/m^2, entry 3), indicating that the photocatalytic production of hydrogen from water proceeds over PTF/Q. The addition of sacrificial agents to water accelerates hydrogen production (entry 4-8), especially in the presence of formic acid, with the highest yield of hydrogen obtained as 3915.0 μmol/m^2 (entry 7). It is confirmed that sacrificial agents efficiently enhance consumption of holes. The results indicate that both PTF/Q and light irradiation are indispensable for the photodecomposition of water.

Figure 5 shows the time profile of hydrogen evolution over PTF/Q with film thickness of 300 nm. No formation of hydrogen is observed in the reaction without light irradiation; further, it is confirmed that PTF/Q does

Table 1. Hydrogen yield in the photodecomposition of water over PTF/Q (film thickness: 300 nm) in the presence of several sacrificial agents for 8 h of a reaction time.

Entry	Catalyst	Reactant	Light	Yield of hydrogen ($\mu mol/m^2$)
1	Quartz	water + urea	on	0.0
2	PTF/Q	water + urea	off	0.0
3	PTF/Q	water	on	10.0
4	PTF/Q	water + urea	on	27.0
5	PTF/Q	water + methanol	on	1084.0
6	PTF/Q	water + ethanol	on	738.0
7	PTF/Q	water + formic acid	on	3915.0
8	PTF/Q	water + lactic acid	on	604.0

Reaction conditions: Water with several sacrificial agents (4.8 mol/L), Picene thin-film catalyst on a quartz (PTF/Q), room temperature.

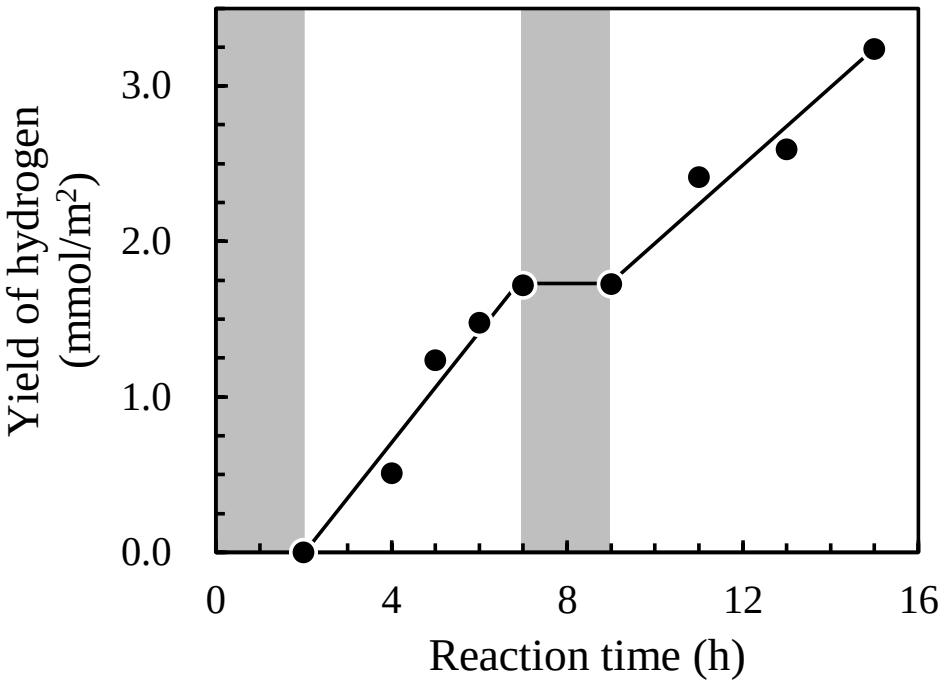

Figure 5. Hydrogen evolution from water with formic acid over PTF/Q (film thickness: 50 nm) with and without light irradiation.

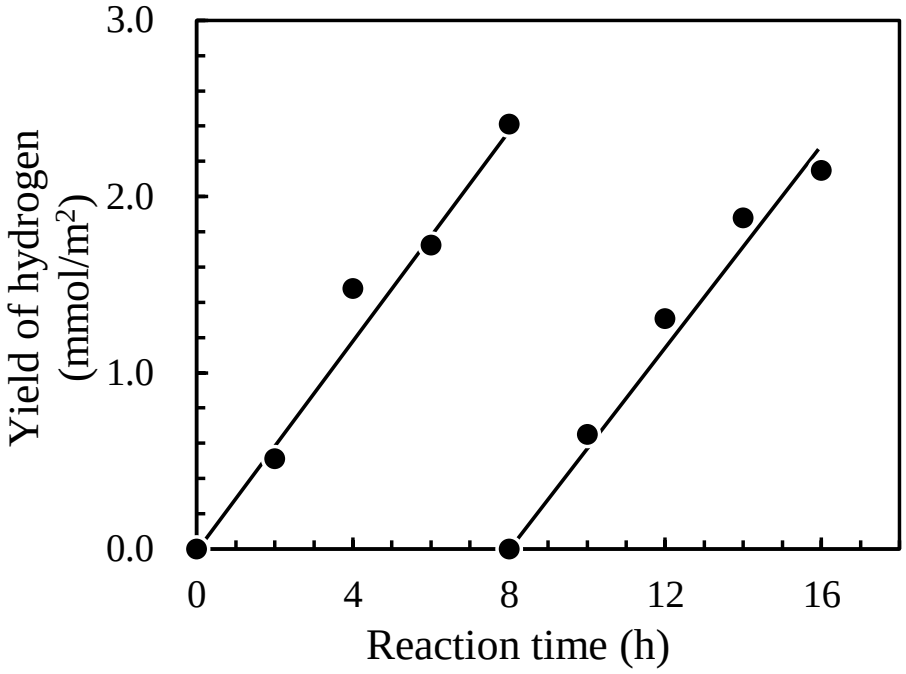

Figure 6. Repeated tests for photocatalytic hydrogen formation from water with formic acid over PTF/Q with film thickness of 50 nm.

not undergo photodegradation, because hydrogen production increases linearly with time. Moreover, repeated tests of the used PTF/Q were carried out, and the results are shown in Figure 6. The used catalyst has almost the same rate of hydrogen production as the fresh one and there is no noticeable degradation of activity after 16 h of repeated runs. The total evolution of hydrogen after 16 h is 1.82 μmol, exceeding the amount of picene on the quartz (8.84×10^{-2} μmol) used in the reaction. The reusability study shows that the catalytic performance remains almost constant under UV light irradiation for at least 16 h. After the reaction, the catalyst was characterised by XRD and UV-vis absorption spectroscopy. The results demonstrated that PTF/Q was stable throughout the reaction without any change in its structure. From the abovementioned observations, it can be concluded that the organic semiconductor consisting of a picene crystal film can effectively catalyse the photodecomposition of water to hydrogen. The photocatalytic activity of PTF/Q of different film thickness was also evaluated by the photodecomposition of water with formic acid for 10 h (see Figure 7). PTF/Q with the thinnest film (50 nm) exhibits the highest activity for hydrogen formation (2.15 mmol/m^2). A decrease in hydrogen yield was clearly observed with an increase in picene film thickness on the quartz, despite the fact that the catalysts containing thicker picene films show more efficient absorption in the UV-vis region. The excellent activity observed for PTF/Q with film thickness of 50 nm is considered to be attributed to an advantage in the crystal structure. As described above, it is suggested that PTF/Q with lower picene crystal thickness has a rough surface

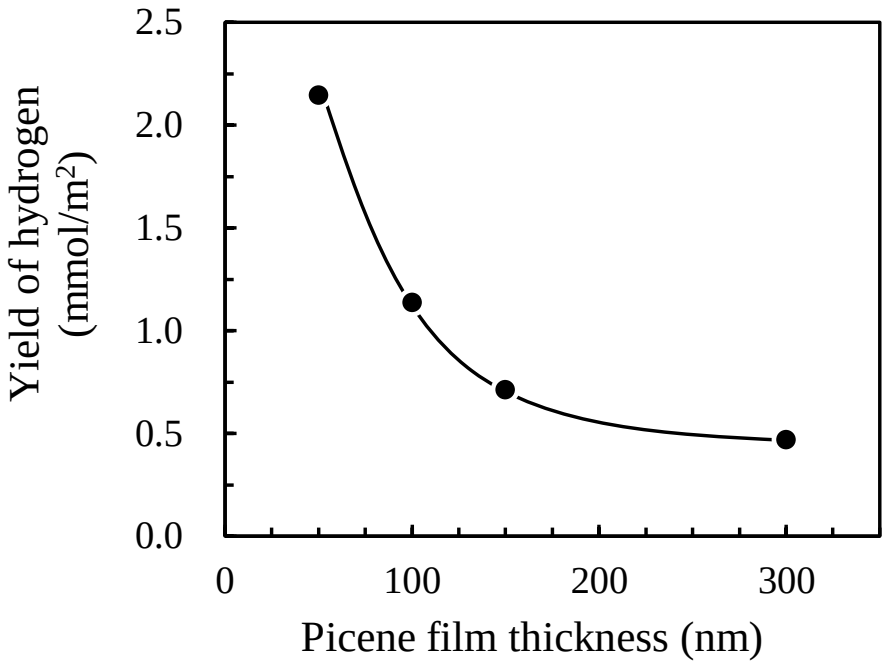

Figure 7. Hydrogen yield in the photodecomposition of water with formic acid over PTF/Q with different thickness of the picene film for 10 h of a reaction time.

since PTF/Q with film thickness of 50 nm has the highest relative peak intensity based on the XRD measurements (see Figure 3). The relationship between the hydrogen yield and relative peak intensity based on diffraction patterns is shown in Figure 8. The catalyst with the highest relative peak intensity shows the best activity (2.15 mmol/m^2), and there is a proportionally strong dependence between the hydrogen yield and relative peak intensity. A decrease in the relative peak intensity indicates that PTF/Q comprises a highly crystallised single crystal of Phase 2 and a uniform catalyst surface. A highly crystallised phase shows less activity due to a uniform surface and a smooth specific surface area. In contrast to a highly crystallised film phase, a microcrystalline grain of picene shows high activity, probably because it has a broad contact area of rough surfaces and numerous active sites. Therefore, it is suggested that the picene crystal phase of Phase 1 is the major active species and PTF/Q with a film thickness of 50 nm has a rough surface and numerous active sites, and hence, it shows excellent photocatalytic activity for hydrogen formation. The result indicates that the control of the surface morphology is very important to further improve the performance of PTF/Q in the photocatalytic process. Hence, it seems necessary to design surface morphology of films including photocatalyst components and their specific surface area, in the future.

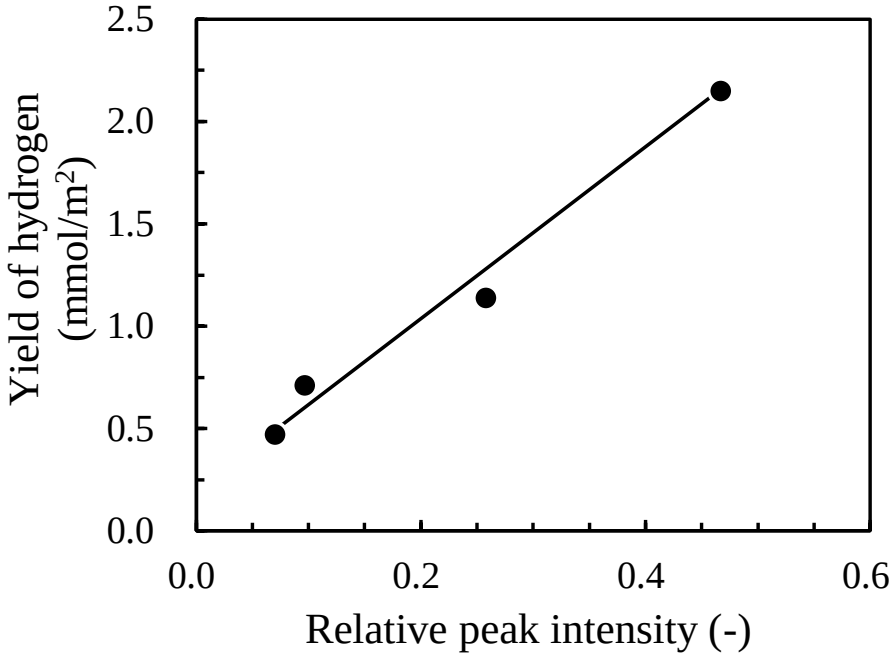

Figure 8. The dependence of hydrogen yield on the relative peak intensity based on XRD measurements.

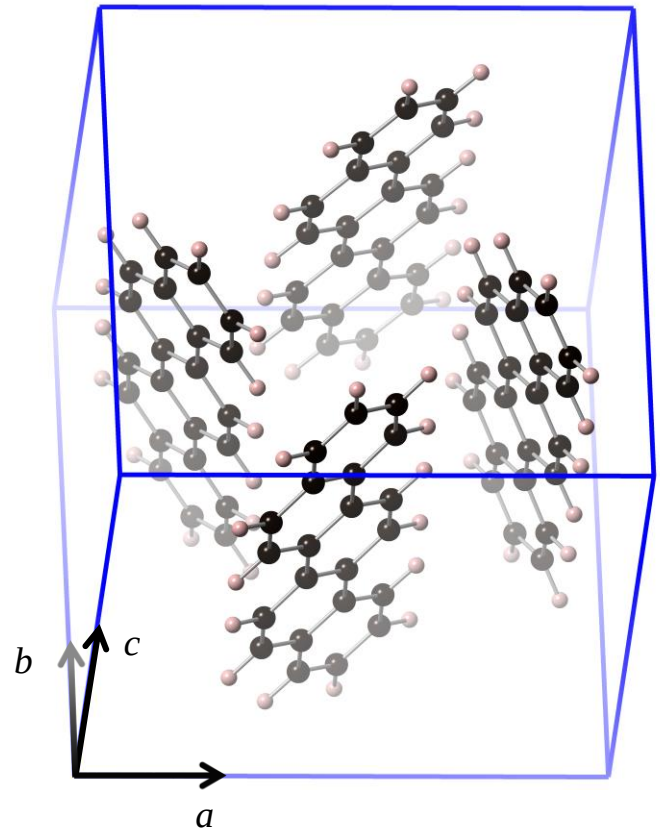

Figure S1 Lattice structure of picene on PTF/Q.

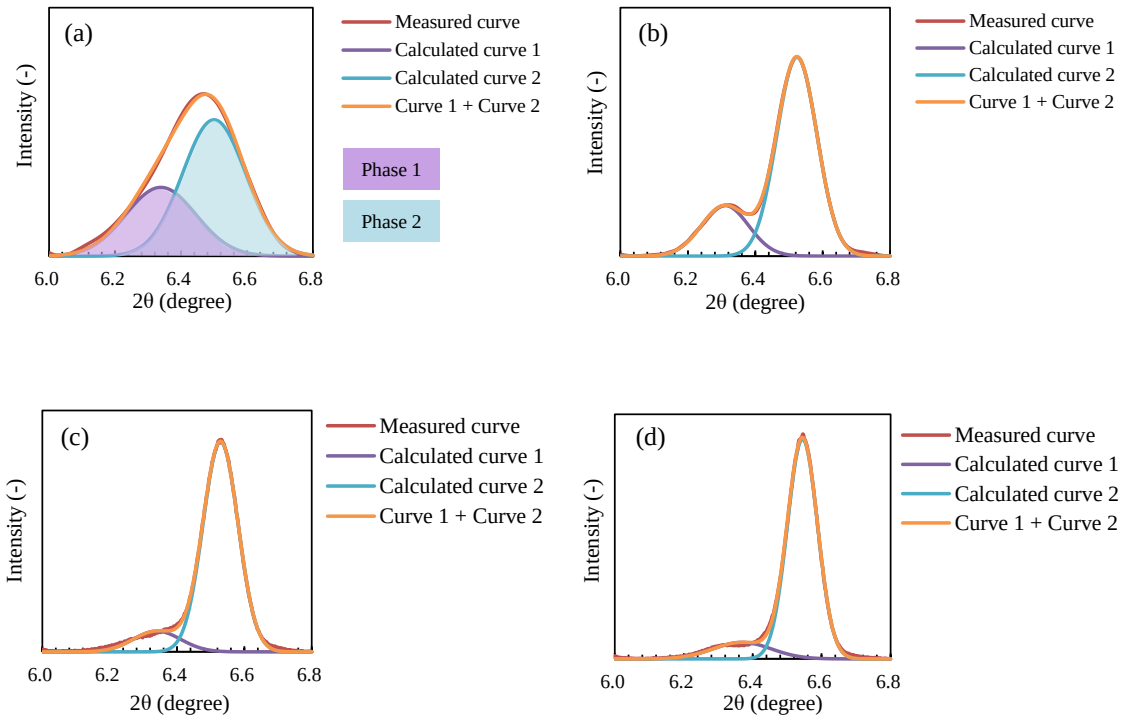

Figure S2 The line profile of XRD patterns of PTF/Q catalysts with film thickness of 50 nm, (a) film thickness: 50 nm; (b) film thickness: 100 nm; (c) film thickness: 150 nm; (d) film thickness: 300 nm. The curve fitting was carried out using the following pseudo Voigt function.

$$V(2\theta) = \eta \cdot L(2\theta) + (1-\eta) \cdot G(2\theta) = \eta \frac{2}{\pi W}\left[1 + \left(\frac{2\theta - 2\theta_i}{W}\right)^2\right]^{-1} + (1-\eta)\ \frac{2\sqrt{\ln 2}}{W\sqrt{\pi}} exp\left[-4\ln 2\left(\frac{2\theta - 2\theta_i}{W}\right)^2\right]$$

V(2θ): pseudo Voigt profile, L(2θ): Lorentzian curve, G(2θ): Gauss curve, 0≤η≤1

$$\textit{Relative peak intensity (-)} = \frac{\textit{Peak intensity of Phase 1}}{\textit{Peak intensity of Phase 2}}$$

4.5.4. Conclusions

It was found that PTF/Q shows photocatalytic activity for the decomposition of water in the presence of several sacrificial agents. PTF/Q containing a thinner film showed the best photocatalytic activity due to the roughness of the catalyst surface, based on the analysis of XRD measurements. Diffraction patterns also revealed that the picene crystals are highly oriented, in a vertical manner, on the surface of the quartz substrate. UV-visible absorption spectra revealed that the optical gap of the catalyst is equivalent to 3.2 eV. The presented work successfully demonstrates the utility of organic semiconductors for the photocatalysis. The results of this study are expected to contribute to the design of efficient and sustainable photocatalytic systems using organic semiconductor catalysts for a wide variety of photocatalytic reactions.

References

1. T. Bak, J. Nowotny, M. Rekas, C.C. Sorrell, *Int. J. Hydro. Energy*, 27 (2002) 991–1022.
2. M. Pumera, *Energy Environ. Sci.*, 4 (2011) 668–674.
3. A. Steinfeld, *Solar Energy*, 78 (2005) 603–615.
4. R. Dholam, N. Patel, M. Adami, A. Miotello, *Int. J. Hydro. Energy*, 34 (2009) 5337–5346.

5. A. Kudo, Y. Misekia, *Chem. Soc. Rev.*, 38 (2009) 253–278.
6. K. Obata, K. Kishishita, A. Okemoto, K. Taniya, Y. Ichihashi, S. Nishiyama, *App. Catal. B: Environ.*, 160–161 (2014) 200–203.
7. R. Abe, *J. Photochem. Photobiol. C Photochem. Rev.* 11 (2010) 179–209.
8. A. Kudo, Y. Misekia, *Chem. Soc. Rev.*, 38 (2009) 253–278.
9. T. Sreethawong, Y. Suzuki, S. Yoshikawa, *Int. J. Hydro. Energy*, 30 (2005) 1053–1062.
10. G. L. Chiarello, M. H. Aguirre, E. Selli, *J. Catal.*, 273 (2010) 182–190.
11. K. Shimura, H. Kawai, T. Yoshida, H. Yoshida, *ACS Catal.*, 2 (2012) 2126–2134.
12. M. Grätzel, *Nature*, 414 (2001) 338–344.
13. A. P. Alivisatos, *J. Phys. Chem.*, 100 (1996) 13226–13239.
14. G. Chen, H. Sasabe, T. Igarashi, Z. Hong, J. Kido, *J. Mater. Chem. A*, 3 (2015) 14517–14534.
15. J. Y. Kim, T. Yasuda, Y. S. Yang, C. Adachi, *Adv. Mater.*, 25 (2013) 2666–2671.
16. Y. Jouane, S. Colis, G. Schmerber, A. Dinia, P. Lévêque, T. Heiser, Y. A. Chapuis, *Org. Electron.*, 14 (2013) 1861–1868.
17. J. A. Merlo, C. R. Newman, C. P. Gerlach, T. W. Kelley, D. V. Muyres, S. E. Fritz, M. F. Toney, C. D. Frisbie, *J. Am. Chem. Soc.*, 127 (2005) 3997–4009.
18. D.L. Talavera, G. Nofuentes, J. Aguilera, M. Fuentes, *Renew. Sust. Energy Rev.*, 11 (2007) 447–466.
19. C. D. Dimitrakopoulos, P. R. L. Malenfant, *Adv. Mater.*, 14 (2002) 99–

117.

20. K. Nagai, T. Abe, Y. Kaneyasu, Y. Yasuda, I. Kimishima, T. Iyoda, H. Imaya, *Chem. Sus. Chem.*, 4 (2011) 727–730.
21. T. Abe, Y. Tanno, N. Taira, K. Nagai, *RSC Adv.*, 5 (2015) 46325–46329.
22. H. Okamoto, N. Kawasaki, Y. Kaji, Y. Kubozono, A. Fujiwara, and M. Yamaji, *J. Am. Chem. Soc.*, 130 (2008) 10470–10471.
23. S. Trasatti, *Pure Appl. Chem.*, 58 (1986) 955–966.
24. S. Gottardi, T. Toccoli, S. Iannotta, P. Bettotti, A. Cassinese, M. Barra, L. Ricciotti, Y. Kubozono, *J. Phys. Chem. C*, 116 (2012) 24503–24511.
25. A. K. Diallo, R. Kurihara, N. Yoshimoto, C. V. Ackermann, *App. Surf. Sci.*, 314 (2014) 704–710.
26. T. Djuric, T. Ules, H. G. Flesch, H. Plank, Q. Shen, C. Teichert, R. Resel, M. G. Ramsey, *Cryst. Growth Des.*, 11 (2011) 1015–1020.
27. Y. Kubozono, H. Goto, T. Jabuchi, T. Yokoya, T. Kambe, Y. Sakai, M. Izumi, L. Zheng, S. Hamao, H. L.T. Nguyen, M. Sakata, T. Kagayama, K. Shimizu, *Physica C*, 514 (2015) 199–205.
28. I. P. M. Bouchoms, W. A. Schoonveld, J. Vrijimoeth, T. M. Klapwiji, *Synth. Met.*, 104 (1999) 175–178.
29. S. Fanetti, M. Citroni, R. Bini, L. Malavasi, G. A. Artioli, P. Postorino, *J. Chem. Phys.*, 137 (2012) 224506-1–224506-7.
30. Q. Xin, S. Duhm, F. Bussolotti, K. Akaike, Y. Kubozono, H. Aoki, T. Kosugi, S. Kera, N. Ueno, *Phys. Rev. Lett.*, 108 (2012) 226401-1–226401-5.

5. General Conclusion

Chapter 5. General Conclusion

This work described the catalyst design and reaction mechanism for the thermal and photo reactions, and clarified the detailed reaction mechanism of benzene oxidation and photocatalytic decomposition of hydrogen carriers. Chapter 2 and 3 covered catalyst design for the heterogeneous metal complex catalyst in the benzene hydroxylation and investigation of the reaction mechanism. Also for the photo reactions, chapter 4 provides the catalyst design of visible-light responsible catalyst and thin-film organic semiconductor, and the reaction mechanism of photo reaction. The obtained result in these chapters are summarised as follows.

In chapter 2.1, for the purpose of catalyst design, the encapsulated vanadium complex catalyst in Y-zeolite was prepared by Ship in a bottle method for the liquid-phase benzene hydroxylation. Encapsulation of the vanadium complex catalyst in the supercage of Y-zeolite allowed us to prevent the catalyst from eluting into the reaction solution. It was found out that the encapsulated catalyst has the catalytic functions for the liquid-phase benzene hydroxylation. And also, effort for catalyst design of binuclear transition metal complex catalysts was performed. Chapter 2.2 revealed binuclear copper complex catalyst has a better catalytic property than mononuclear one. It was found that two copper ions positioned adjacent to each other effectively work for oxidation of benzene with molecular oxygen. Furthermore, in chapter 2.3, the reaction mechanism of benzene hydroxylation in liquid-phase was investigated experimentally and

theoretically. DFT calculations of the oxygen activation process by a vanadium complex revealed the structure of the reaction intermediates and the energy diagram during the process. The results also showed energy gap between V(III)/V(IV) of vanadium complexes is related with the catalytic performance, and it was found out that the reduction process of vanadium complex is the rate determining step in benzene hydroxylation with molecular oxygen in the liquid-phase.

In chapter 3, the gas-phase catalytic oxidation of benzene was performed over Cu/HZSM-5 catalysts with added Ti using molecular oxygen. The decrease of O_2 partial pressure prevented formation of the by-products, and thus improved the phenol selectivity considerably. Addition of Ti to Cu/HZSM-5 also improved the phenol yield, and led to the increase of Cu^+ sites, which was closely related to the phenol formation activity of Cu/Ti/HZSM-5. The copper and titania supported HZSM-5 catalyst (Ti/Cu atomic ratio = 0.7) exhibited the extremely good catalytic performance of phenol yield (4.3%) and phenol selectivity (88.0%) for the direct oxidation of benzene to phenol under lower O_2 partial pressure. From the result of O_2 uptake measurement, it was found out that titania provided highly dispersion of copper, and improvement of the catalytic performance.

Chapter 4 described catalyst design for visible-light responsible catalyst and investigation of the reaction mechanism. In chapter 4.1, photo-oxidation of cyclohexane by tungsten oxide was studied. Cyclohexanone and cyclohexanol were obtained with high selectivity in the reaction under visible light irradiation. On the basis of isotope labeled experiments and

ESR measurement, it was found out that cyclohexyl radical is formed as a reaction intermediate during light irradiation. And also, the lattice oxygen of WO_3 was inserted into the products, thus it was suggested that the products are produced by the reaction of cyclohexyl radical with the lattice oxygen of WO_3. Furthermore, the physical mixing of TiO_2 with Pt/WO_3 led to higher photocatalytic activity than that of Pt/WO_3. The photocatalytic activity increased with increasing BET surface area of TiO_2 mixed to Pt/WO_3. The physical mixing of TiO_2 was found to accelerate the formation of cyclohexyl radical. It was therefore speculated that the surface of TiO_2 contributes to the formation of cyclohexyl radical or stabilization of cyclohexyl radical. Chapter 4.2 and 4.3 described catalyst design of visible-light responsible titanium oxide and investigation of the reaction mechanism for the photodecomposition of ammonia. TiO_2 photocatalyst doped with iron ($Pt/Fe–TiO_2$) led to a higher activity than undoped TiO_2 photocatalysts (Pt/TiO_2). It was found from UV–vis, ESR, and XRD measurements that by substituting Fe^{3+} for Ti^{4+}, the resulting $Fe–TiO_2$ catalyst material might allow for the effective utilization of irradiation light owing to the presence of a Fe impurity band, thereby leading to its higher activity. From ESR measurements for reaction mechanism investigation, it was indicated that a NH_2 radical formed as an intermediate. To further investigate the mechanism of the NH_3 decomposition, the two reaction pathways in which N_2 and H_2 formed through a NH_2 radical were considered, that is the formation of the NH radicals through extraction of each hydrogen atom from the two NH_2 radicals (route 1) or the formation of NH_2-NH_2 by the coupling

of adjacent NH_2 radical (route 2). DFT calculations indicated route 2 was more favorable pathway than route 1. Chapter 4.4., based on knowledge acquired from chapter 4.1, deals with preparation of visible-light responsible titania oxide catalyst by co-doping with two different transition metal ions. Ta and Cr co-doped titanium oxide was successfully prepared, and exhibited extremely good catalytic property for the photodecomposition of water with urea. Furthermore, the decomposition mechanism of urea in water decomposition was investigated. Urea was found to be converted into N_2 and CO_2 by titanium oxide photocatalysts. In chapter 4.5, catalyst design for organic semiconductors was described. It was found out that picene, which is a representative low-weight organic semiconductors, effectively worked for photocatalytic decomposition of water with sacrificial agents. Thin-film structure of picene crystal on a quartz sheet had influence on the catalytic performance. The catalyst on which the picene crystal is roughly dispersed had excellent photocatalytic activity for hydrogen formation. The result indicates that the control of the surface morphology is very important to further improve the performance of PTF/Q in the photocatalytic process.

This work clarified detailed reaction mechanisms of benzene oxidation and several photocatalytic reactions, and summarised most important literature to catalyst design, its development and the main ways it is done. Throughout this whole thesis, there are a lot of studies and commentaries on a better understanding of their reaction mechanisms. The need for more thorough knowledge about the mechanisms and optimal

conditions for new and existing reactions is still large. In conjunction with computational efforts, which has seen great progress the last decades, a versatile tool to uncover mechanistic details is available. Since a computational study already has been performed, a combination of calculations and experimental work in this thesis is probably the best way to advance catalytic reactions.

List of Achievements

List of publications

Chapter 2

1. Liquid-phase Oxidation of Benzene with Molecular Oxygen over Vanadium Complex Catalysts Encapsulated in Y-Zeolite,
   Atsushi Okemoto, Yoshiki Inoue, Koichi Ikeda, Chiaki Tanaka, Keita Taniya, Yuichi Ichihashi, Satoru Nishiyama,
   Chemistry Letters, Vol.43 No.11 (2014), pp 1734–1736.

2. Study of Benzene Hydroxylation in Liquid Phase Using Mono- and Binuclear Copper Complex Catalysts,
   Atsushi Okemoto, Kurumi Kato, Keita Taniya, Yuichi Ichihashi, Satoru Nishiyama,
   Chemistry Letters, Vol.44 No.3 (2015) pp.384–386.

3. Theoretical study of reaction mechanism for selective oxidation of benzene by vanadium complex catalysts encapsulated in Y-zeolite,
   Atsushi Okemoto, Arisa Utsunomiya, Yoshiki Inoue, Hisayoshi Kobayashi, Takafumi Horie, Keita Taniya, Yuichi Ichihashi, Satoru Nishiyama,
   Under preparation

4. Direct Oxidation of Benzene with Molecular Oxygen in Liquid Phase Catalysed by Heterogeneous Copper Complexes Encapsulated in Y-type Zeolite,
   Atsushi Okemoto, Yusuke Ozawa, Ryousuke Nakahata, Keita Taniya, Yuichi Ichihashi, Satoru Nishiyama,
   Submitted to Catalysts.

Chapter 3

5. Selective catalytic oxidation of benzene over Cu/Ti/HZSM-5 under low oxygen pressure for one step synthesis of phenol,
   Atsushi Okemoto, Yo-hei Tsukano, Arisa Utsunomiya, Keita Taniya, Yuichi Ichihashi, Satoru Nishiyama,
   Journal of Molecular Catalysis A: Chemical, 411 (2016) pp.372–376.

Chapter 4

6. Photocatalytic decomposition of NH_3 over TiO_2 catalysts doped with Fe,
   Kazutaka Obata, Kensuke Kishishita, Atsushi Okemoto, Keita Taniya, Yuichi Ichihashi, Satoru Nishiyama,
   Applied Catalysis B: Environmental, 160-161 (2014) pp.200–203.

7. Application of picene thin-film semiconductor as a photocatalyst for photocatalytic hydrogen formation from water,
   Atsushi Okemoto, Kensuke Kishishita, Sho Maeda, Shin Gohda, Masahiro Misaki, Yasuko Koshiba, Kenji Ishida, Takafumi Horie, Keita Taniya, Yuichi Ichihashi, Satoru Nishiyama,
   Applied Catalysis B: Environmental, 192 (2016) pp.88–92.

8. Hydrogen Production for Photocatalytic Decomposition of Water with Urea as a Reducing Agent,
   Atsushi Okemoto, Kazuhito Tanaka, Yumika Kudo, Shin Gohda, Yasuko Koshiba, Kenji Ishida, Takafumi Horie, Keita Taniya, Yuichi Ichihashi, Satoru Nishiyama,
   Catalysis Today, in press.

9. Reaction mechanism of ammonia photodecomposition over Ni/TiO_2 photocatalysts,
   Arisa Utsunomiya, Atsushi Okemoto, Yuki Nishino, Kensuke Kitagawa, Keita Taniya, Yuichi Ichihashi, Satoru Nishiyama,
   Applied Catalysis B: Environmental, 206 (2017) pp.378-383.

10. The Study of WO_3-TiO_2 Physical Mixed Catalysts for Cyclohexane Photooxidation under Visible Light Irradiation,
    Kohei Ueyama, Atsushi Okemoto, Takuya Hatta, Shingo Saijo, Keita Taniya, Yuichi Ichihashi, Satoru Nishiyama,
    Under preparation

Other publications

1. メタンと水から水素を作る光触媒の開発,

   市橋祐一、牧野伸彦、桶本篤史、谷屋啓太、西山覚,

   スマートプロセス学会誌, Vol.2, No.6 (2013) pp.282‐286.

2. Role of Al^{3+} species in beta zeolites for Baeyer-Villiger oxidation of cyclic ketones by using H_2O_2 as an environmentally friendly oxidant,
   Keita Taniya, Ryota Mori, Atsushi Okemoto, Takafumi Horie, Yuichi Ichihashi, Satoru Nishiyama,
   Submitted to Catalysis Today.

3. Mechanistic Study of Water Gas Shift Reaction over Cu-ZnO-Al_2O_3 Catalysts in a Reformed Gas Atmosphere - Influence of hydrogen in reaction atmosphere on the rate for WGRS -,
   Keita Taniya, Yasuhiro Horie, Ryo Fujita, Atsushi Okemoto, Yuichi Ichihashi, Satoru Nishiyama,
   Submitted to Journal of Catalysis.

4. Preparation of a Photoresponsive Tracer to Evaluate the Performance of Dry-Type Powder Photoreactors,
   Junichi Hirota, Taro Inoue, Toru Watanabe, Atsushi Okemoto, Takafumi Horie, Naoto Ohmura, Keita Taniya, Yuichi Ichihashi, Satoru Nishiyama,
   Submitted to Journal of Chemical Engineering of Japan.

5. Hydrogen Formation from Water with Methane in the Gas Phase over Ni-Cr/TiO_2 Photocatalyst Prepared by Electroless Plating Method,
   Sho Maeda, Atsushi Okemoto, Nobuhiko Makino, Takafumi Horie, Keita Taniya, Yuichi Ichihashi, Satoru Nishiyama,
   Under preparation.

Awards

1. 優秀ポスター賞, 日本エネルギー学会完成支部第 58 回研究発表会/石油学会関西支部第 22 回研究発表会, 2013.12

2. 優秀研究賞, 近畿化学協会平成 26 年度第 2 回キャタリストクラブ例会第 7 回触媒表面化学研究発表会, 2014.10

3. Outstanding Student Award, Premium Program of Kobe University, 2016.1

4. Excellent Poster Presentation Award, International Symposium on Nanostructured Photocatalysts and Catalysts, 2016.4

Acknowledgements

The studies presented in this thesis are the summaries of the author's works carried out during 2011–2016 at the Department of Chemical Engineering, Faculty of Chemical Engineering, Kobe University.

The author takes opportunity to express his sincere gratitude to Professor Yuichi Ichihashi, Professor Satoru Nishiyama, Professor Kenji Ishida, and Professor Naoto Ohmura for their continuing guidance, valuable discussion, and encourage during this work.

Special thanks are given to Professor Hisayoshi Kobayashi of Kyoto Institute of Technology for his effectual suggestion and kind discussion on DFT calculations. The author also sincerely thanks to Professor Sophie Hermans and Professor Michel Devillers of University of Catholic Louvain for their kind support in the preparation of copper complex supported carbon nanotubes and useful suggestions.

He would like to express heartfelt thanks to Professor Keita Taniya, Dr. Yasuko Koshiba, Mr. Norihisa Kumagai of Kobe University, and Dr. Masahiro Misaki of Kindai Univeristy Technical College, for their helpful suggestions and supports. I would also like to take this opportunity to thanks Mr. Shin Gohda of Nard Institute, LTD. for years of his tremendous support and helpful advice.

It is also his great pleasure to thank Mr. Norihisa Kumagai, Mr. Yoshiki Inoue, Mr. Ko-hei Tsukano, Mr. Kazuhito Tanaka, Mr. Shun

Watanabe, Mr. Hisato Fujiwara, Ms. Kurumi Kato, Mr. Kensuke Kishishita, Ms. Arisa Utsunomiya, with whom the author has collaborate and had many instructive discussions during course of this study.

Atsushi Okemoto

Kobe University

2017

Publication data

神戸大学博士論文「Mechanistic study on redox reactions over heterogeneous catalysts and design of local structure of active sites」全 240 頁

提 出 日 2019 年 1 月 19 日

Doctor Thesis, Kobe University

“Mechanistic study on redox reactions over heterogeneous catalysts and design of local structure of active sites”, 240 pages

Submitted on January, 19th, 2019

The date of publication is printed in cover of repository version published in Kobe University Repository Kernel.